Title
Atomically Thin Processing of High Surface Area Nanomaterials for Electrochemical Energy Devices

Author
Kao, Emmeline

Publication Date
2018

Peer reviewed|Thesis/dissertation

Atomically Thin Processing of High Surface Area Nanomaterials for Electrochemical Energy Devices

by

Emmeline Y. Kao

A dissertation submitted in partial satisfaction of the

requirements for the degree of

Doctor of Philosophy

in

Engineering – Mechanical Engineering

in the

Graduate Division

of the

University of California, Berkeley

Committee in charge:

Professor Liwei Lin, Chair
Professor Hayden Taylor
Professor Dorian Liepmann

Spring 2018

Atomically Thin Processing of High Surface Area Nanomaterials for Electrochemical Energy Devices

Emmeline Y. Kao

Abstract

Atomically Thin Processing of High Surface Area Nanomaterials for Electrochemical Energy Devices

by

Emmeline Y. Kao

Doctor of Philosophy in Engineering – Mechanical Engineering

University of California, Berkeley

Professor Liwei Lin, Chair

As interest in renewable energy grows on both research and policy fronts, energy storage likely represents one of the most viable solutions to the problems posed by the intermittency and irregularity of renewable resources. While new classes of materials promise improved performance of energy storage systems, understanding energy storage electrode architecture and fabrication at the micro-scale allows us to fully leverage performance along different dimensions.

This dissertation aims to explore the use of device architecture manipulation to improve energy storage and conversion electrodes, focusing on addressing challenges around manufacturing high-surface area electrodes. Phsyically, our approach to texturizing electrodes consists of synthesizing materials as to create high-surface area templates while physically manipulating the electrode to maximize performance. Chemically, we manipulate performance with Ångström-level precision, utilizing atomically thin layers to induce chemical enhancement of our devices at the electrode interface.

The principles of leveraging physical and chemical manipulation of electrodes is demonstrated in five unique works: (1) atomic layer deposition of titanium-nitride on carbon nanotubes for supercapacitor applications, (2) two-dimensional iron-phosphate for supercapacitor applications, (3) thiophene-based electrodeposition for photoelectrochemical water splitting, (4) titanium dioxide-coated zinc oxide nanowire arrays for photoelectrochemical water splitting, and (5) development of atomic layer deposited black titania for photoelectrochemical water splitting.

To Him who is able to do immeasurably more than all we ask or imagine...

Contents

List of Figures

Nomenclature

Abbreviations

2D Two-Dimensional

ACR Assigned Commissioners Ruling

Ag/Ag+ Silver/Silver+ reference electrode

Ag/AgCl Silver/Silver Chloride Reference Electrode

ALD Atomic Layer Deposition

AR4 Fourth Assessment Report

AR5 Fifth Assessment Report

b-TiOx Black Titania

CNT Carbon Nanotubes

CV Cyclic Voltammogram

CVD Chemical Vapor Deposition

EDLC Electric Double Layer Capacitance

EIS Electrochemical Impedance Spectroscopy

$FePO_4$ Iron Phosphate

FESEM Field Emission Scanning Electron Microscopy

GWP Global Warming Potential

H_2 Hydrogen Gas

H_2SO_4 Sulfuric Acid

IOU Independently Owned Utilities

IPCC International Panel on Climate Change

$LiFePO_4$ Lithium Iron Phosphate

MEMS MicroElectroMechanical Systems

N_2 Nitrogen

O_2 Oxygen Gas

PDMS Polydimethylsiloxane

PEC Photoelectrochemical

PPY Polypyrrole

Pt Platinum

PV Photovoltaic

RCP Representative Concentration Pathways

RF Radiative Forcing

RPS Renewable Portfolio Standard

SAIDI System Average Interruption Duration Index

SDBS Sodium Dodecylbenzene Sulfonate

SEM Scanning Electron Microscopy

TDMAT Tetrakis (dimethylamido) titanium

TEM Transmission Electron Microscopy

TiN Titanium Nitride

TiO_2 Titanium Dioxide

$TiO_{2-x}N_x$ Titanium Oxynitride

TMDC Transition Metal Dichalcogenide

UV Ultraviolet

VACNT Vertically Aligned Carbon Nanotubes

XPS X-ray photoelectron spectroscopy

XRD X-ray Diffraction

ZnO Zinc Oxide

Acknowledgments

The work presented in this dissertation would not have reached this stage were it not for my scientific friends, colleagues, and mentors:

To Professor Liwei Lin, thank you for your years of support in my career. From the first email sent to preparing me for the notorious world of academia, thank you. To my thesis committee, Professor Hayden Taylor and Professor Dorian Liepmann, thank you for teaching me in your classes, supporting me in quals, on the job market, and at this final chapter of my PhD.

The Linlab has been my daily habitat, but it was its members that brought joy to my work. Thank you to Hyun Sung Park and Simon Liu for endless discussions of Korean food, theology, American culture, and everything in between. Thank you to my office mates in 668 SDH—Eric Sweet, Ilbey Karakurt, Jacqueline Elwood, Junwen Zhong, Sedat Pala, and Xining Zang–who convinced me to move out of the basement and (literally) into the sunlight and have filled our office with laughter. Thank you especially to Roseanne Warren, Casey Glick, Chen Yang, Levent Beker, Ben Eovino, Caiwei Shen, Hyung-seok Jang, Jinwoo Bae, and Neil Ramirez.

To my undergraduates and highschoolers, whom I've had the privilege to mentor–Goran Rez-Kallah Bertholet, Jianan Lu, Winston Ou, Albert Li, Qiaohao Liang, Lujie Yang, Eh-Hsa Say, Sairy Roman Perez–thank you for your diligence and openess to growing with me.

Lastly, I want to thank those who have come before me, who have dedicated their work to solving our world's great problems through science. It has been an honor to add to this body of work.

A PhD can make you feel that living a full and rich life comes secondary to your work. I want to acknowledge all those who instead reminded me of the truth:

When I was 10, my father told me he wakes up every day ready to go to work in academia—because he loved what he did. My family has inspired, challenged, supported, and guided me more than anyone else in my life. It's impossible to write in this space of the influence my family, so I will say only these few things: To my parents, at this point, you've raised 3 doctors and remain humble about your role in our accomplishments. But you've always taught us to put God and people first, live life beyond our work, and to rest in prayer. To my two rock-star siblings, Katherine and Jonny, it's been a blessing to grow up in your shadow, be inspired by your love and work, and be the coddled youngest child. You have been salt and light for me. Matthew 5:13–16

Thank you to my Berkeley community: Veritas Graduate Christian Fellowship, Monday small group, and Megan Wong. You reminded me every day that I'm not alone and was never meant to be alone in our journey. We've shared meals, pontificated about superheroes, and waded through theology together. Thank you for indulging my love

for boba, going to Purple Kow, ShareTea, Tea1, I-Tea, Happy Lemon, and 85C with me. Psalm 34:8

Thank you especially to Becky Portnoff, Jeff Kang, Joy Wan, and Marquita Ellis: you've delighted me with intricate conversations of our PhD work in God's kingdom, commiserated over trials and tribulations, supported me with boba, cookies, brownies, places to nap, endless phone calls, and unlimited hugs, challenged me in almost every way possible, and encouraged me more than I deserve. Living life with you these past 5 years has been one of my greatest joys. Acts 2:42

Lastly, my Creator, Father, Redeemer, and Friend. You never leave me. Phillippians 3:7–8

Chapter 1

Introduction

1.1 Motivation

Harnessing, utilizing, and storing energy is a bedrock upon which our society grows, thrives, and carries out its most basic functions. In its most broad definition, energy is the ability to do work. However, energy systems are varied and vast. This dissertation focuses on innovations in electrochemical energy storage and conversion. In everyday life, we find ourselves thoroughly surrounded by energy storage and conversion. Energy stored in foods powers our ability to live, work, and grow. Our societies employ stored energy in the form of fossil fuels, nuclear fuels, or available energy sources such as wind and solar to power heating, electricity, and other basic functions. Even our earth relies on the storage and conversion of energy: our climate and ecosystem use and store energy from a fusion hydrogen star millions of miles away.

Inspired by the role of energy in our societies, the scope of this dissertation is to consider the role of nanoscale device architecture in improving energy devices. In doing so, this work aims to present solutions that reduce dependency on fossil fuels, instead presenting a pathway toward alternative storage and conversion mechanisms.

The Intergovernmental Panel on Climate Change (IPCC), whose objective is the "stabilization of greenhouse gas concentrations in the atmosphere at a level that would prevent dangerous anthropogenic interference with the climate system," (Pachauri et al., 2014) has declared a human link to climate change. In their latest report, the fifth assessment report (AR5), they write "[h]uman influence on the climate system is clear, and recent anthropogenic emissions of greenhouse gases are the highest in history. Recent climate changes have had widespread impacts on human and natural systems." (Pachauri et al., 2014)

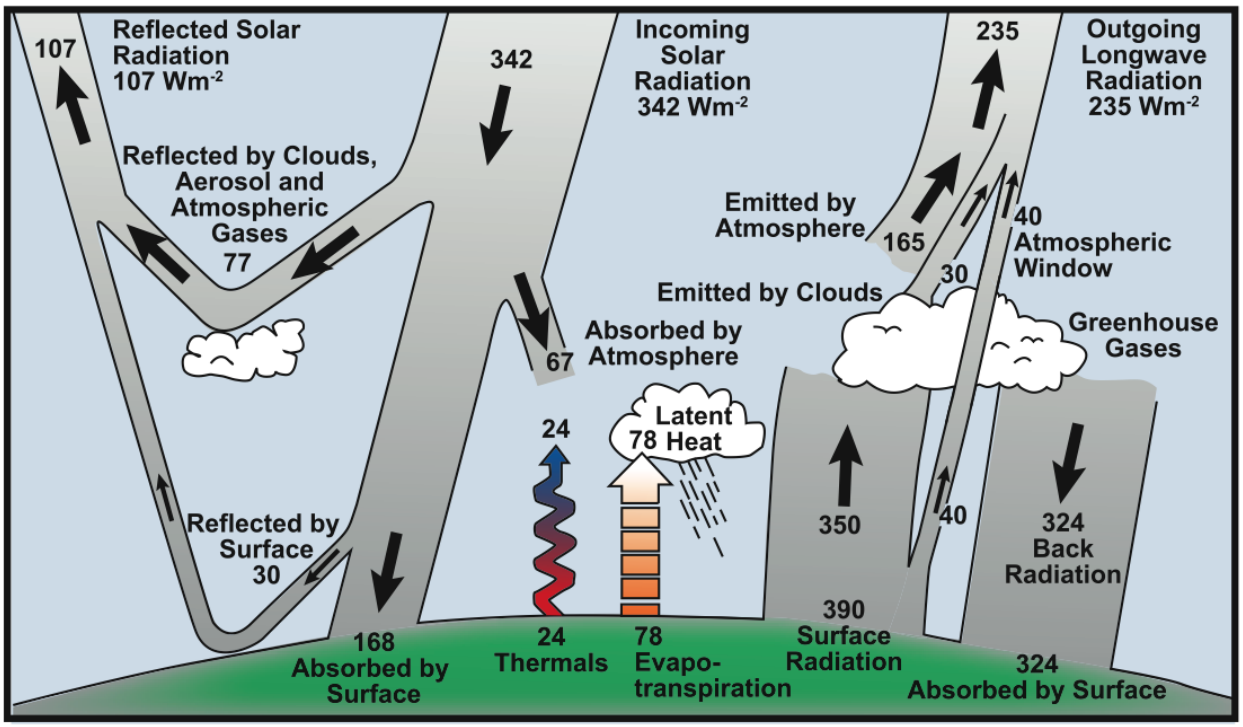

Figure 1.1: Energy Flows in our climate, estimated in $\frac{W}{m^2}$(Kiehl and Trenberth, 1997)

1.2 Climate Change Metrics

In understanding climate change, a working understanding of energy metrics used by climate scientists and policy makers is essential to building tools to mitigate climate change. This section is a brief primer on climate change metrics.

1.2.1 Radiative Forcing

Earth's global mean energy balance is estimated as shown in Figure 1.1, corresponding to average total energy flows on the order of hundreds of $\frac{W}{m^2}$.(Kiehl and Trenberth, 1997) Radiative forcing, described as RF, is a metric by which the change in climate conditions due to a specific factor can be quantified in $\frac{W}{m^2}$. IPCCs fourth assessment report (AR4) describes radative forcing as

"Radiative forcing is a measure of the influence a factor has in altering the balance of incoming and outgoing energy in the Earth-atmosphere system and is an index of the importance of the factor as a potential climate change mechanism. In this report radiative forcing values are for changes relative to preindustrial conditions defined at 1750 and are expressed in watts per square meter (W/m^2)" (IPC and Change, 2007)

This factor describes the rate of energy change, normalized by area, for a given factor.

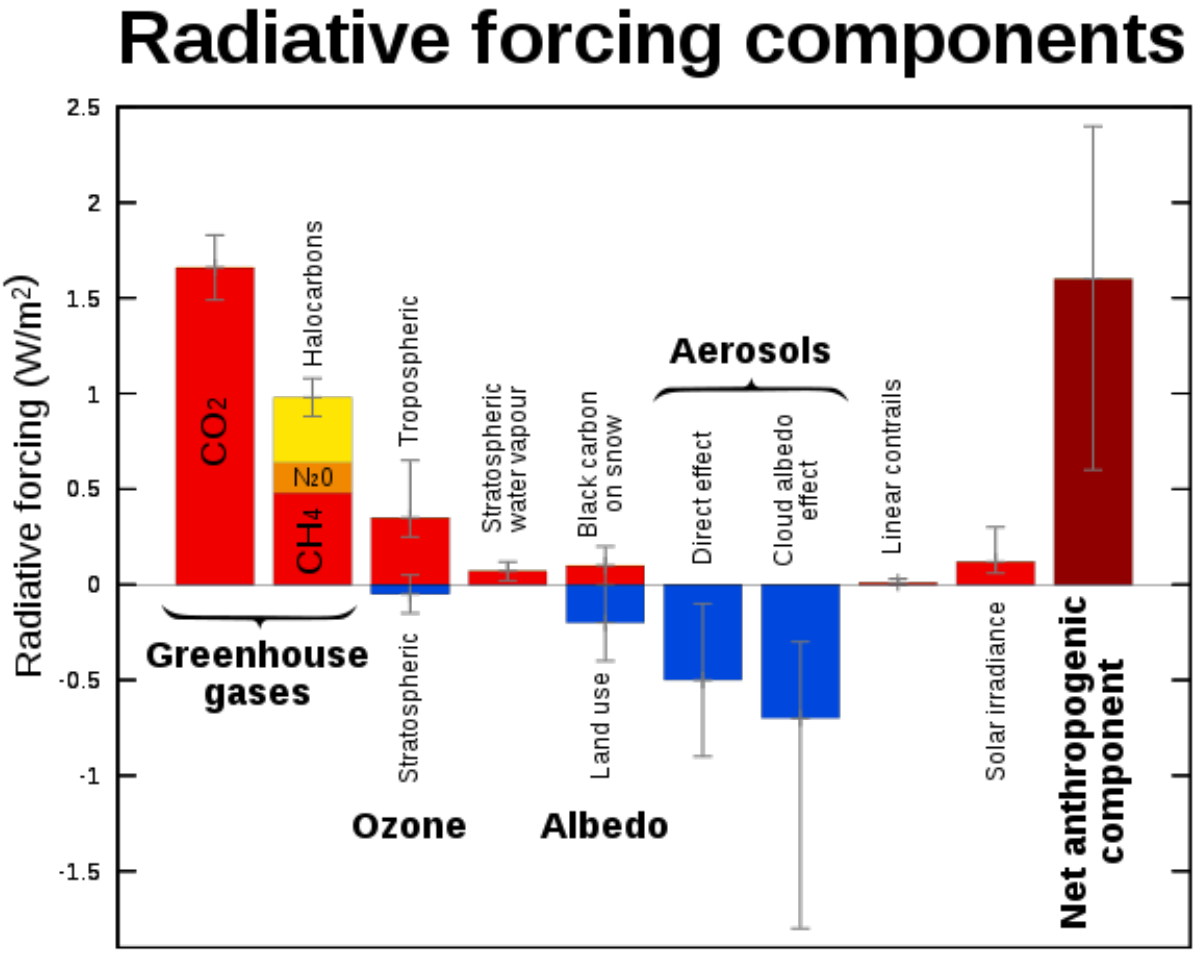

Figure 1.2: Estimated radiative forcings for common anthropogenic factors (IPC and Change, 2007)

For the usage which IPCC employs, the energy change is measured relative to pre-industrial conditions, ca. 1850. For example, commonly cited anthropogenic factors and their corresponding radiative forcings are shown in Figure 1.2, as shown in the IPCC AR4.(IPC and Change, 2007) As shown in Figure 1.2, anthropogenic radiative forcing is estimated to be orders of magnitude lower than that of the energy flows throughout our earth, as shown in Figure 1.1. However, the sensitivity of our climate to those forcings can be described by the Climate Sensitivity Parameter.

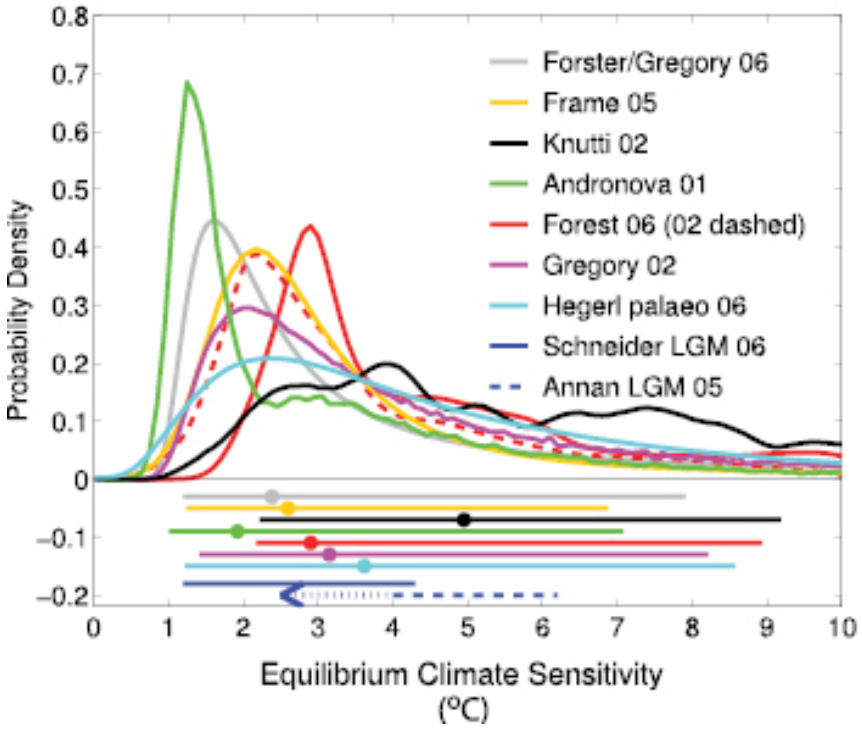

Figure 1.3: Modeled climate sensitivity parameters (IPC and Change, 2007)

1.2.2 Climate Sensitivity Parameter

The Climate Sensitivity Factor describes the mean temperature change due to radiative forcing,

$$\lambda = \frac{\Delta T}{RF} \tag{1.1}$$

Consequently, the Climate Sensitivity Parameter can also be used to estimate the temperature change given a specific radiative forcing. The parameter is found by modeling global-average surface temperature; a number of estimated parameters, as collected by IPCC, are shown in Figure 1.3.

1.2.3 Global Warming Potential

Global Warming Potential (GWP) is a dimensionless metric by which the mass of a greenhouse gas is directly related to climate change. It is defined as

$$GWP = \frac{\int_0^T RF_{gas} R_{gas}(t)dt}{\int_0^T RF_{CO_2} R_{CO_2}(t)dt} \tag{1.2}$$

where RF is the radiative forcing per kg, R is the mass of the gasses in kg, and T is the time over which the impact is evaluated for both gases. The time is critical, given that different greenhouse gases experience different atmospheric persistence. For example, methane, as estimated in AR5, has an estimated GWP of 86 over 20 years, but a GWP 34 over 100 years. Thus, in the next 20 years, the effect of methane on temperature is expected to be 86 times that of CO_2 for the same mass of gas released. Similarly, over the next 100 years, methane rates as 34 times more potent as the same mass of CO_2.

In the GWP equation, this is captured in the mass, as a function of time.

1.3 Modeling of Climate Change and Mitigation Strategies

IPCC has shown that increases in CO_2 is correlated with temperature increases relative to pre-industrial times. Figure 1.4 shows the increase in temperature from 1890–2010, projecting into the future under different scenarios, known as representative concentration pathways (RCP). Each RCP is described by the radiative forcing in the year 2100 relative to pre-industrial times. For example, RCP 8.5 is the projected CO_2 emissions and corresponding temperature increase if the cumulative radiative forcing in 2100 is $8.5\frac{W}{m^2}$.

The relation between radiative forcing and increased greenhouse gases is shown in Figure 1.5. To achieve a lower temperature anomaly relative to pre-industrial times, mitigation strategies for reducing greenhouse gasses are critical. There are a number of strategies to doing so; this dissertation will focus on energy production and storage.

The carbon emissions associated with fossil fuel usage globally, shown in Figure 1.6, total around 10 billion metric tons of carbon/year. In the U.S., fossil fuels comprise the majority of electricity generation, with natural gas accounting for 33% of the emissions in 2016 (recall that on a 20 year horizon, CH_4, a main component of natural gas, has a GWP of 86) and coal accounting for 32% (Figure 1.7). Decreasing reliance on low-carbon emission fuels is therefore a compelling strategy for climate change mitigation: fewer carbon emissions are expected to result in decreased radiative forcing, thus allowing for a pathway corresponding to lower global temperature increases.

1.4 Role of Energy Conversion in Mitigation Strategies

The role of energy conversion in decreasing reliance on fossil fuels is clear: all forms of electricity generation take place due to some kind of energy conversion process, also known as a transducing process. For renewable energies, the starting energy form is considered to

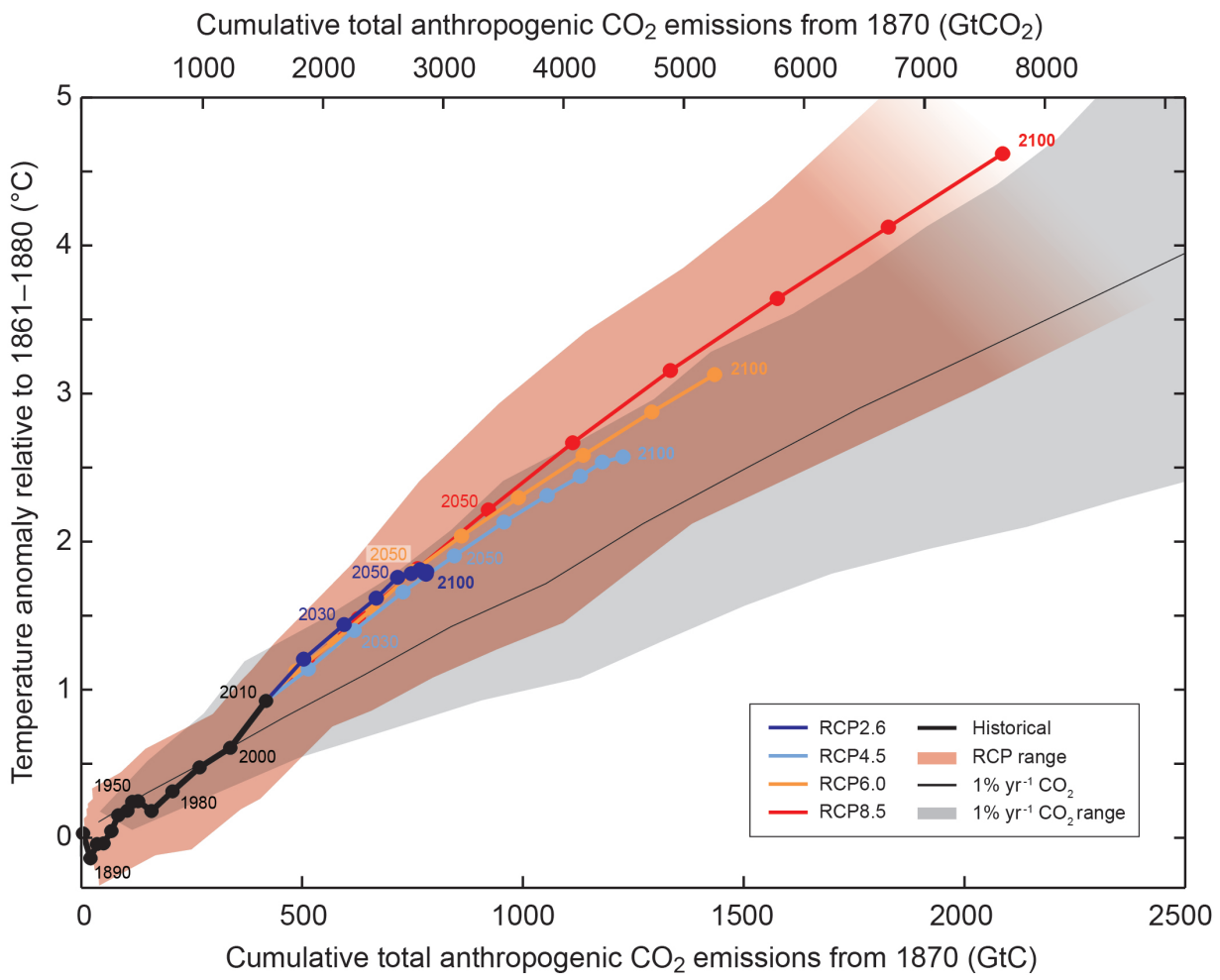

Figure 1.4: Representative Concentration Pathways projection, as modeled in IPCC AR5 (Pachauri et al., 2014)

be a quasi-unlimited or renewable resource, such as wind (wind → mechanical energy → electricity), solar (solar photons → electricity), or hydro (potential energy → electricity).

A well-known method to conceptualize mitigation is using the stabilization triangle. Developed by Professors Robert Socolow and Stephen Pacala,(Pacala and Socolow, 2004) it presents a pathway toward stabilizing emissions at their current level, where the difference between the business-as-usual ramp and stabilization is represented by the "stabilization triangle." (see Figure 1.8) This triangle is further subdivided into 8 wedges, where each wedge represents a carbon-cutting strategy that would cut 1 billion tons of carbon per year.

Furthermore, Socolow and Pacala posit that multiple wedges are already available. They outline 15 possible strategies, 6 of which are in the realm of renewable energy (see Figure 1.9)—further cementing the role of energy conversion in the form of renewables to achieving

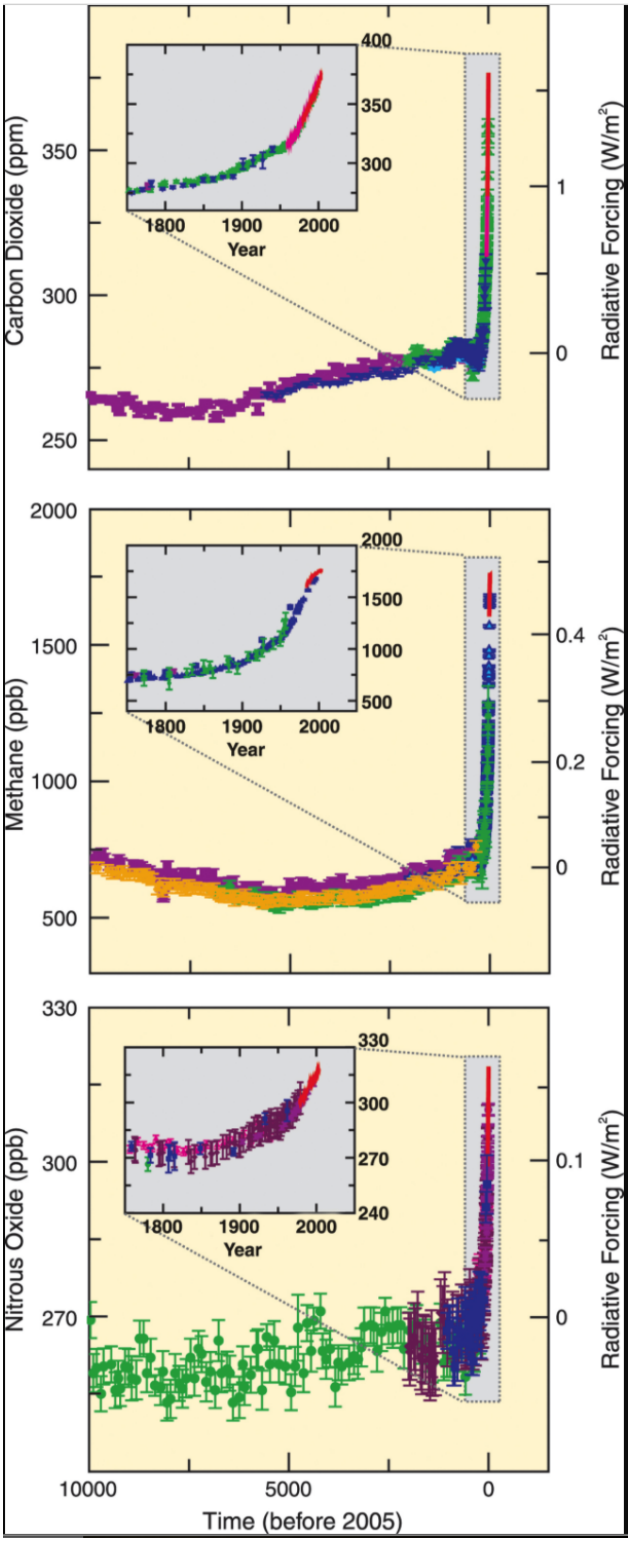

Figure 1.5: Common greenhouse gasses and associated radiative forcing, as a function of time since the pre-industrial period. (Pachauri et al., 2014)

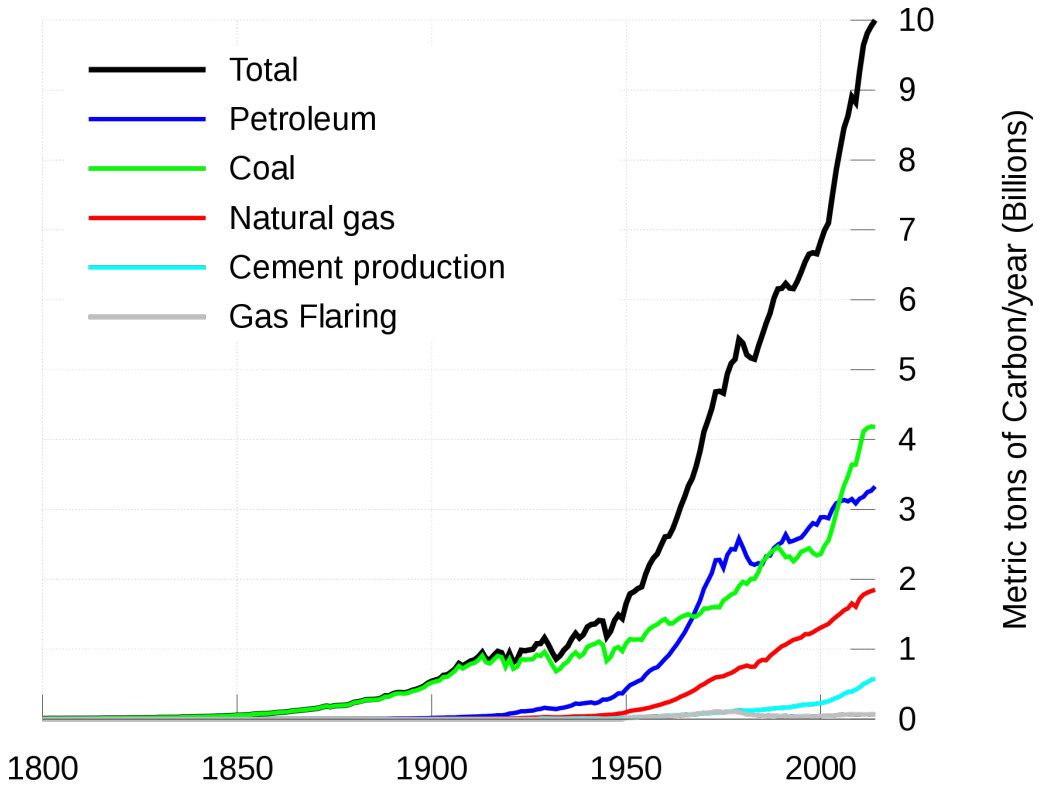

Figure 1.6: Estimated global carbon emissions for fossil fuels (Marland et al., 1994)

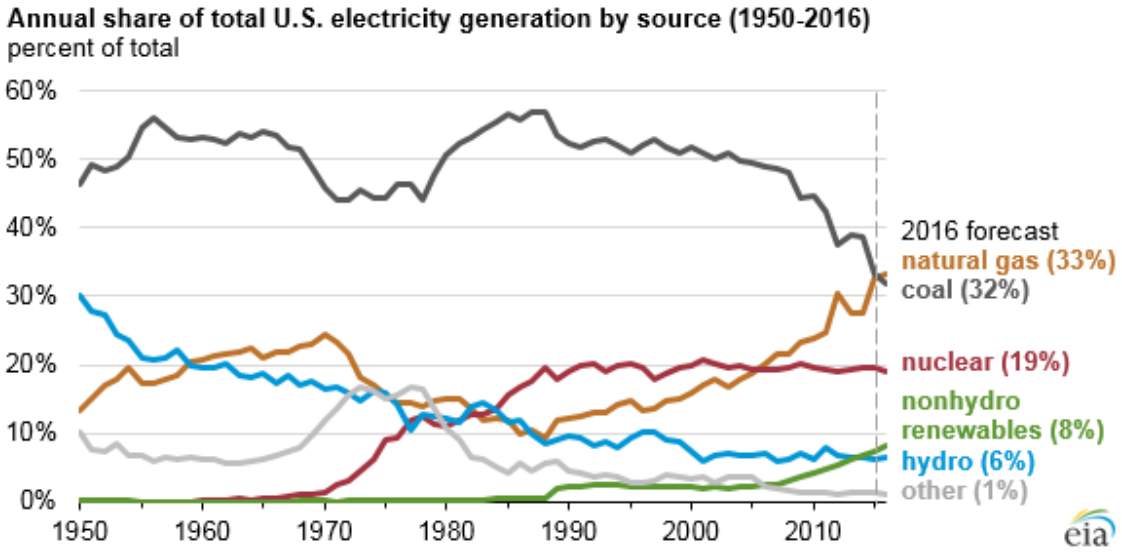

Figure 1.7: A map of U.S. electricity production (EIA, 2016)

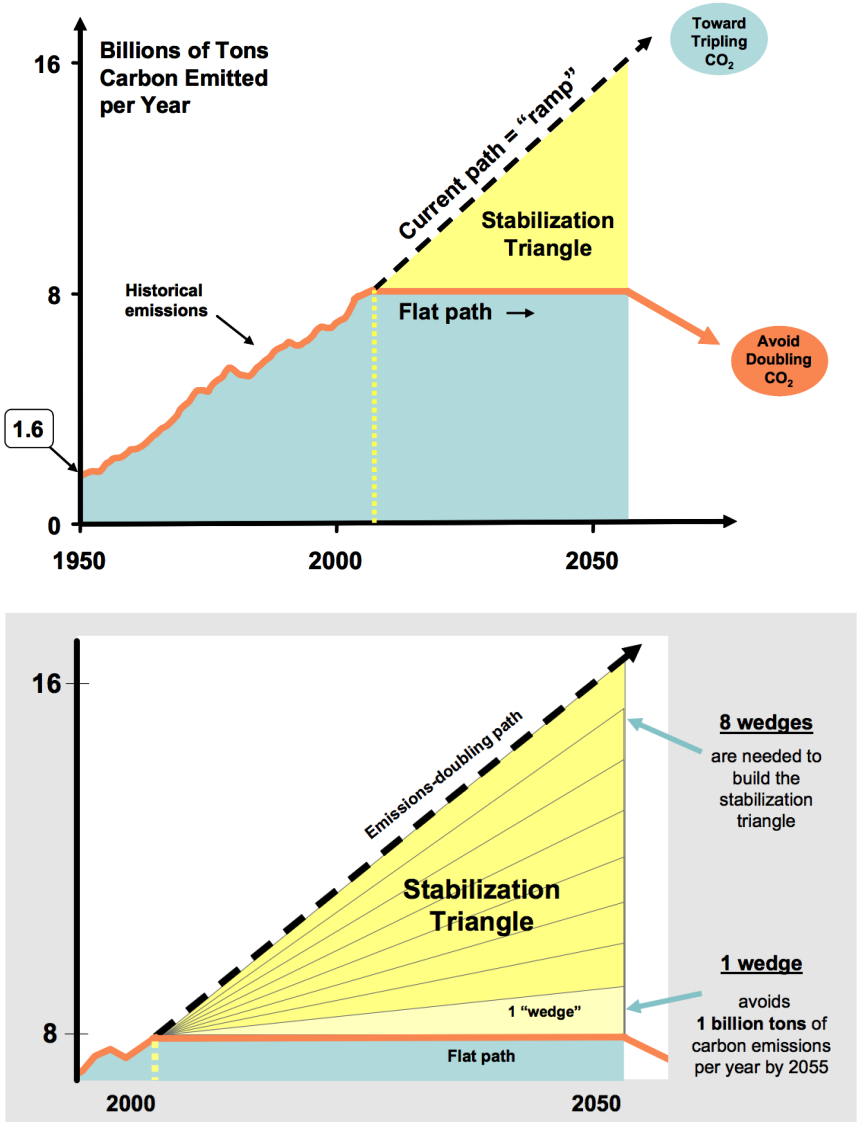

Figure 1.8: Conceptual illustration of the stabilization triangle, as presented by Professors Robert Socolow and Stephen Pacala (Pacala and Socolow, 2004)

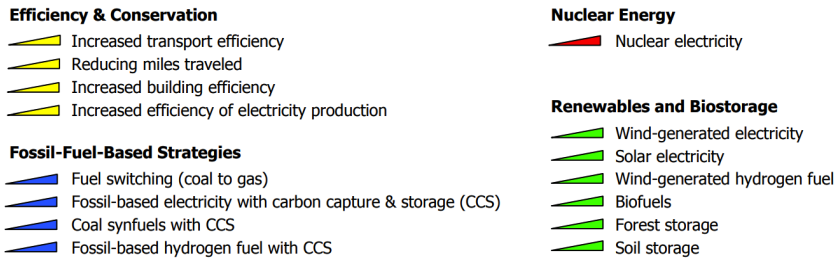

Figure 1.9: Options for wedges, representing a pathway toward reducing 1 billion tons of carbon per year (Pacala and Socolow, 2004)

reduction in radiative forcing.

1.5 Role of Energy Storage in Mitigation Strategies

On midday, May 11, 2014, Germany's electricity sector reached a record high 75% of renewable energy in their overall electricity demand. The portion of electricity coming from wind and solar throughout the country was so great that electricity prices even dipped into the negative for much of the afternoon, (Kroh, 2014) just one of the effects of Germany's radical Energiewende (Energy transition). However, measured across the entirety of the first half of 2014, renewables made up just 31% of all electricity demand in Germany. These two data points, when taken in context, underscore the potency and potential in renewables, yet also highlight a critical flaw–these resources are not consistent.

In comparison to Germany, the United States boasts significantly fewer renewable resources as a percentage of their energy portfolio. In 2014, renewable sources accounted for about 10% of electricity consumption and 13% of electricity generation, less than half of that of Germany's.(EIA, 2015) Yet according to the reliability indicator System Average Interruption Duration Index (SAIDI), Germany outperformed the U.S. almost 8 to 1, implying that greater stabilization is possible even with more irregular and intermittent energy sources.(LaCommare, 2008; Bundesnetzagentur, 2013)

Grid expansion is "the most important prerequisite to ensuring the greater penetration of renewable energy in electricity production" by the Federal Ministry for Economic Affairs and Energy.(BMWi, 2012) Successful integration of renewables into the electricity sector hinges on successful management and control of the electric grid. Current issues in grid stabilization include, but are not limited to, renewable integration, load leveling, frequency regulation, peak shaving and off peak storage, transient stability, congestion relief, power quality, and time shifting.(DOE, 2013)

One approach to greater grid stabilization comes in the form of energy storage, which can increase renewable penetration by storing intermittent sources for later use, providing

improvements in load leveling, frequency regulation, power quality, and peak shaving, depending on the technology used. In the United States, most policy concerning energy storage comes in the form of a Renewable Portfolio Standard (RPS), which mandates that a certain amount of electricity delivered must come from a renewable source. RPS differ from state to state in amount mandated, the units in which the mandate is expressed, and what technologies are eligible. As of 2012, 29 states have RPS policies (with 7 states having non-binding goals) toward increasing renewables in their energy mixes,(Barbose, 2012; NREL, 2014) with many states including various storage technologies as eligible in their RPS. However, within the U.S., California is unique in enacting the first energy storage mandate, Assembly Bill 2514. AB2514, written by Nancy Skinner and signed by Governor Arnold Schwarzenegger, establishes an energy storage target of 1,325MW total for the three independently owned utilities (IOUs) Pacific Gas and Electric Company, Southern California Edison, and San Diego gas and Electric by 2020, with installations completed before 2024. The requirement was initiated according to three guiding principles:

1. Optimization of the grid (including peak reduction, reliability, or deferment of transmission and distribution investments)
2. Integration of renewable energy
3. Reduction of green house gas emissions to 80% below 1990 levels by 2050 (CPUC, 2013b)

The ruling proposing storage procurement targets, for the reason that "additional market barriers for emerging storage technologies will only diminish through a procurement process" The Assigned Commissioners Ruling (ACR) specifically refers to storage systems that have not yet realized large-scale commercial operation ("may have been demonstrated but are not yet deployed on the grid in California"), and thus benefit from long-term investment. As it is intended to promote emerging storage technologies, the California Public Utilities Commission has put in certain provisions. First, pumped hydro storage >50MW is not to be counted towards procurement targets. This is because pumped hydro "may not face all of the same types of barriers and issues" as well as to encourage a broad range of technologies. Second, the target is at its lowest in the first solicitation year, 2014, and will ramp up by approximately 33% every two years. This allows for a cushion in learning, as well as gives room for the possibility of cheaper and more cost-effective technologies given more investment. Third, no more than 50% of these targets can be met with IOU owned storage systems. Fourth, the commission is relatively flexible with respect to procurement targets to allow for flexibility in commercial operation for relatively new technology. Thus, IOUs are allowed to shift up to 80% of their storage technology between the transmission and distribution end uses (however, cannot shift in or out of consumer end use). (CPUC, 2013a)

1.6 Scope

The scope of this dissertation aims to investigate a subset of the technology available to address these issues. Specifically, this work focuses on both nanoscale energy conversion and energy storage, through a lens of manipulating device architecture at the electrode. In doing so, this work aims to leverage the physical: drastically improving device performance by carefully modifying the structure of the electrode. In addition, tools to atomically modify physical structures are employed, inducing electrochemical surface effects that further improve device performance. The principles of using a physical/electrical template, modified to induce electrochemical enhancement are demonstrated in 5 unique works in this dissertation (Figure 1.10): (1) atomic layer deposition of titanium-nitride on carbon nanotubes for supercapacitor applications, (2) two-dimensional iron-phosphate for supercapacitor applications, (3) thiophene-based electrodeposition for photoelectrochemical water splitting, (4) titanium dioxide-coated zinc oxide nanowire arrays for photoelectrochemical water splitting, and (5) development of atomic layer deposited black titania for photoelectrochemical water splitting.

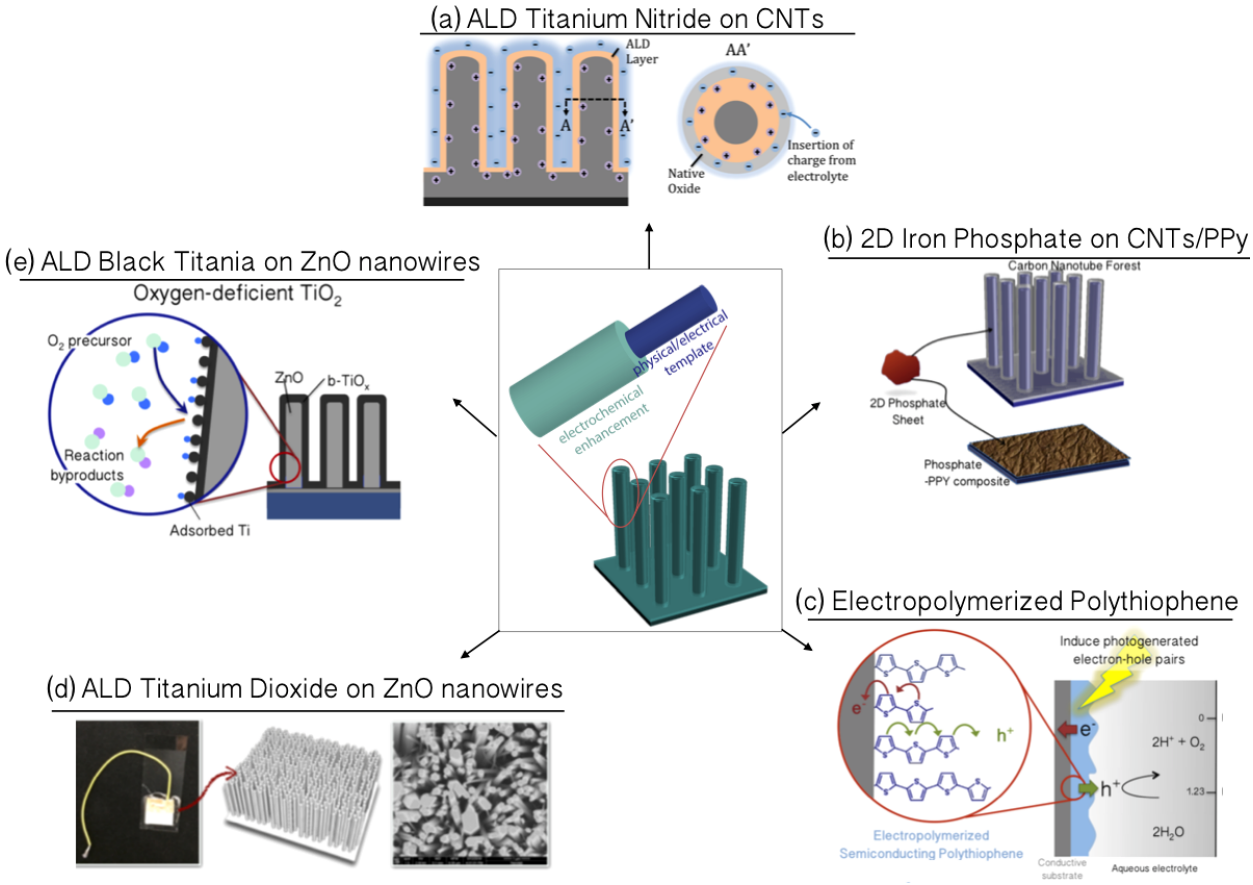

Figure 1.10: The principles of using a physical/electrical template, modified to induce electrochemical enhancement are demonstrated in 5 unique works in this dissertation: (a) atomic layer deposition of titanium-nitride on carbon nanotubes for supercapacitor applications, (b) two-dimensional iron-phosphate for supercapacitor applications, (c) thiophene-based electrodeposition for photoelectrochemical water splitting, (d) titanium dioxide-coated zinc oxide nanowire arrays for photoelectrochemical water splitting, and (e) development of atomic layer deposited black titania for photoelectrochemical water splitting.

Chapter 2

Titanium Nitride-Based Supercapacitors

Titanium nitride (TiN) coating on vertically aligned carbon nanotube (VACNT) forest electrodes by means of atomic layer deposition (ALD) to store charge in electrochemical supercapacitors is demonstrated. Experimental results show that after 400 cycles of ALD processing, a roughly 20nm-thick TiN layer is coated uniformly on individual CNTs in the forest electrode. The electrochemical characterizations show 2000 times higher capacitance of the ALD TiN-CNT device as compared to that of a flat TiN electrode. Furthermore, over 500% enhancement in electrochemical capacitance of the ALD TiN-CNT device ($81 mF/cm^2$) as compared to bare CNT forest electrodes ($14 mF/cm^2$) is been accomplished due to the increased oxygen vacancies on the TiN surfaces. As such, this work presents a new path to increase energy density of supercapacitors using TiN-based porous electrode materials.

In this chapter, mechanisms behind energy storage using supercapacitors are introduced and motivated as a potential solution to achieving grid stability. The atomic layer deposition method is introduced and the corresponding performance is evaluated.

2.1 Achieving Grid Stability Using Supercapacitors

Electrochemical supercapacitors hold a unique position in grid stabilization applications, with high power density, translating to quick charge/discharge cycles, and the potential for high stability. However, the limiting factor in supercapacitors is its energy density as compared to batteries or other high energy density storage devices. Because of these traits, electrochemical supercapacitors are best suited for power quality applications and frequency regulation, as reported by the Department of Energy, (DOE, 2013) but have not been widely deployed in grid applications due to their relatively nascent state of technological advancement. Supercapacitor characteristics in power and energy density arise from the charge storage mechanisms used in supercapacitor devices. Early electrochemical supercapacitors

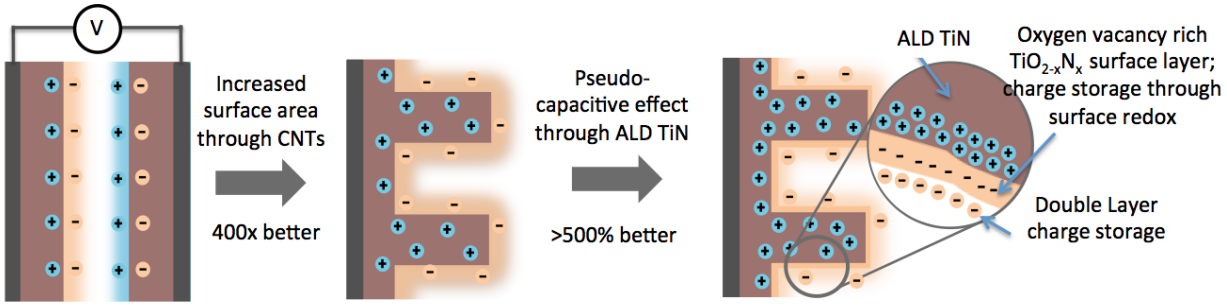

Figure 2.1: Conceptual illustration of increasing capacitance through increased surface area and the pseudo capacitive effect. The storage and release of electrical charge occurs by adsorption and desorption of charge on the surface of TiN (Double Layer charge storage) as well as oxidation of the surface layer. This surface layer of $TiO_{2-x}N_x$, which forms as a native oxide layer, has a high nitrogen concentration, with a large number of oxygen vacancies in the surface. Both charge storage mechanisms combine to increase capacitance in the device. The current then flows through the ALD TiN and CNTs.

achieved charge storage through double layer capacitance, achieved when ions from the electrolyte collect on the surface of the electrode. Since the number of ions that can gather at the surface is directly proportional to surface area, the energy storage of these electrodes can be further increased through texturization of electrode surface.

This is often achieved by using high surface area materials with high intrinsic capacities, such as porous carbon, activated carbon, or carbon nanotubes. These supercapacitors charge and discharge quickly, as the charge is highly mobile and the charge layer forms only at the surface of the material. In contrast, lithium ion batteries have relatively slow charge discharge cycles, as ions must intercalate themselves into the material. Moreover, in the process of intercalation, electrodes may become susceptible to damage. For example, silicon, known as one of the highest energy density lithium ion battery materials, can expand up for 400% upon intercalation. Damage in double layer supercapacitors is minimal, since charge simply gathers on the surface and does not insert itself into the electrode area.

The second mechanism of charge storage in an electrochemical supercapacitor is achieved by reactions occurring in the surface of the electrode, or pseudocapacitance. In contrast to batteries, these reactions are much faster since they occur only on the surface layers of the electrode. However, many pseudocapacitors suffer from poor stability, since electrodes may experience damage from ion insertion or faradaic reactions. These two mechanisms of supercapacitor charge storage working in tandem can dramatically increase the charge storage capacity, depending on the device architecture and faradaic reaction. In our supercapacitor device, we increase the double-layer capacitance by using a vertically aligned carbon nanotube (CNT) forest, a high surface area material. We then further attempt to increase charge capacitance by conformally coating the CNT forest with TiN, which has previously

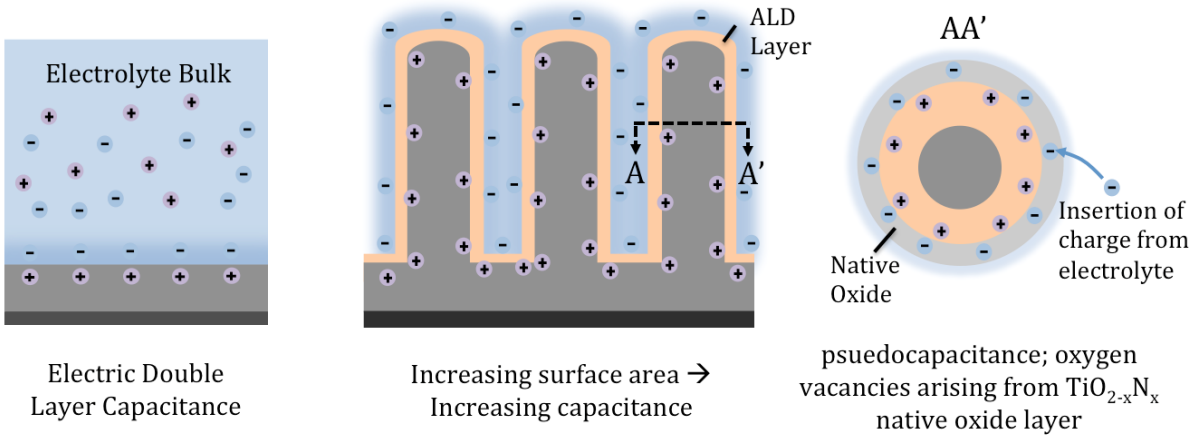

Figure 2.2: Conceptual illustration of our specific design: by employing TiN coatings on VACNT, pseudocapacitance is induced as the oxygen vacancy-rich native oxide layer.

been shown to exhibit faradaic redox surface reactions due to increased oxygen vacancies at the surface (see Figure 6.1).

In our electrode as illustrated in Figure 4.2, we achieve high capacitance by (1) increasing the surface area using the porous CNT forest architecture and (2) allowing for redox reactions to occur in the oxygen vacancy rich TiN surface layer. These results are comparable to other supercapacitor materials deposited by ALD onto vertically aligned CNT structures. (Warren et al., 2015b; Fiorentino et al., 2014) Specifically, the large surface area helps the electric double-layer capacitance as storage/release of electrical charges occurs by the adsorption/desorption of charges on the surface of TiN. The oxidation of the surface layer, $TiO_{2-x}N_x$, forms a native oxide layer with high nitrogen concentration and a large number of oxygen vacancies for the redox reactions, which aid Faradaic electrochemical storage as the pseudo-capacitance enhances energy storage.

2.2 Principles of Electrochemical Double Layer Capacitance

When voltage is applied across two electrodes, separated by an electrolyte, ions in the electrolyte will accumulate at the surface of the electrode of opposite charge. This phenomena is Electric Double Layer Capacitance (EDLC) and can be described by the capacitance equation:

$$C = \frac{\epsilon A}{d} \tag{2.1}$$

where A is surface area and d is distance between two charge layers. As opposed to a conventional capacitor, where two oppositely charged electrodes are separated by a non-conducting dielectric layer, EDLC effectively doubles the active area, allowing for positive and negative charge accumulation at each electrolyte-electrode interface. Moreover, EDLC experiences drastically reduced distances between oppositely charged layers, since mobile ions in the electrolyte are separated from charged electrodes only by solvation sheaths. (Winter and Brodd, 2004) In an aqueous electrolyte, the distance between charge layers is on the order of the diameter of an H_2O molecule. (Srinivasan, 2006)

It thus stands to reason that an increase in active surface area will proportionally increase capacitance due to EDLC.

2.2.1 Structure of the Double Layer

Surface charge regions characterized by distinct governing principles of charge distribution comprise the structure of the EDLC, depending on the size of ions within the electrolyte. A representative depiction of aqueous electrolyte with large anions and smaller cations is shown in Figure 2.3.

Far from the electrode surface exists the electrolyte bulk. This behaves as an electrically neutral layer, with solvation sheaths gathered around the smaller ions (represented as glow borders in Figure 2.3). Closer to the electrode surface exists the Guoy-Chapman layer, where ion distribution as a function of distance from the electrode surface is governed by Maxwell-Botlzmann statistics. For this model, charge in a 1-1 electrolyte can be represented as:

$$q = \frac{2kTn_0\epsilon}{\pi} sinh \frac{e_0 V}{2kT} \tag{2.2}$$

where q is the diffuse charge, k is Boltzmann's constant, T is temperature, n_0 is the number of ions of positive and negative sign per unit volume in the bulk, ϵ is the dielectric constant in the medium between the plates, and V is the potential drop from the metal to the bulk of the electrolyte. Differential capacity is subsequently (Srinivasan, 2006; Stern, 1924)

$$C = \frac{n_0 \epsilon e_0^2}{2pikT}^{1/2} cosh \frac{e_0 V}{2kT} \tag{2.3}$$

Approaching the electrode surface, there exists an outer and inner Helmholtz layer, representing ions that have adsorbed onto the surface of the electrode, represented by a linear potential drop across the interface, with a capacitance of

$$C = \frac{\epsilon}{4\pi d} \tag{2.4}$$

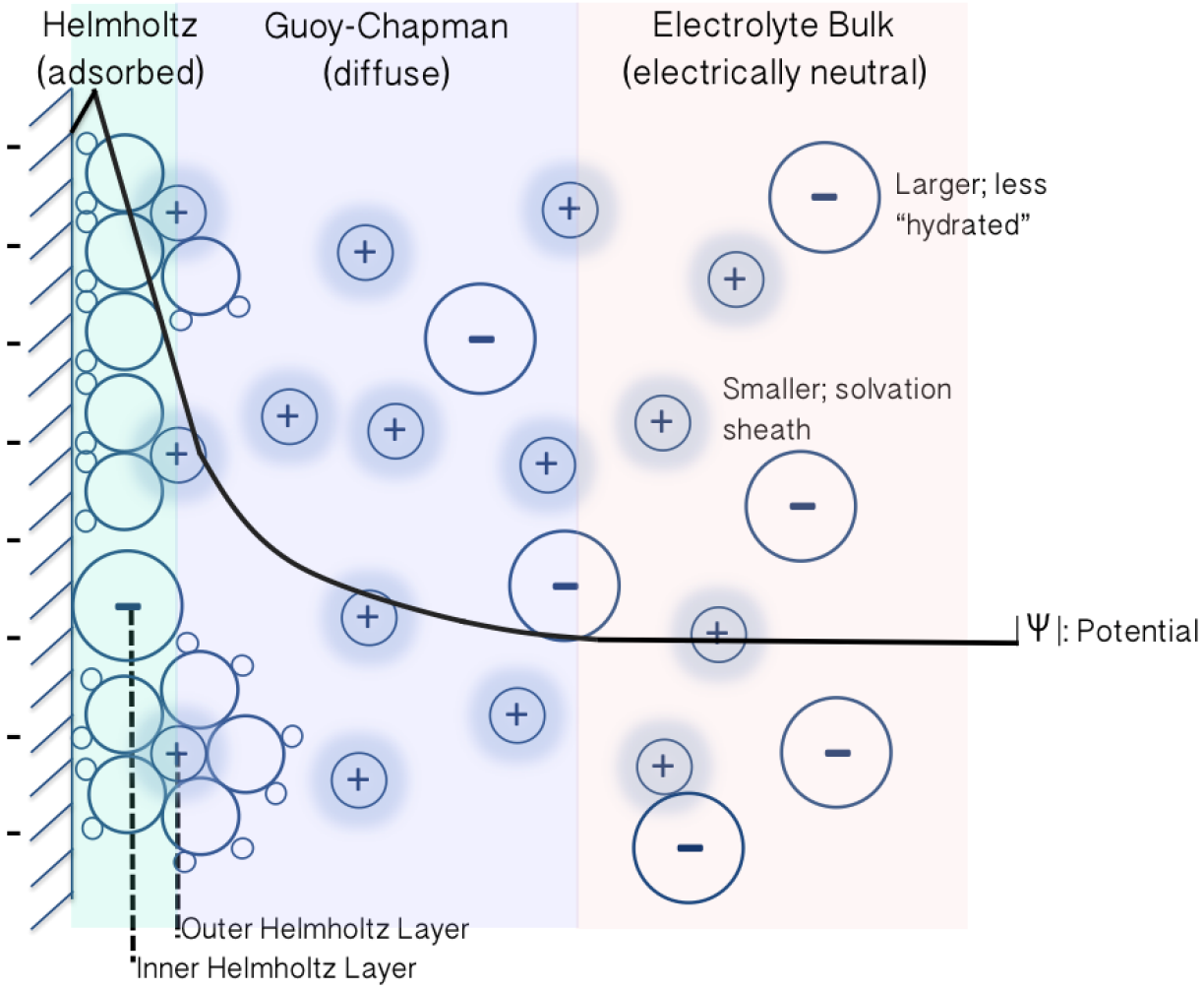

Figure 2.3: Conceptual illustration of the structure of the electrochemical double layer

In the outer Helmholtz plane, d is roughly the diameter of the molecule that comprises the solvation sheath around an ion. In Figure 2.3, this is represented as water molecules around the smaller, positive ion. The inner Helmholtz layer accounts for dehydrated ions specifically adsorbed onto the electrode. In Figure 2.3, this is represented as a larger anion, which is known to have fewer water molecules in the primary hydration sheath. (Grahame, 1951; Srinivasan, 2006)

2.3 Principles of Pseudocapacitance

Pseudocapacitance is a Faradaic charge transfer at the surface of an electrode-electrolyte interface whose capacitance contribution can be orders of magnitude higher than that of

EDLC electrodes for the same surface area and electrolyte. (Conway et al., 1997).

Examples of common pseudocapacitive mechanisms include

1. Faradaic redox, wherein at a given potential, the oxidation state of surface atoms at the electrode-electrolyte interface are altered. Depending on the applied potential, the surface of an electrode can either be reversibly reduced (decrease in oxidation state) or oxidized (increase in oxidation state).

2. Intercalation, wherein ions are physically inserted into the electrode lattice. This is the principal mechanism by which secondary batteries achieves energy storage and will be a focus psuedocapacitance in Chapter 3.

3. Underpotential Deposition, wherein the electrode is held at a potential lower than that of equilibrium, causing ions to reduce (deposit) onto the surface of the material.

4. Chemisorption, wherein adsorbed, unsolvated (dehydrated, in the case of aqueous electrolytes) ions experience electron transfer with the electrode surface.

2.4 Supercapacitor Design

As discussed in Section 2.1, in order to maximize energy storage of a supercapacitor, both electric double layer capacitance (Section 2.2) and pseudocapacitance (Section 2.3) must be maximized. To increase EDLC, carbon nanotubes were chosen for their high surface area and conductivity. Though single-walled CNTs, cylindrical, single-layer graphene, are known to be either metallic or semiconducting, multiwalled CNTs, concentric tubes of single-layer graphene, are highly conductive and largely metallic. (Baughman et al., 2002) Figure 2.4 shows a transmission electron microscopy (TEM) image of an as-fabricated CNT, with a diameter of roughly 20 nm and visible walls indicating multi-walled CNT structure. Vertically aligned CNTs, where CNTs, aligned perpendicular to a substrate, create a "forest"-like morphology. The highly-ordered, highly-porous forest structure allows for large surface areas.

Titanium nitride thin films have been widely used as the protection coatings in machinery and contacts in microelectronics due to the exceptional hardness, mechanical stability, biostability, and electrical conductivity achieved by these film. Increased oxygen vacancies through surface behavior of the native oxide in TiN films have also led to usages in electrochemical supercapacitors for increased capacitance. For these applications, control over deposition upon irregular surfaces and nanostructures is central in optimizing performance. However, previous titanium nitride supercapacitors have been limited in geometry or surface functionalization due to the difficulty of precise fabrication. These electrodes are fabricated through a two-step, high temperature process, limiting selection of high surface area electrode materials, (Jun et al., 2009; Lu et al., 2012) or deposited by sputtering with poor conformality and coverage. (Achour et al., 2017) Here we present results from depositions of

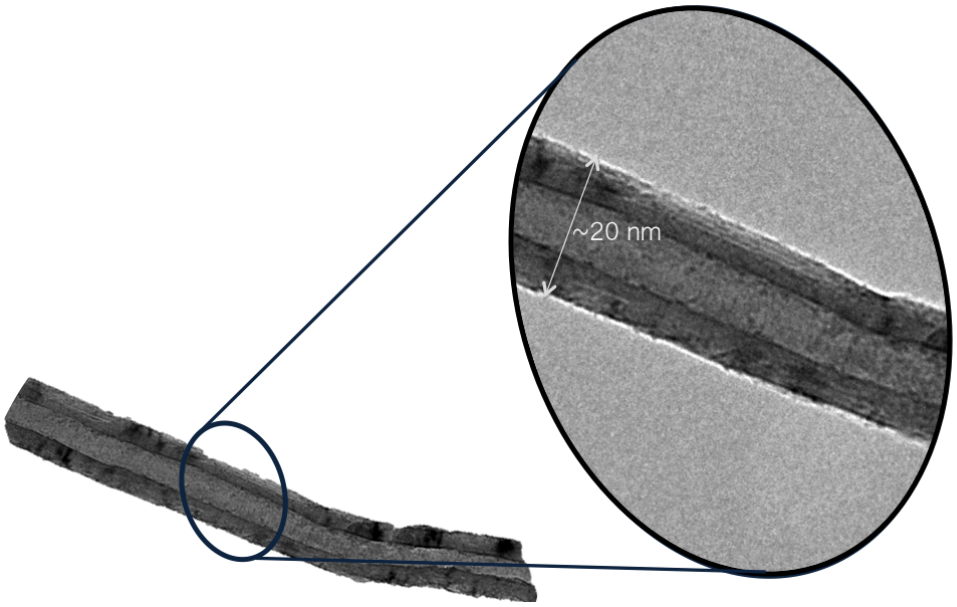

Figure 2.4: TEM image of a single as-grown, multi-walled CNT with a diameter of 20 nm.

Ångström-level precision ALD TiN onto porous CNT forest electrodes and their outstanding performances in the supercapacitor electrode applications.

2.5 Fabrication

The CNT forest is grown as shown in Figure 2.5. First, a silicon substrate is prepared with 100 nm thermally grown oxide. Next, a thin layer of molybdenum is deposited by electron-beam evaporation to form a conductive layer. The catalyst is a thermally evaporated mixture of 5 nm iron and 5 nm aluminum, with aluminum acting to prevent molybdenum and iron from forming an alloy. The substrate is transferred to a vacuum quartz tube furnace to grow the CNT forest by chemical vapor deposition (CVD), as outlined by Yingqi Jiang et al. (Jiang et al., 2009) Once the temperature of the furnace is stabilized at 720 °C, the process gases, hydrogen and ethylene are introduced in a 7:1 ratio with respect to volumetric flow rate. When heated to high temperatures, the catalysts nucleate and form droplets on the conductive surface, forming the basis for the CNT forest. At this high temperature, when placed in an ethylene rich environment, the CNTs are then grown by CVD.

TiN is ALD deposited using Tetrakis (dimethylamido) titanium (TDMAT) and nitrogen plasma as precursors. The process is highly dependent on ALD configuration, temperature, precursors, and is especially sensitive to atmospheric contaminants.

A Cambridge Nanotech Fiji tool was used to deposit the TiN. ALD deposition was tested for 200 °C, 250 °C, and 300 °C, as shown in Figure 2.6. Ultimately, TiN films deposited

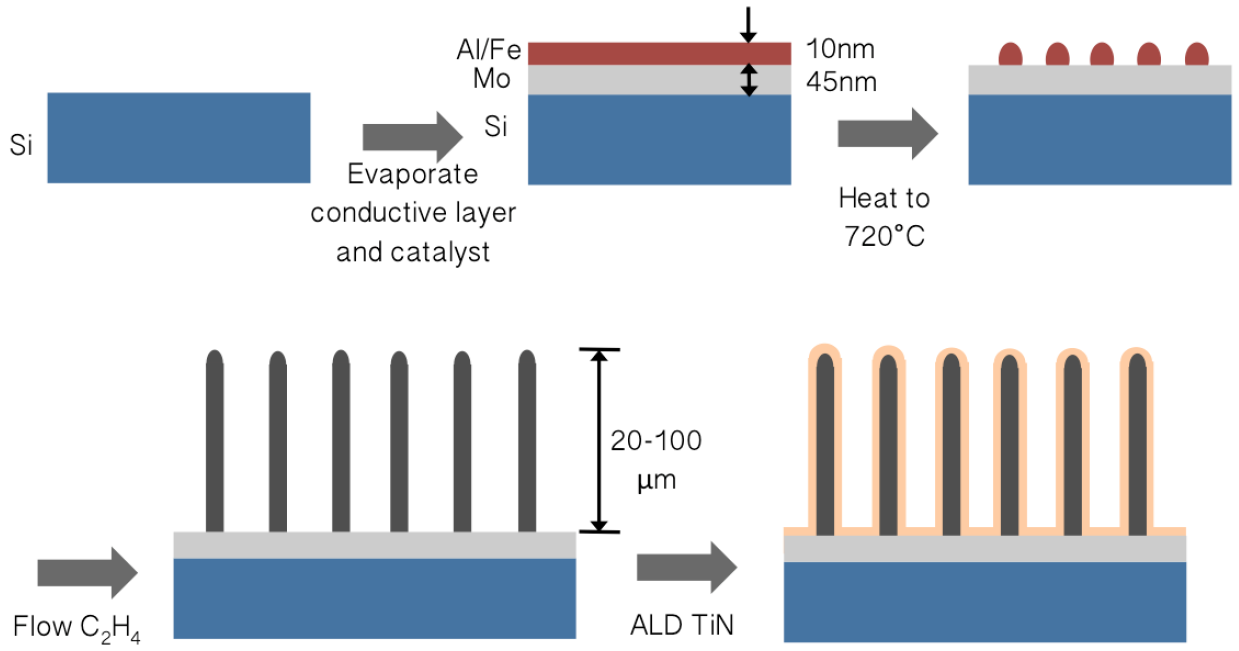

Figure 2.5: Process flow of substrate fabrication. Steps a-c show preparation of the CNT substrate before growth. This is carried out by evaporating a conductive layer and catalyst onto a silicon substrate with thermally grown oxide. When heated, the catalysts form droplets, which form the basis for CNT growth. In an ethylene environment, a vertically aligned CNT forest is grown by CVD (step d). Finally, in step e, TiN is deposited conformally onto the CNT forest using ALD.

at 250 °C were used as the temperature in Cambridge Nanotech's standard TiN recipe. Additionally, as shown in Figure 2.6, films deposited at 250 °C show the lowest oxygen to titanium ratio, indicating a higher amount of TiN in the sample. TDMAT heated to 75 °C was pulsed for 0.25 s, and N_2 plasma pulsed for 20 s at an overall chamber temperature of 250 °C, with purge steps of 6 s and 5 s, respectively, between the precursor steps. The pressure was on the order of millitorrs. The growth rate is roughly 6 Å/cycle. The as deposited film forms a native oxide in the presence of atmosphere, which is exacerbated in high temperature environments. Therefore, the deposited film is left to cool for 30 minutes–1 hour under vacuum environment.

2.6 Characterization

Figure 2.7 shows SEM images of vertically aligned CNT forest coated with ALD TiN. As the images show, a CNT forest of roughly 30 μm in height was successfully grown, corre-

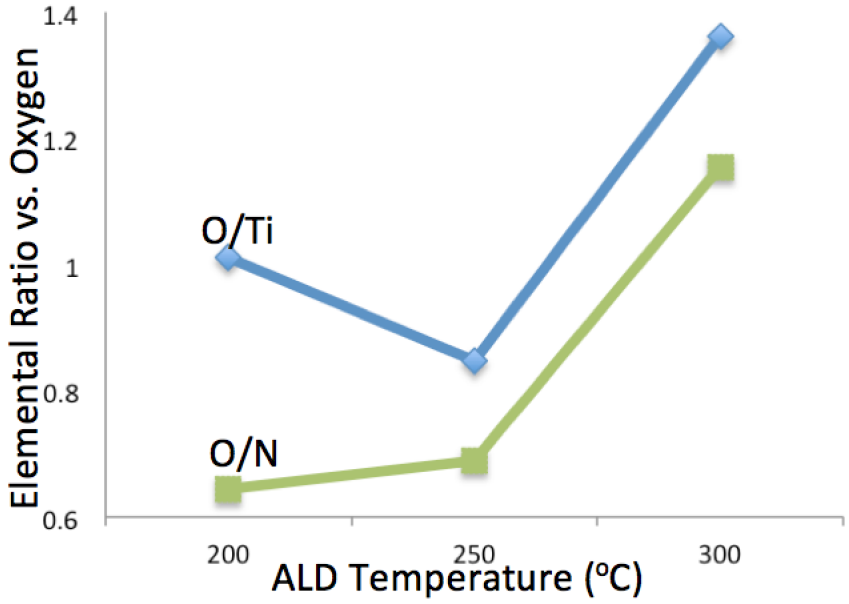

Figure 2.6: XPS (X-ray photoelectron spectroscopy) analysis of composition versus ALD temperature. Note the high oxygen content, a result of the $TiO_{2-x}N_x$ surface layer.

sponding to 20 minutes of growth time in an ethylene environment. Figure 2.8 show the TEM image of coated CNTs, showing conformal coating and uniform thickness of the ALD TiN, corresponding to 400 cycles of ALD. The CNT has diameter of 20 nm and the TiN is roughly 20 nm in thickness, consistent with the growth rate for this TiN recipe.

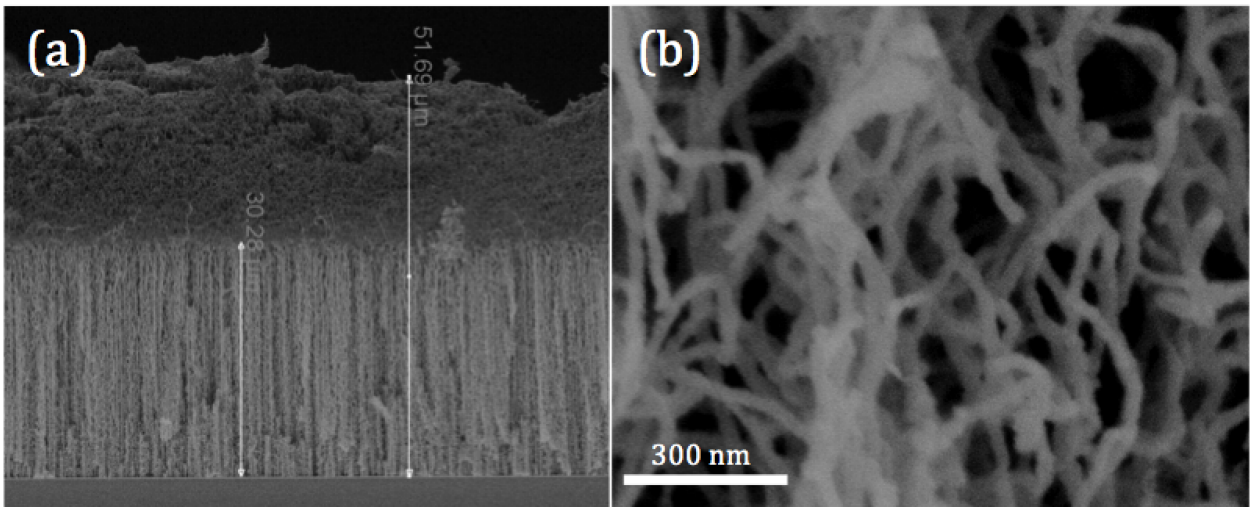

Figure 2.7: a) SEM image of TiN-coated CNT forest showing conformal coating of the approximately 30m tall forest. b) SEM image of the bottom of the TiN-coated CNT forest.

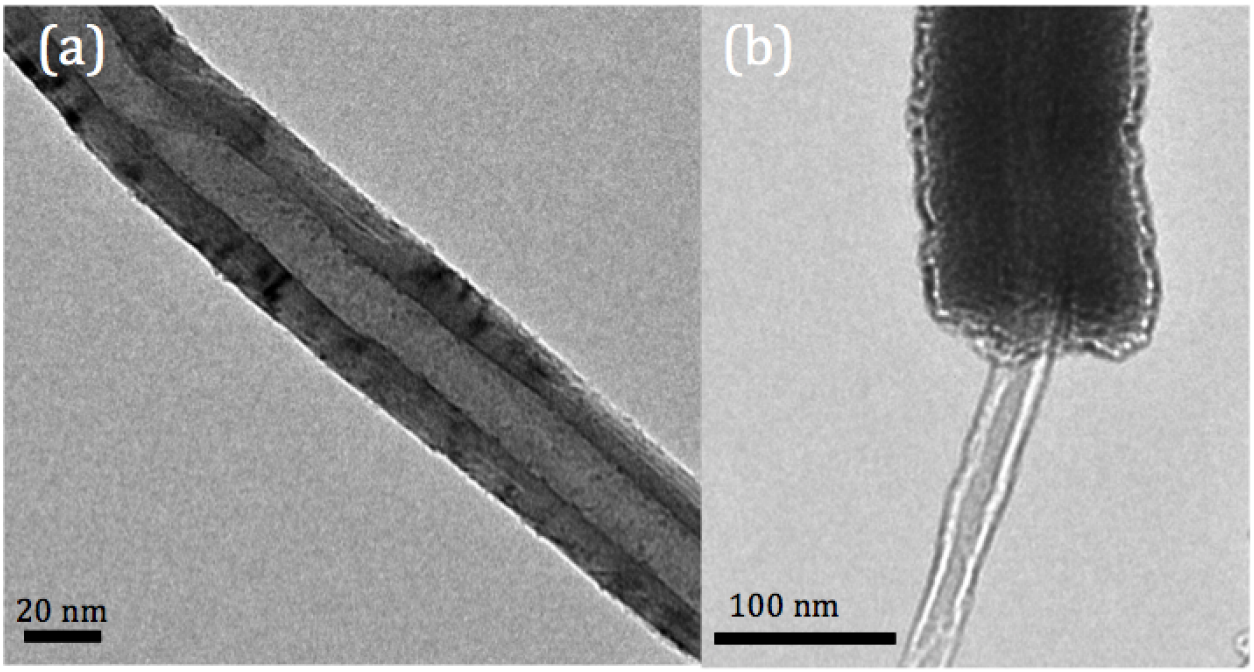

Figure 2.8: a) TEM image of a single carbon nanotube. b) TEM image of TiN-coated carbon nanotube

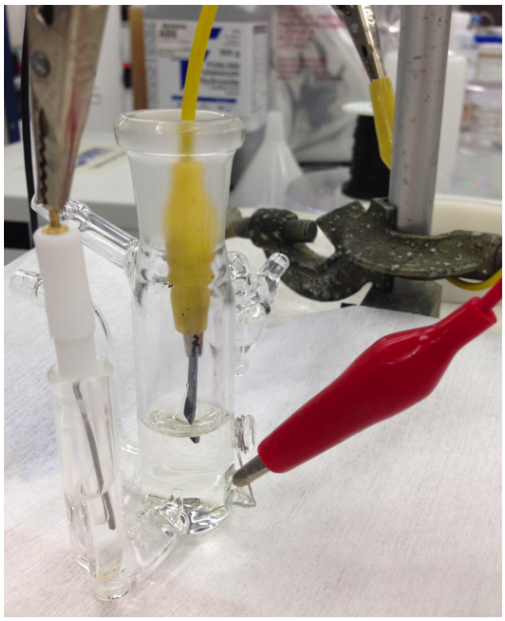

Figure 2.9: a) TEM image of a single carbon nanotube. b) TEM image of TiN-coated carbon nanotube

2.6.1 Electrode Testing

The electrode was tested using a three-electrode setup in aqueous and organic electrolyte. Electrodes were used as prepared and tested with Pt wire as the counter electrode. In aqueous 0.5 M H_2SO_4 solution, measurements were taken vs. an Ag/AgCl reference electrode. In non-aqueous 0.1 M tetrabutylammonium hexafluorophosphate solution (dissolved in acetonitrile), measurements were taken vs. an Ag/Ag+ reference electrode. (see Figure 2.9).

2.7 Electrochemical Characterization and Performance

2.7.1 Cyclic Voltammetry

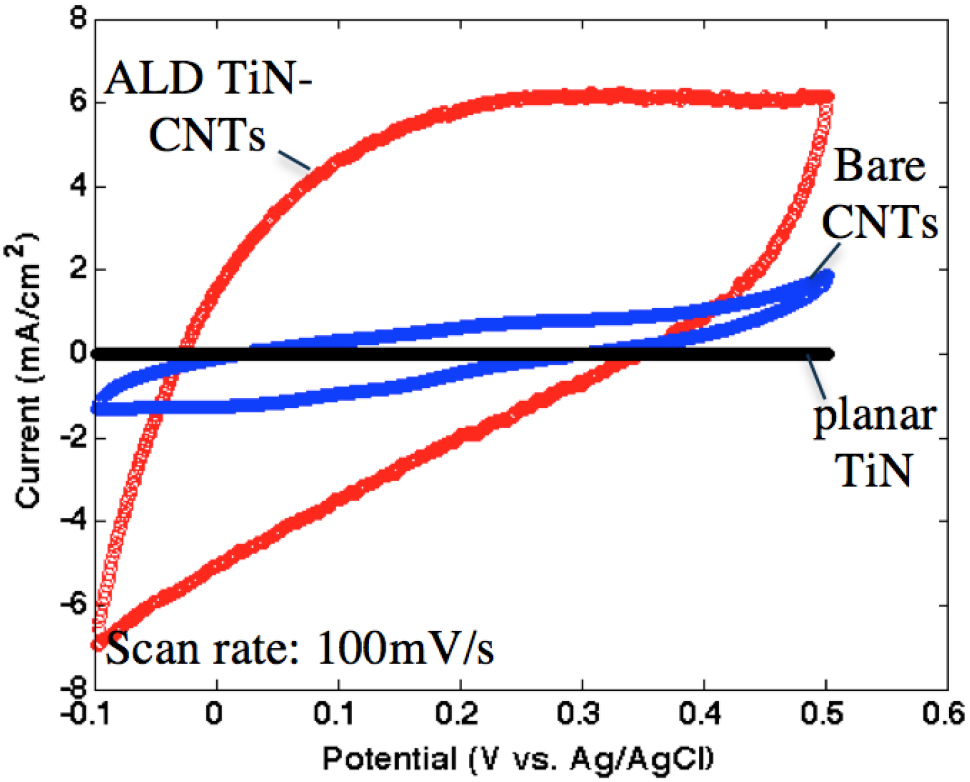

Figure 2.10: Cyclic Voltammograms (CVs) of ALD TiN-CNTs as compared with bare CNTs and planar TiN, corresponding to 81 mF/cm^2, 14 mF/cm^2, and 0.2 mF/cm^2, respectively. CVs tested vs. Ag/AgCl.

TiN-CNT, CNT, and planar TiN electrodes were tested using a three-electrode setup with 0.5 M H_2SO_4 as electrolyte, Pt wire as counter electrode, vs. Ag/AgCl as shown in Figure 2.9. The cyclic voltammetry curves show an improvement of >500% in capacitance

of the TiN-CNT device relative to that of bare CNTs (81 mF/cm^2 for TiN-CNT and 14 mF/cm^2 for CNT electrodes), and the bare CNTs show an almost 400x improvement in capacitance relative to planar TiN electrodes (0.2 mF/cm^2).

The significance of surface area on supercapacitor charge storage is shown in Figure 2.10, wherein using a porous CNT framework increases capacitance almost 400x over that of a planar TiN electrode. Furthermore, the improvement of >500% in capacitance by conformal coating of TiN indicates that charge storage in the TiN-CNT device does not only take place via ion adsorption/desorption but also through Faradaic redox reactions, or pseudocapacitance. By increasing surface area, one can drastically improve supercapacitor performance. In contrast to current electrochemical supercapacitor work using TiN, ALD allows for robust coating, conformal coating, and angstrom level precision, providing both great flexibility in choice and architecture of the device and potential for increasing surface area.

2.7.2 Impedance Spectroscopy

Figure 2.11a shows electrochemical impedance spectroscopy of the TiN-CNT electrode, with two clear regimes of double-layer capacitance at high frequencies and diffusion-limited capacitance at lower frequencies, corresponding to the electric double-layer storage mechanism and pseudocapacitive storage mechanism, respectively. The Randle's cell (Figure 2.11) represents a first-order equivalent circuit approximation of an adsorption/desorption and diffusion model that has been fitted to experimental data, showing the trends of storage mechanisms in the device. In the model, adsorption is represented by a constant phase element, corresponding to double-layer capacitance, and pseudocapacitance is represented by the Warburg impedance, a diffusion-limited impedance. The Randle's cell fit for the electrode in aqueous solution is shown in Figure 2.11b, c and show poor agreement in the low-frequency range because, in practice, Warburg impedance is not ideal. In the low-frequency (diffusion-dominated) regime, behavior in the model is determined largely by the Warburg impedance, which is modeled as ideal. In practice, while diffusion behavior can be approximated by ideal Warburg impedance, behavior in porous pseudocapacitive electrodes have shown to have dependencies on conductance of the solution and properties of the porous electrode structure. (Tilak et al., 1992)

Pseudocapacitive effects most likely arise due to increased oxygen vacancies within the native $TiO_{2-x}N_x$ layer that forms upon exposure to the atmosphere. As seen in Figure 3a, the oxygen content in the surface of the electrode, as measured using XPS, is relatively high, implying a high-oxygen concentration in the native oxide layer. Furthermore, nitrogen doping of titanium dioxide materials has been shown to increase oxygen vacancies, thus increasing the potential for charge insertion and storage. The ability to store more charge results from the reorganization of electrons associated with the absent oxygen. The defect state has been shown to be introduced at approximately 0.8 eV below the valence band, (Pacchioni, 2015) implying that the electrons are fixed, not mobile. These electrons are transferred into empty

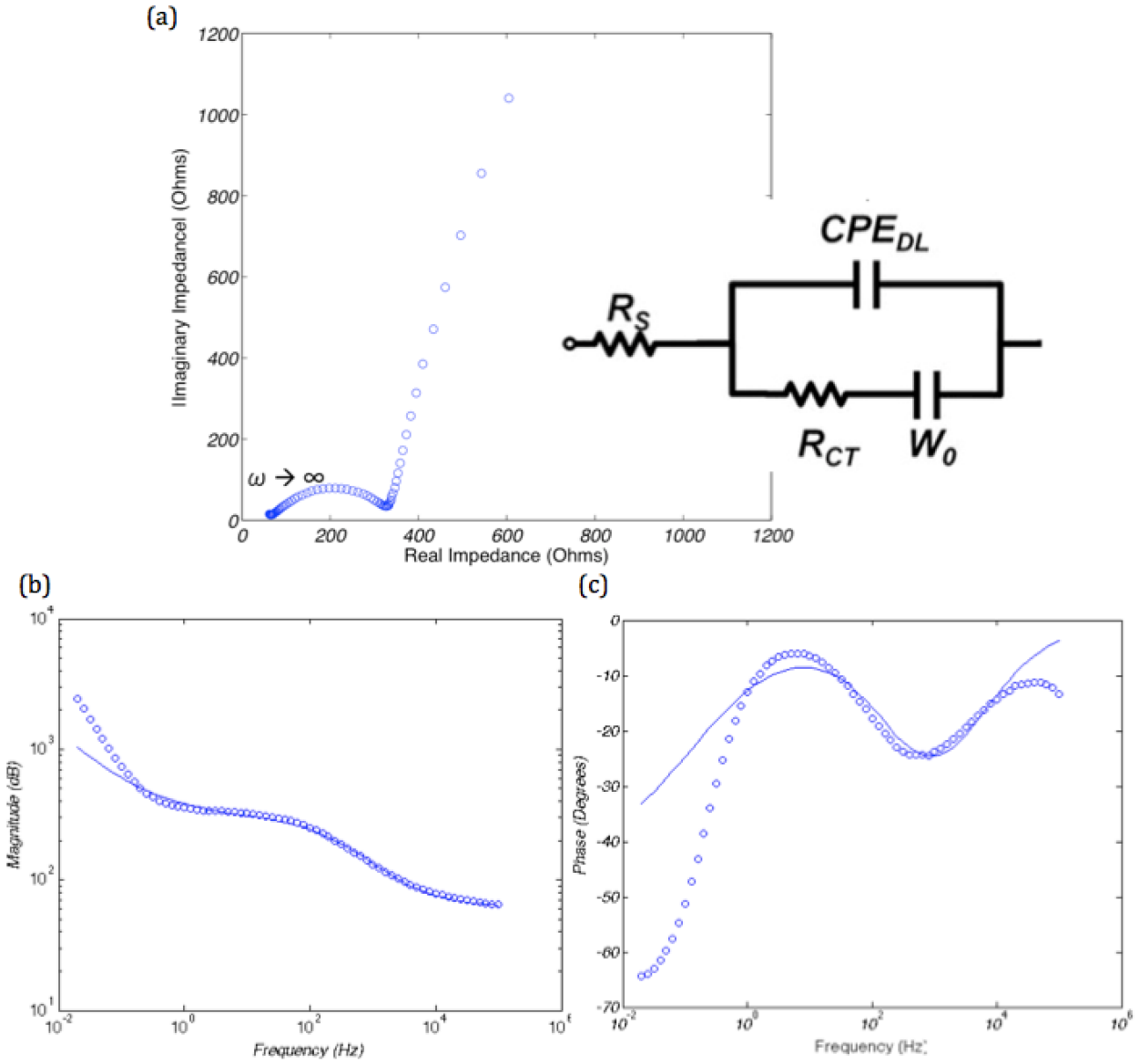

Figure 2.11: (a) Nyquist plot of Electrochemical Impedance Spectroscopy (EIS) for ALD TiN-CNTs in aqueous solution. The two regimes, corresponding to double layer capacitance effect and the diffusion limited region, show both pseudocapacitance as well as electric double layer capacitance. (inset) first order model of Randle's cell to model pseudocapacitive devices. (b)(c) Bode plot of ALD TiN-CNTs with Randle's cell fit. At lower frequencies, the fit estimates poorly (underestimates in Magnitude, overestimates in Phase). This is due to the use of an ideal Warburg impedance in the model.

3d orbitals belonging to adjacent titanium atoms, resulting in a change of formal oxidation state from Ti^{+4} to Ti^{+3}. (Rumaiz et al., 2009)

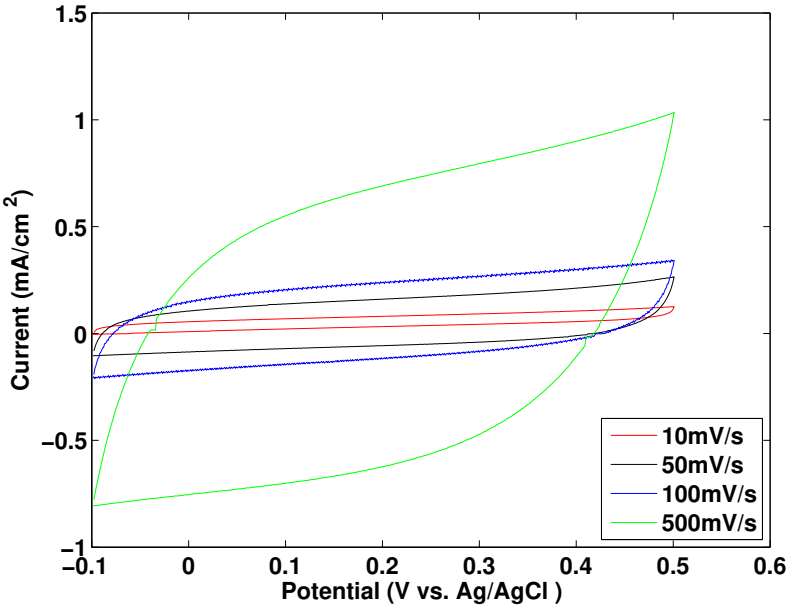

Figure 2.12: Cyclic Voltammograms (CVs) of ALD TiN-CNTs in an organic electrolyte, 0.1M Tetrabutylammonium hexafluorophosphate in acetonitrile at varying scan rates, vs. Ag/AgCl.

2.7.3 Stability

In testing pseudocapacitive devices, stability must be considered, since damage to the electrode can occur from the insertion of ions, or damage to the electrode in the case of non-reversible Faradaic reactions. Over continuous charge/discharge cycles, the device is relatively stable. However, as can be seen in Figure 4b, the reaction is not completely reversible. We hypothesize that this is due to irreversible oxidation at the surface of the TiN electrode.

Existing work on TiN supercapacitor devices has shown relatively stable oxygen vacancies in the presence of non-reversible oxidation due to simultaneous diffusion of nitrogen from the TiN bulk into the native oxide layer. (Achour et al., 2017) In the proposed system, the native oxide layer maintains the same number of oxygen vacancies, as the oxidation occurs through diffusion of oxygen into the bulk while nitrogen simultaneously diffuses from the bulk to the surface layer.

To increase stability, the electrode was tested in an oxygen-free electrolyte of 0.1 M Tetrabutylammonium hexafluorophosphate dissolved in acetonitrile. As shown in Figure 2.12, performance decreases relative to the electrode tested in sulfuric acid aqueous solution (i.e.: magnitude of the aqueous solution as shown in Figure 2.10 is larger than that of Figure 2.12). However, as Figure 2.13 and Figure 2.14 show, the electrode is relatively stable, retaining 90% of its capacity after 300 cycles. As shown in Rohl et. al, (Rohl and

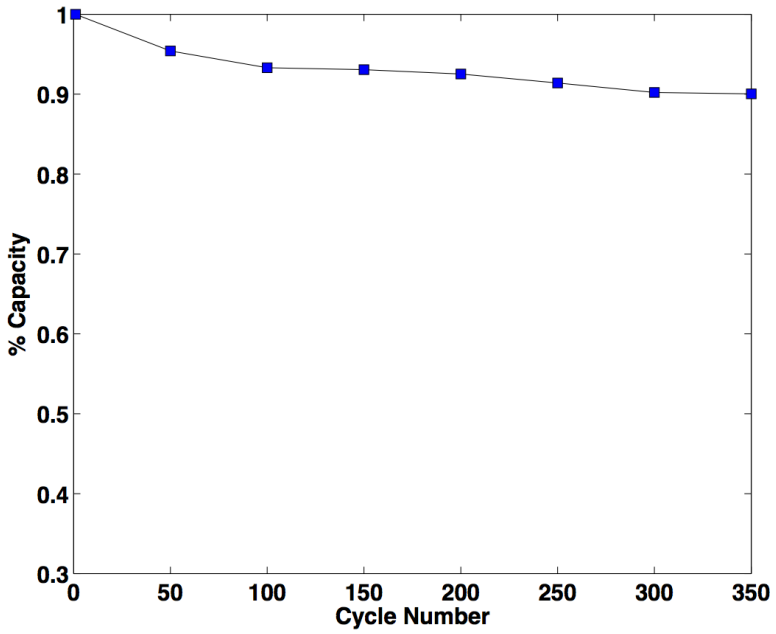

Figure 2.13: Capacity fade over 350 cycles of ALD TiN-CNT electrode in organic electrode.

cycles.png

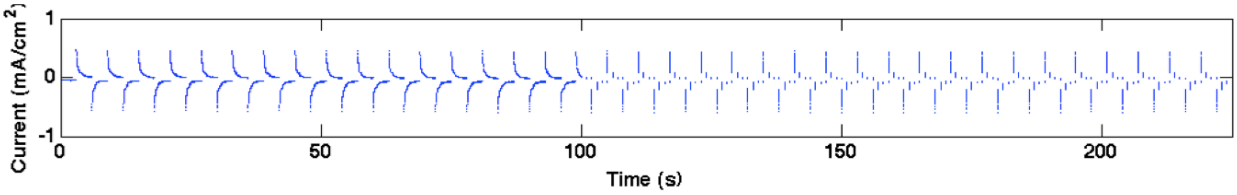

Figure 2.14: Repeated cycling of the supercapacitor device, showing little degradation between cycles.

Mingos, 1993) hexafluorophosphate has a relatively large volume as compared to smaller salts such as sulfates, occupying about 53 Å^3. The reduced performance in organic electrolyte as compared to aqueous sulfuric acid electrolyte may be due to the difference in size of molecules that insert themselves into voids left by oxygen vacancies. Similarly, larger salts can also contribute to faster capacity fade.

2.8 Conclusions

While current technology is limited to a two-step deposition process, or processes with poor conformality such as sputtering, we have achieved a conformal and precise coverage of TiN onto high aspect ratio porous CNT forests for supercapacitor applications. Analysis of our

TiN-CNT architecture shows excellent performance and charge capacity, with the ability to increase performance by taking advantage of the flexibility offered by the precise ALD process. Furthermore, the electrode is relatively stable, with the potential for higher stability using different electrolytes or film thicknesses. Such stability studies are the subject of future work.

Chapter 3

Phosphate-based 2D sheets

This work presents the synthesis, assembly, and integration of two-dimensional (2D) phosphate sheets for lithium ion energy storage devices. Three achievements have been accomplished in this work: (1) synthesis and assembly of 2D, polycrystalline phosphate sheets greater than 50 μm^2 in area, and (2) 3x improved capacitance of an iron phosphate-polypyrrole battery/supercapacitor (3.6 mF/cm^2) over bare polypyrrole (PPY) films, and (3) 20x improved capacitance of an $FePO_4$-carbon nanotube (CNT) battery/supercapacitor (20.8 mF/cm^2) over bare CNT-based electrodes.

In this chapter, the effects of inducing pseudocapacitance via intercalation-based materials is shown. 2D synthesis methods are discussed, with emphasis on wet synthesis as a pathway toward developing instances of phosphate 2D sheets.

3.1 2D Synthesis

Since the inception of graphene in 2004, researchers have sought to fabricate 2D materials, where high surface area increases active sites and results in favorable material properties. Materials with high surface area have been shown to improve both catalytic and electrochemical performance and recent works have opened up pathways into developing scalable synthesis for 2D morphopologies of layered materials, where weak van der Waals forces between planes form naturally layered structures. (Tan and Zhang, 2015; Xiao et al., 2016)

Exfoliation, chemical vapor deposition (CVD), and chemical synthesis have since been developed to fabricate 2D materials. However, both exfoliation and CVD are relatively low-yield, produce sheets with small lateral sizes, and require high-cost processes. Additionally, most processes are only developed for naturally layered materials. In the last few years, chemical synthesis processes have been developed to create 2D sheets of materials that do not naturally occur in layered states. These processes have relied on solvothermal, solution-processed synthesis, capable of bottom-up synthesis with high yield capabilities. However, these methods have largely been only been able to fabricate single precursor materials (metals

and oxides), as opposed to compound materials. (Sun et al., 2014) Furthermore, it has been difficult to fabricate these materials with large lateral areas. This work shows that, for the first time, by using a multiple-precursor solvothermal method, one can construct 2D sheets of iron phosphate ($FePO_4$).

3.1.1 Layered Materials

For the purpose of this dissertation, it is useful to consider the distinction between layered materials, or materials that occur naturally, and non-layered materials, or materials whose bulk forms have never taken a 2D layered structure in nature.

In layered materials, strong bonds in the lateral plane act in concert with weak interactions in the longitudinal plane. These interactions, a result of van der Waals forces, yield atomic layers formed into a bulk material. For example, graphite is a collection of atomically 2D graphene, stacked into a bulk material by van der Waals forces. Other layered materials include transition metal dichalcogenides (TMDCs), monochalcogenides, select oxides (such as [PbO, $Pb_2O(SO_4)$, Na_2PbO_2), and Mxenes. (Novoselov et al., 2016)

In non-layered materials, bonding occurs in 3 dimensions, forming a non-layered bulk material. Of these materials, few have been synthesized to form in a 2D layer. However, using controlled synthesis, noble metals, certain metal oxides (such asTiO_2, WO3, CeO_2, In_2O_3, SnO_2, Fe_2O_3), and certain metal chalcogenides have been formed over the last decades. (Tan and Zhang, 2015)

Methods of 2D fabrication, both of layered and non-layered materials, are summarized below.

3.1.2 Exfoliation

Exfoliation is the first instance of 2D material fabrication, shown with graphene in 2004. (Novoselov et al., 2004) In this process, weak van der Waals interactions between layers are broken to allow for the extraction of a single 2D layer. As a top-down synthesis method for 2D sheets, it relies on a layered heterostructure from which to extract 2D sheets.

3.1.2.1 Mechanical Exfoliation

Mechanical Exfoliation, sometimes referred to as "Scotch Tape" exfoliation, is still employed today for the exfoliation of varying layered materials. The process requires the material to selectively separate one layer only, when exposed to either a normal or shear force. (Yi and Shen, 2015) This force can be employed by adhering a material, or "taping" a material to the surface of the bulk material, releasing a single layer with the adhesion material.

Since the first instance of mechanical exfoliation of graphene using literal Scotch Tape, (Novoselov et al., 2004) advanced mechanical exfoliation systems focus on (1) new "taping"

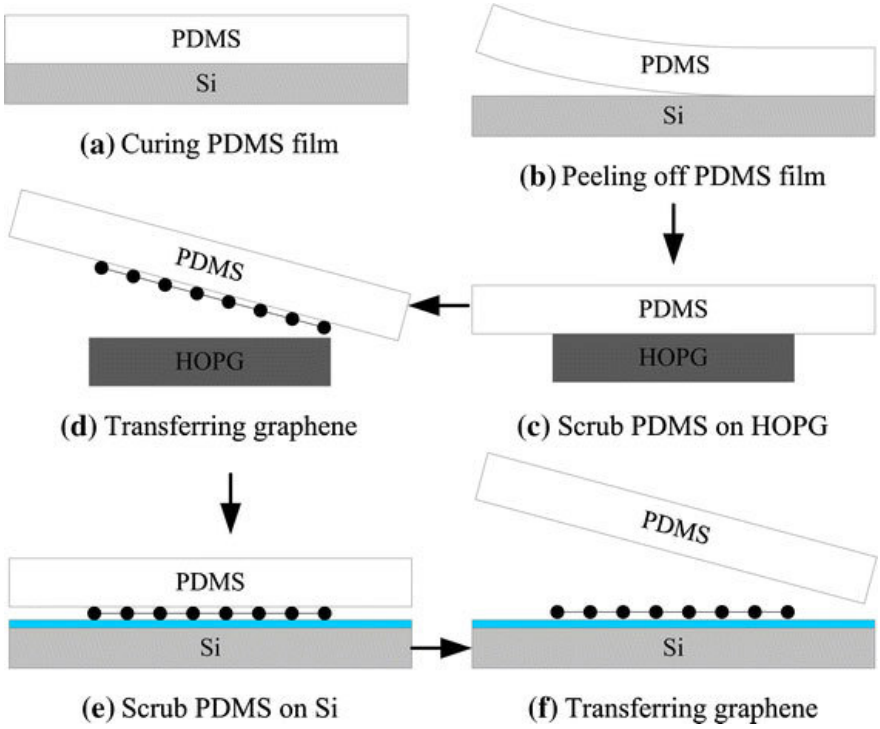

Figure 3.1: An example depiction of mechanical exfoliation, using PDMS (Lee et al., 2009).

layers, utilizing cured polymers (see Figure 3.1), evaporated metals, etc. or (2) extracting large area sheets, since monolayer removal is relatively low-area. (Novoselov et al., 2016). Gold-mediated epitaxy, as reported by the Javey group, was able to achieve around 500μm monolayers of TMDCs. (Zhou et al., 2016).

3.1.2.2 Liquid Exfoliation

For the purpose of this dissertation, liquid exfoliation is distinct from mechanical exfoliation due to the liquid phase and mass production costs. It is distinct from ion intercalation since it does not rely on ions to achieve exfoliation.

Liquid exfolation, as demonstrated for graphene, MoS_2, TMDCs, and other layered materials, has been shown to achieve dispersions of 2D layers in a potentially scalable, process-compatible method.(Coleman et al., 2011; Wang et al., 2015; Nicolosi et al., 2013) However, liquid exfoliation is also relatively difficult to control, with low yields, inconsistent layer numbers, and relatively small lateral size. Furthermore, no definitive method has arisen to separate exfoliated sheets in solution. (Tan and Zhang, 2015)

3.1.2.3 Ion Intercalation

Ion intercalation introduces the separation of layered materials using insertion of ions such as lithium and sodium. In contrast to liquid exfoliation, ion intercalation has been shown to achieve large area sheets up to hundred of microns. (Zheng et al., 2014) In contrast to mechanical exfoliation, ion intercalation is capable of high-yield, scalable processing of layered materials such as graphene, MoS_2, TiS_2, TaS_2, WS_2, ZrS_2 and other TMDCs. (Tan and Zhang, 2015)

However, as with all exfoliation methods, ion intercalation is limited only to layered materials and is unable to be used as a synthesis pathway to non-layered materials.

3.1.3 Chemical Vapor Deposition

CVD is a process by which gaseous phase precursors react on the surface of a substrate, depositing a solid layer. In contrast to exfoliation, CVD is capable of producing 2D sheets of non-layered materials. However, it is highly dependent upon process temperature, pressure, source material, carrier flow rate and distance to the substrate. Its utilization as a 2D synthesis method arose out of the need for a synthesis process that is both scalable and controllable: the bottom-up processing of CVD allows for consistent processing, albiet at energy intensive processing temperatures. (Cai et al., 2018) Moreover, CVD requires high vacuum and yields highly variable results based on the substrate choice. Nucleation and subsequent growth are directly altered by material defects within the substrate, allowing for grain boundaries to form; even in cases of pristine substrates, nucleation and growth were found to preferentially occur on specific facets due to the facet-dependent binding energies of the TMDCs and substrate. (Chen et al., 2015)

3.1.4 Wet Chemical Synthesis

Wet chemical synthesis has been emerging as a method to produce 2D sheets of layered and non-layered materials, in a relatively scalable process. Methods that employ wet chemical synthesis consist of a solution phase reaction, most often aided by surfactants or polymers, yet can obtain 2D sheets of a wide range of materials, including metal oxides, metals, and metal chalcogenides.

Wet chemical synthesis can take many forms, with four major groups (Tan and Zhang, 2015): (1) 2D templated synthesis, where layered materials are used as templates upon which 2D crystals can be formed (Huang et al., 2011); (2) solvothermal synthesis, in which 2D materials are formed under high temperature in a solvent (Duan et al., 2014; Sun et al., 2014); (3) self-assembly, using nanoparticles or nanowires to self-assemble (Schliehe et al., 2010); and (4) soft colloidal templated synthesis, degrading precursors into monomers, which nucleate and directionally grow using a template. (Du et al., 2012)

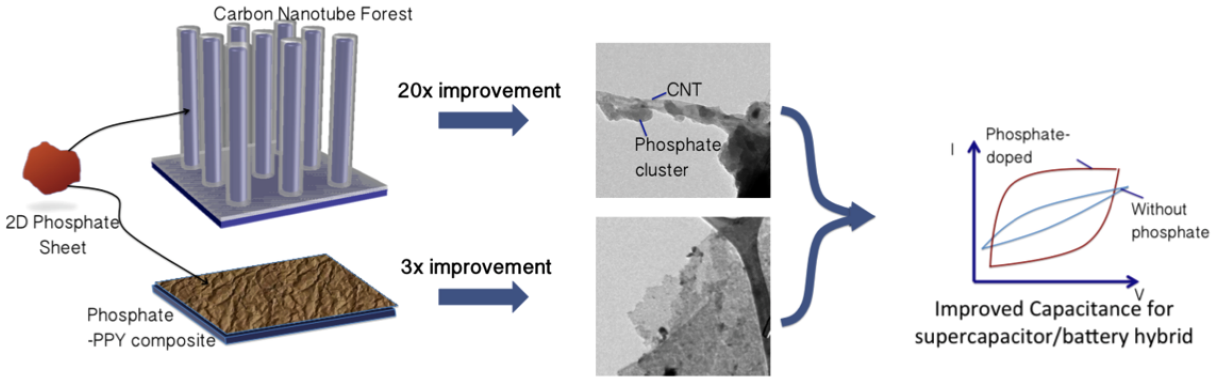

Figure 3.2: By fabricating 2D phosphate sheets and loading them onto vertically aligned carbon nanotube forests and polypyrrole sheets, we achieve 20x and 3x improvement in capacitance, respectively, as compared with previous published works. (Warren et al., 2015a). This is achieved by Lithium ion intercalation into the ultra-high surface area $FePO_4$ sheets.

3.2 Iron Phosphate as electrode material

Lithium iron phosphate ($LiFePO_4$) has been widely considered a compelling lithium-ion battery electrode due to its low cost, non-toxicity, thermal stability, and relatively high specific capacity. However, it's use as a commercial electrode material has been hindered by its low conductivity. Furthermore, synthesis of $LiFePO_4$ has proven difficult for large-scale processing, achieved by solid state reaction, hydrothermal processing, sol gel processing, and precipitation, among others, and requiring high temperature processing, including calcination steps of >500°C. (Jugović and Uskoković, 2009)

In this work, we fabricate hybrid $FePO_4$ electrodes by loading 2D $FePO_4$ onto well-known supercapacitor materials: PPY and porous CNT network. Since $FePO_4$ is capable of lithium ion intercalation, energy density is increased by allowing for bulk diffusion of lithium ions into the thin $FePO_4$. By increasing surface area of $FePO_4$, we are able to maximize contact between the non-conductive sheets and conductive substrates, substantially increasing electrochemical performance.

The newly synthesized $FePO_4$ sheets are integrated into two material systems: (1) CNT forest electrode; and (2) PPY electrode as shown in Figure 6.1. The insets show TEM images of the assembled 2D sheets in the electrodes. We are able to achieve 20x and 3x improvement for $FePO_4$-CNT and $FePO_4$-PPY devices, respectively, as compared to the bare supercapacitive material.

3.3 Fabrication

The sheets are developed in a low-temperature solvothermal process using an organic template. Metal precursor, 10mM iron chloride, is allowed to co-coordinate with a surfactant 20 mM sodium dodecylbenzene sulfonate (SDBS). Formation of $FePO_4$ is induced by a reduction agent (10 nM sodium borohydride) and thermal annealing at 90°C, causing coordinated metal to react with phosphate ions (100 mM sodium phosphate monobasic), to reduce onto the organic scaffold, forming a uniform layer of phosphate material (Figure 6.2). The mixture is then stirred overnight at 90°C, producing suspended $FePO_4$ sheets in water. The surfactant network can be removed by degradation upon post-treatment thermal annealing. TEM imaging of a resulting sheet is shown in Figure 6.2 (inset). By allowing co-coordination, we achieve ultra-thin nanosheets with lateral sizes up to 8μm.

$FePO_4$-PPY devices are fabricated as shown in Figure 3.4. PPY dopant is added into the $FePO_4$ ink during synthesis. Both SDBS and ammonium persulfate were tested as dopants. The $FePO_4$ ink is dropcasted onto a non-conductive glass substrate, surrounded by pyrrole, and covered. Upon evaporation, the pyrrole polymerizes onto the doped $FePO_4$ ink solution, forming a conductive $FePO_4$-PPY film.

The CNT forest is grown by a two-step process. First, a silicon substrate is prepared with 100 nm thermally grown oxide. Next, a thin layer of molybdenum is deposited by electron-beam evaporation to form a conductive layer. The catalyst is a thermally evaporated mixture of 5 nm iron and 5 nm aluminum, with aluminum acting to prevent molybdenum and iron from forming an alloy. The substrate is transferred to a vacuum quartz tube furnace to grow the CNT forest by chemical vapor deposition (CVD), as outlined by Yingqi Jiang et al. (Jiang et al., 2009) Once the temperature of the furnace is stabilized at 720°C, the process gases, hydrogen and ethylene, are introduced in a 7:1 ratio with respect to the volumetric flow rate. When heated to high temperatures, the catalysts nucleate and form droplets on the conductive surface, forming the basis for the CNT forest. At this high temperature, when placed in an ethylene rich environment, the CNTs are then grown by CVD.

The porous forests are vacuumed for 20 min to evacuate air from the substrate. As $FePO_4$ ink is loaded onto the vacuumed CNTs, negative pressure causes the ink to penetrate into the forest (Figure 3.5). After evaporation, the CNT forest is coated with $FePO_4$ sheets (Figure 6.1 (inset)).

3.4 Electrode Testing

The electrode is tested using a three-electrode setup in lithium-rich electrolyte. Electrodes were tested electrochemically using a Ref 600 Gamry Potentiostat. Cyclic Voltammetry was conducted vs. Ag/Ag+, with a platinum counter electrode, and lithium perchlorate in acetonitrile as the electrolyte.

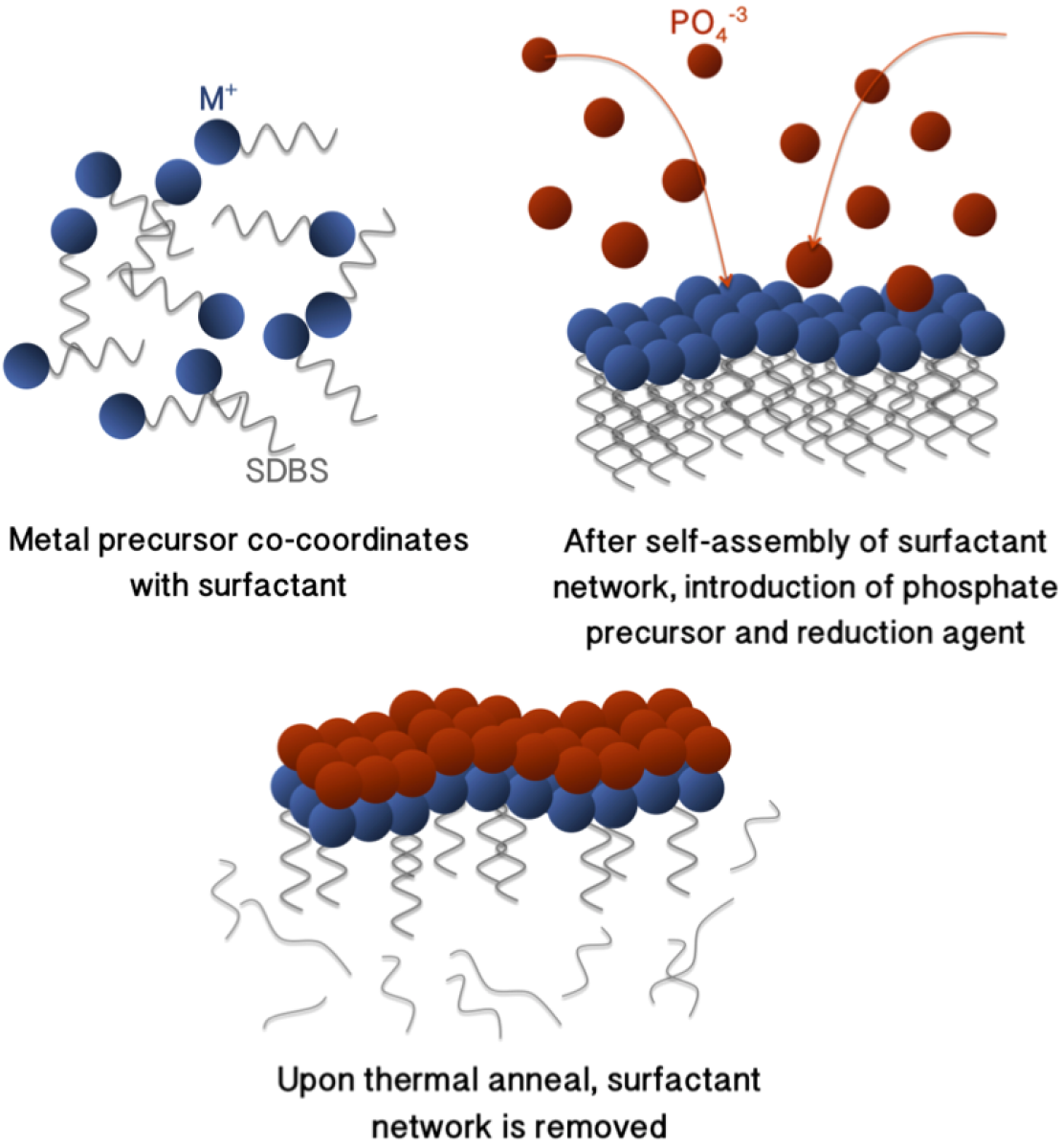

Figure 3.3: Representation of the phosphate self-assembly process. First, metal precursors are allowed to co-coordinate with SDBS and self-assemble before the addition of phosphate precursor. At 90°C, the reducing agent causes the precursors to react. The surfactant network can be removed by post-treatment thermal annealing.

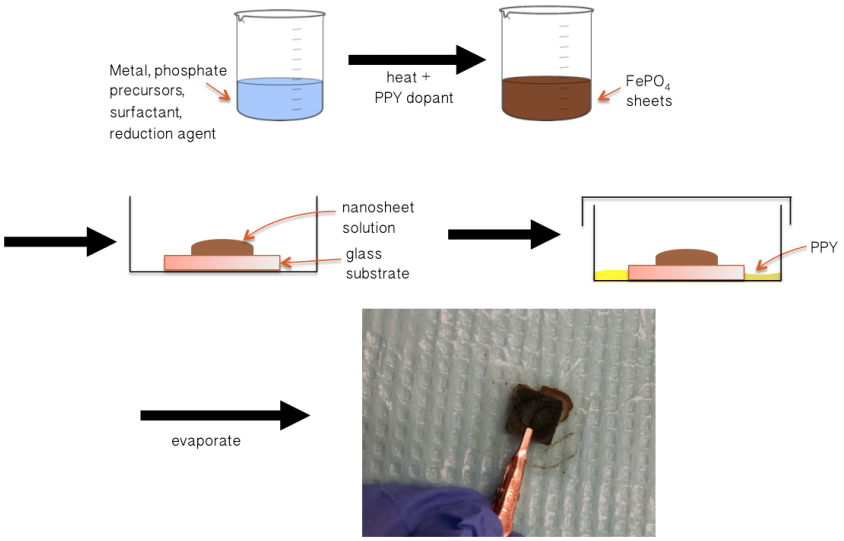

Figure 3.4: Fabrication flow of a $FePO_4$-PPY hybrid supercapacitor/battery. The addition of heat and PPY dopant finish the fabrication of the nanosheet solution. 100μL is dropped onto a glass stage in a petri dish. The stage is surrounded by pyrrole, covered overnight, and allowed to evaporate.

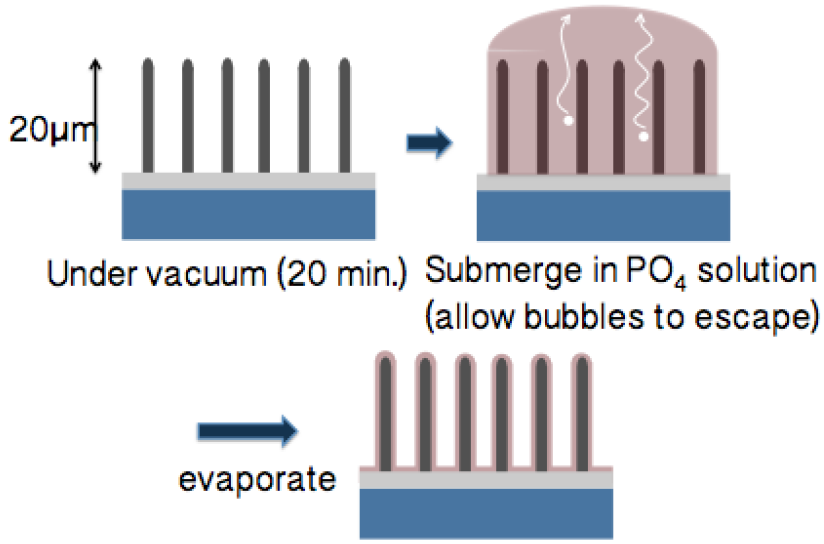

Figure 3.5: Device fabrication process of $FePO_4$-CNTs. After leaving CNTs under vacuum for 20 min, they are submerged into the $FePO_4$ solution. After drying, van der Waals forces keep $FePO_4$ sheets adhered.

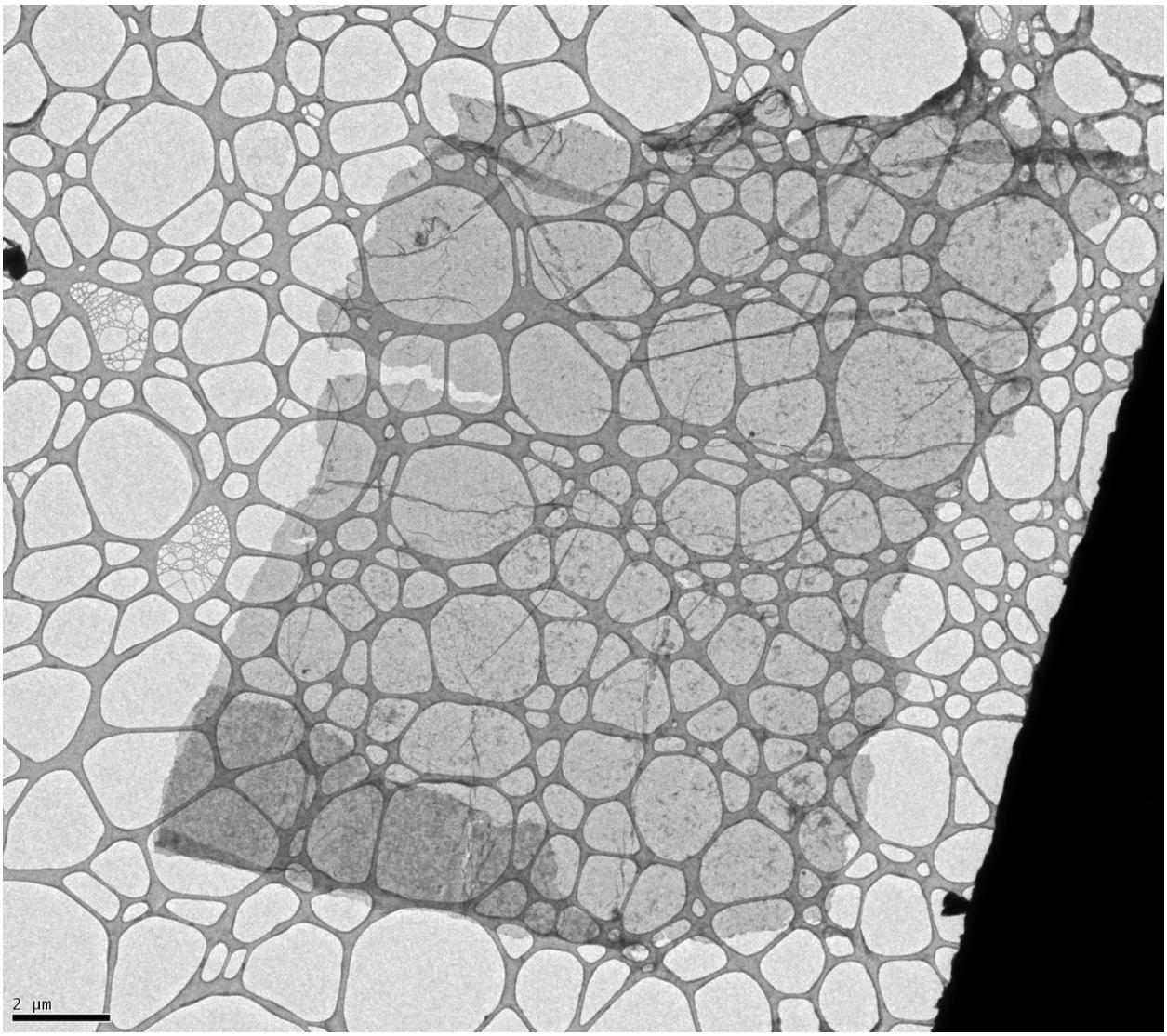

Figure 3.6: TEM imaging of the $FePO_4$ sheets described in Figure 6.2. Film areas are grown up to 50 μm^2.

3.5 Characteristics of solution-processed 2D sheets

The synthesis results of the 2D sheets are shown in the TEM images (Figure 5.10, 3.6). The sheets are large in area, grown up to $50\mu m^2$ (Figure 3.6) and polycrystalline in nature, with grain sizes of about 3–4 nm.

$FePO_4$-based electrodes can be further improved by optimizing morphology of $FePO_4$. By allowing sufficient time for metal ions to coordinate to the surfactant network, we have achieved 2D sheets of $FePO_4$. However, in a surfactant lean mixture, uncoordinated ions preferentially form randomly assembled nanoparticles, reducing before assembling onto the

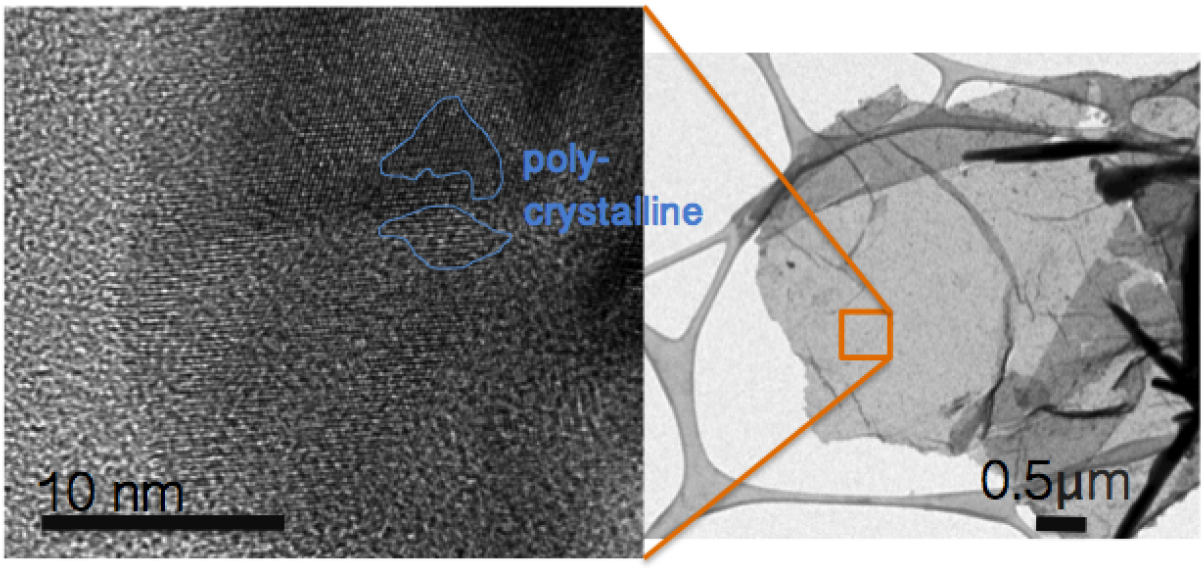

Figure 3.7: TEM imaging of the $FePO_4$ sheets described in Figure 6.2. The structure is polycrystalline, with grain sizes of about 3-4 nm.

organic framework (Figure 3.8). Similarly, excess reducing agent or higher energy state will induce reduction before ions are fully coordinated, resulting in a nanoparticle ink.

The effects of thermal annealing on film quality is also shown in TEM images in Figure 3.9. Thermally annealed samples showed fewer morphological defects and improved crystallinity, indicating higher quality films for diffusive energy storage. However, annealing also results in undesirable layering of nanosheets, reducing surface area available to contact with conductive binders.

3.6 Performance as a Li-ion battery-capacitor hybrid

Due to the ability of $FePO_4$ to intercalate lithium ions, we are able to demonstrate superior capacitive effects by utilizing bulk diffusion of lithium ions into the $FePO_4$ material. (Warren et al., 2015a) $FePO_4$-based cathodes, which have recently come to attention as lithium-ion battery anodes, are limited in performance due to poor conductivity. However, our high surface area, 2D $FePO_4$ sheets can be loaded onto conductive materials easily. When co-polymerized with PPY, $FePO_4$ allows for bulk diffusion of lithium ions into the electrode material, resulting in a substantial improvement (>3x) in capacitance as compared to bare PPY (Figure 3.10). Interestingly, $FePO_4$-PPY doped with SDBS performed better than samples doped with ammonium persulfate. Though a strong oxidizing agent, samples doped with ammonium persulfate experienced more rapid polymerization, resulting in significantly higher resistances (20-25 kΩ vs. 1-10 kΩ) and subsequently poorer electrochemical perfor-

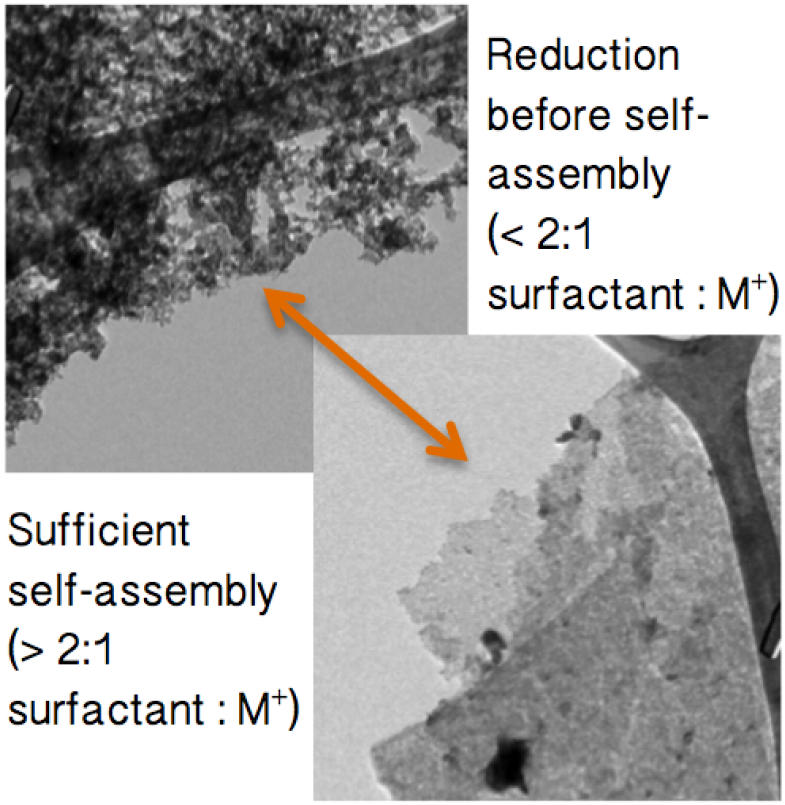

Figure 3.8: Effect of self-assembly on the final morphology of $FePO_4$ by varying surfactant:M^+ concentration. More surfactant promotes self-assembly into lamellar sheets, providing a framework upon which M^+ can coordinate. Without a sufficient framework, M^+ aggregates and reduces into randomly assembled nanoparticles.

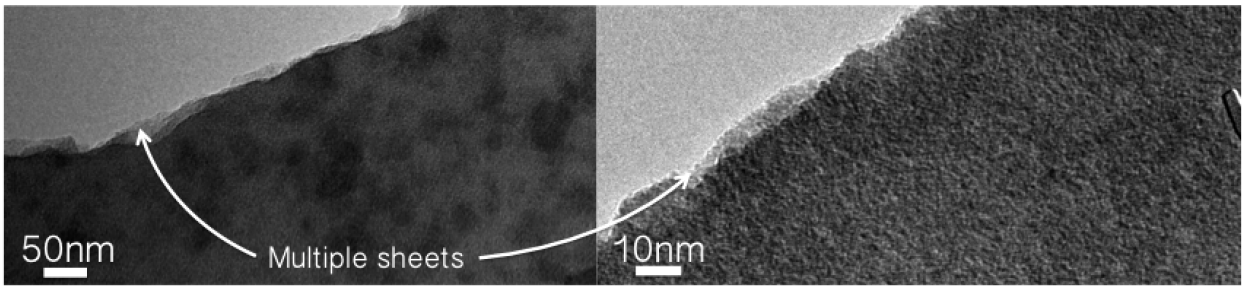

Figure 3.9: Thermally annealed samples show higher quality and improved crystallinity, but undesirable layering of 2D sheets.

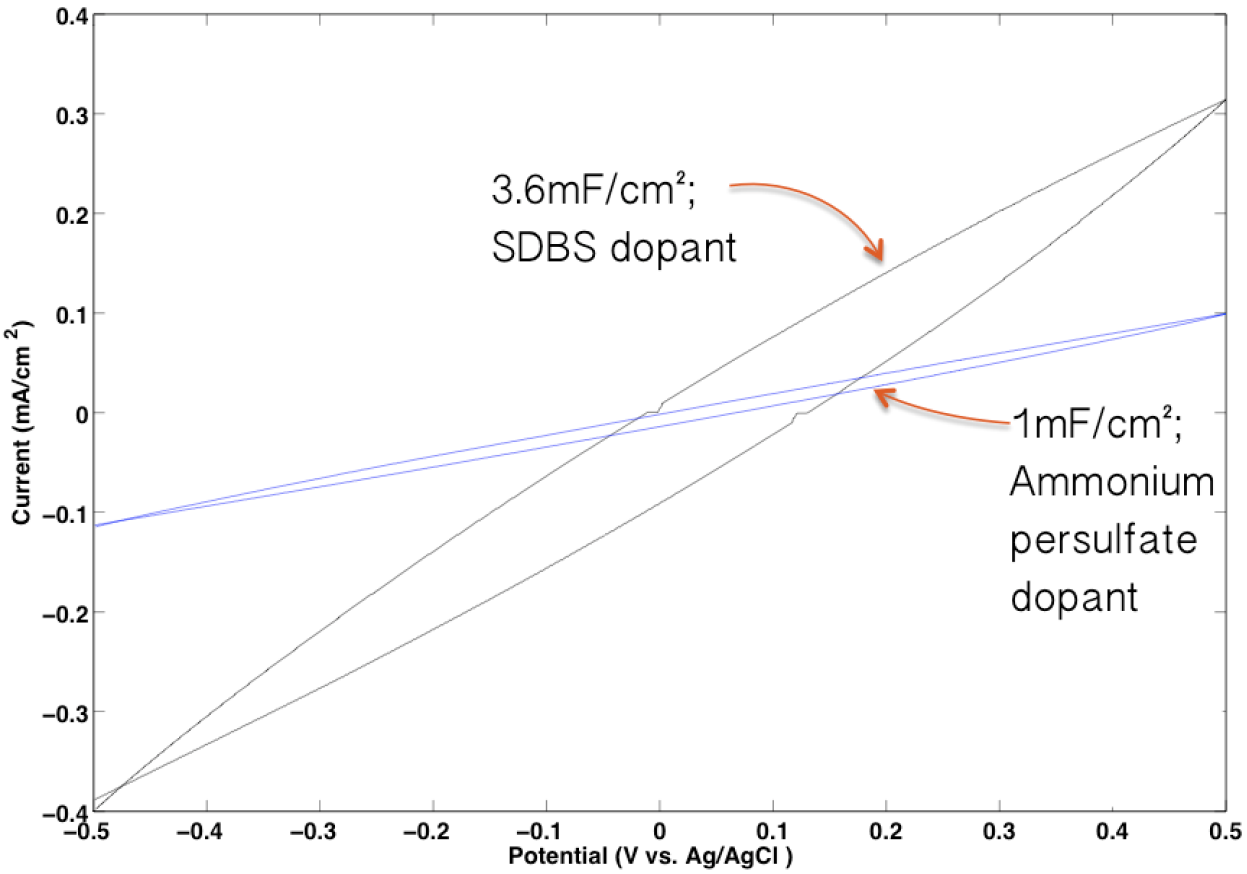

Figure 3.10: Cyclic Voltammetry results of $FePO_4$-PPY supercapacitor/battery hybrid. By using $FePO_4$, we are able to increase the capacitance by 3x.

mance. This is also evident in the cyclic voltammogram (CV) shape. Its thin, almost linear shape is characteristic of highly resistive PPY supercapacitors.

In contrast, the highly porous, highly conductive CNT network shows increased current due to increased surface area. By utilizing a high surface area material, the effects of the electrochemical double charge layer (EDCL), charge adsorbed onto the surface of the electrode, are drastically improved. By utilizing $FePO_4$, pseudocapacitive diffusion of lithium ions is induced, improving the performance >20x over bare CNTs (Figure 3.11).

The cyclic voltammograms shown in this work are also characteristic of supercapacitors. Though improved performance of the $FePO_4$-loaded devices over bare devices implies lithium ion intercalation, lack of sharp peaking indicates that (1) the operating voltage of the devices in this work is outside the lithium intercalation standard potential and (2) capacitance is dominated by EDCL and diffusion, rather than phase change lithium ion intercalation. In contrast, diffusion and EDCL result in broad peaking and the characteristic supercapacitive box shape.

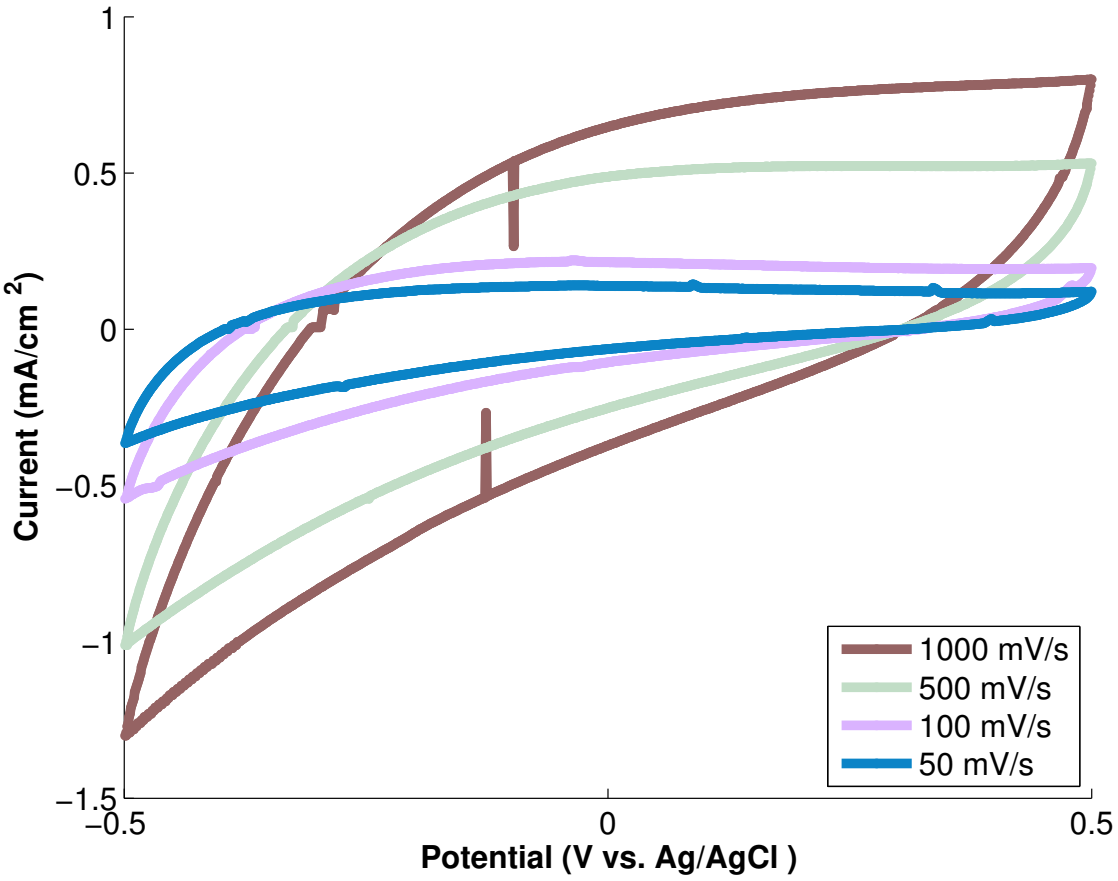

Figure 3.11: Cyclic Voltammetry results of $FePO_4$-CNT supercapacitor/battery hybrid. By using $FePO_4$, we are able to increase the capacitance by 20x.

3.7 Conclusion

Due to the ability of $FePO_4$ to intercalate lithium ions, we are able to demonstrate superior capacitive effects using $FePO_4$-PPY, reaching 3.6 mF/cm^2 (more than 3x the performance of bare PPY films), and 20.8 mF/cm^2 in $FePO_4$-CNTs (more than 20x improvement over bare CNTs). $FePO_4$ cathodes, which have recently come to attention as lithium-ion battery anodes, are limited in performance due to poor conductivity. However, this work presents low temperature, solution-processed synthesis 2D $FePO_4$ sheets, a novel multiple-precursor method for producing 2D materials. These sheets can be loaded onto conductive materials such as PPY and CNTs easily. As such, the development of 2D $FePO_4$ sheets opens up new avenues into highly conductive, high-performance electrochemical electrodes.

Chapter 4

Thiophene-Based Water Splitting

We present thiopene-based devices fabricated via spin-coating and electropolymerization (EP) for usage in solar-powered, photocatalytic hydrogen gas (H_2) harvesting. Two innovative claims are achieved in this work: (1) demonstration of electropolymerized photoelectrochemical (PEC) devices for water splitting, and (2) drastically improved performance of EP-PEC devices over spin-coated PEC hydrogen harvesters, achieving >0.5 V improvement in onset voltage (V_{on}, bias voltage needed to produce photocurrent), with V_{on} of 0 V vs. Ag/AgCl. As such, this work points to new opportunities for material and device fabrication for cheaper and efficient PEC hydrogen harvesting systems.

In this chapter, fundamentals of photoelectrochemical water splitting are introduced. Using polymer-based materials, new approaches to fabrication for water splitting are evaluated.

4.1 Introduction

As a zero-emission liquid fuel for fuel cells, hydrogen gas (H_2) may soon be a competitive replacement for fossil fuels in the US transportation sector.(Ball and Weeda, 2015) In addition, H_2 is already widely used in industry applications: for example, as a reactant for metal finishing, as a precursor to chemical processes such as the HaberBosch process, and even as a high-energy density fuel in aerospace applications. However, current methods of H_2 production rely heavily on fossil fuels. The currently most widely used method, steam reformation ($CH_4 + 2H_2O$ $CO_2 + 4H_2$), not only produces carbon emissions in the H_2 production process itself but also requires maintaining high temperatures (700–1100°C) and is highly energy intensive.(Riis et al., 2006) For this reason, more efficient, less energy-intensive, less carbon-intensive hydrogen production methods are needed.

In contrast, photoelectrochemical (PEC) water splitting devices, working ideally, will passively (without bias voltage) convert sunlight into electron/hole pairs that will oxidize water ($2H_2O + 4h^+$ $4H^+ + O_2$) and reduce resulting H^+ ions ($4e^- + 4H^+$ $2H_2$). As opposed to that of a photovoltaic (PV) cell, a PEC water splitting semiconducting electrode

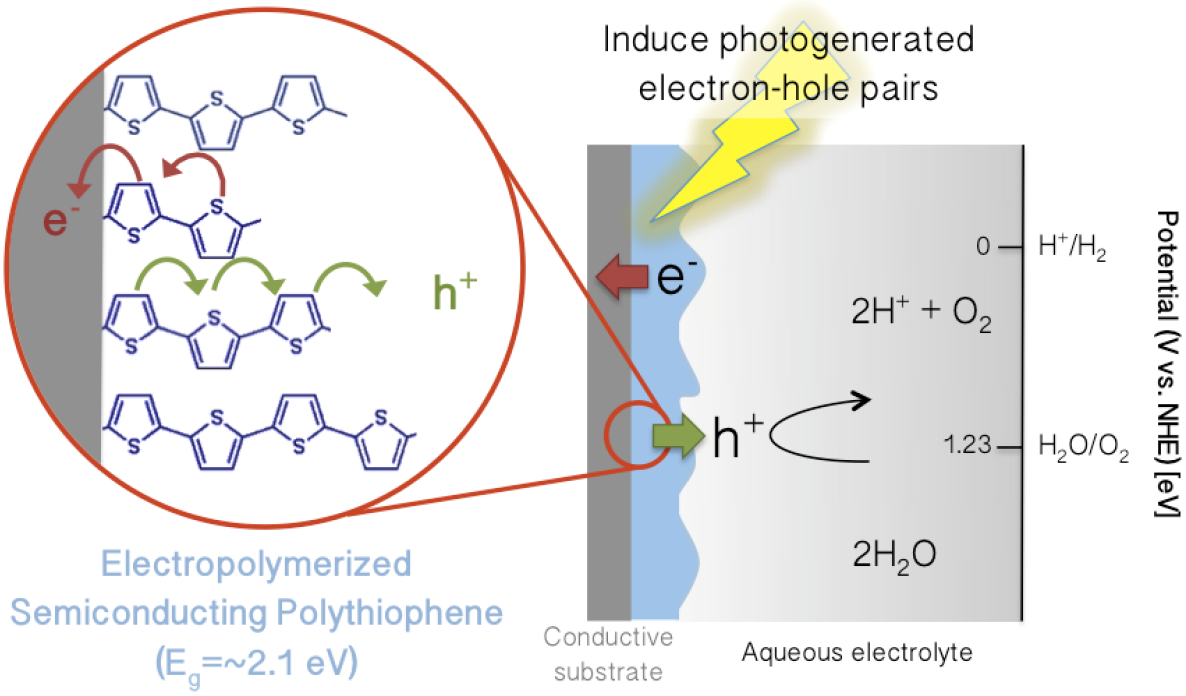

Figure 4.1: Representation of surface reactions at electropolymerized polythiophene (and counter electrode) to allow for hydrogen production. A texturized, electropolymerized, semiconducting polymer with a bandgap of 2.1 eV allows for water oxidation at the surface, and hydrogen reduction at an opposite counter electrode.

uses generated photocurrent to catalyze red/ox reactions in aqueous medium.(Van De Krol, 2012) Since water splitting is easily scalable with the area of semiconducting material used, it is ideal for large-scale hydrogen harvesting. In contrast, achieving large scale hydrolysis using PVs requires multiple cells to be stacked in series, increasing resistivity across the H_2 production system and decreasing conversion efficiency.(Zou et al., 2001)

However, developing materials for efficient conversion of solar energy into fuel has proven difficult to accomplish. Ideal water splitting materials have been difficult achieve; they require a specific band structure and excellent photocatalytic properties. The band structure should exhibit the following characteristics:

1. band gap (E_g) must be small to absorb the solar spectrum effectively
2. E_g must be positioned correctly to allow for the red/ox reactions necessary to split water (conduction band above oxidation potential to donate electrons to the oxidation reaction and valence band below the reduction potential)

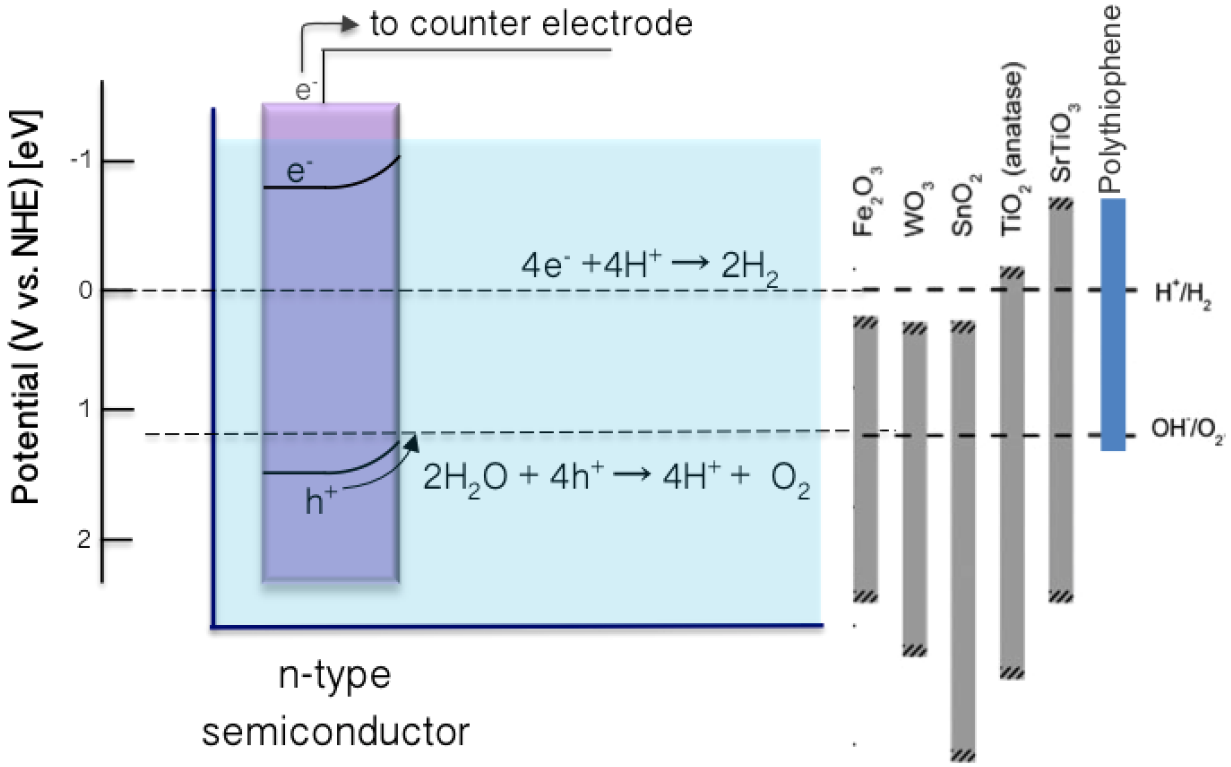

Figure 4.2: Representation of a PEC water splitting system: if the conduction band and valence band are above and below the reduction and oxidation potentials, respectively, then charge separation at the surface will allow for water splitting. In an n-type material (shown here), band bending will allow holes to oxidize water, and electrons will reduce resulting hydrogen ions at the counter electrode. By doing so, H_2 gas is produced, which can then take part in the hydrogen economy. For example, fuel cell vehicles will emit H_2O as a byproduct, which can then be reused as the the aqueous electrolyte in the PEC system.

3. materials must exhibit high charge separation efficiency in contact with an aqueous electrolyte

Moreover, materials often exhibit poor V_{on} (require large bias voltages to observe photocurrent) due to poor conductivity, recombination, and undesirable band structure. (Zhao et al., 2015)

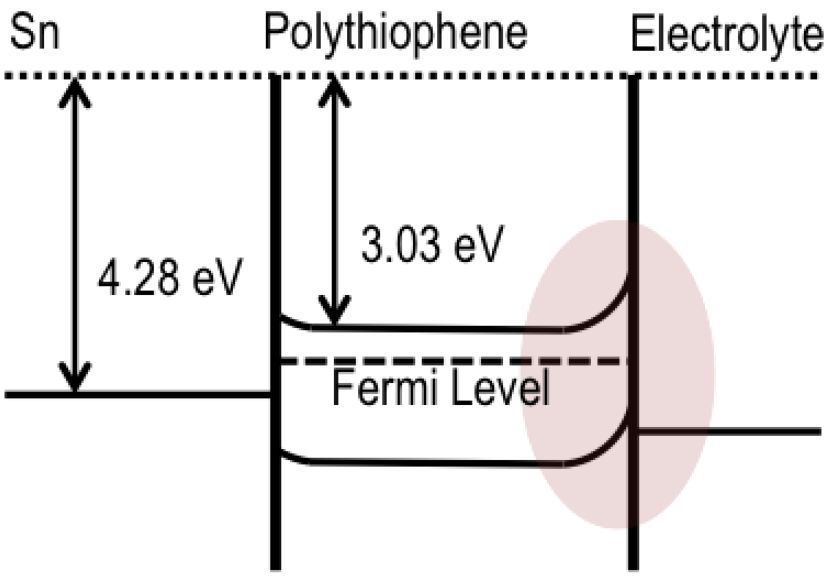

Figure 4.3: Proposed bandgap configuration, allowing electrons to flow freely into the electrical connection.

4.2 Principles of Photoelectrochemical Water Splitting

As in photovoltaic devices, the space-charge layer, a layer of built-in electric field formed in PEC semiconducting electrodes, is responsible for the efficient separation of electrons and holes, and thus prevents recombination. This electric field is formed at the surface of the electrode-electrolyte interface due to the transfer of charge across the interface of the semiconductor.(Van De Krol, 2012)

The origin of this space-charge layer arises from the equilibriation of the semiconductor's Fermi level and the oxidation-reduction potential of the liquid junction (aqueous electrolyte). As charge moves across the semiconductor interface in an effort to reach equilibrium, a depletion layer—the space-charge layer—forms at the surface. The resulting band bending at the interface can occur in four different forms.(Jiang et al., 2017; Zhang and Yates Jr, 2012)

1. Metal-semiconductor-induced bending, wherein, depending on the work function of the metal and the Fermi level of the semiconductor, either Ohmic or Shottky contact can be attained. This band-bending mechanism is especially useful because of its relative tunability, allowing for enhanced charge separation.

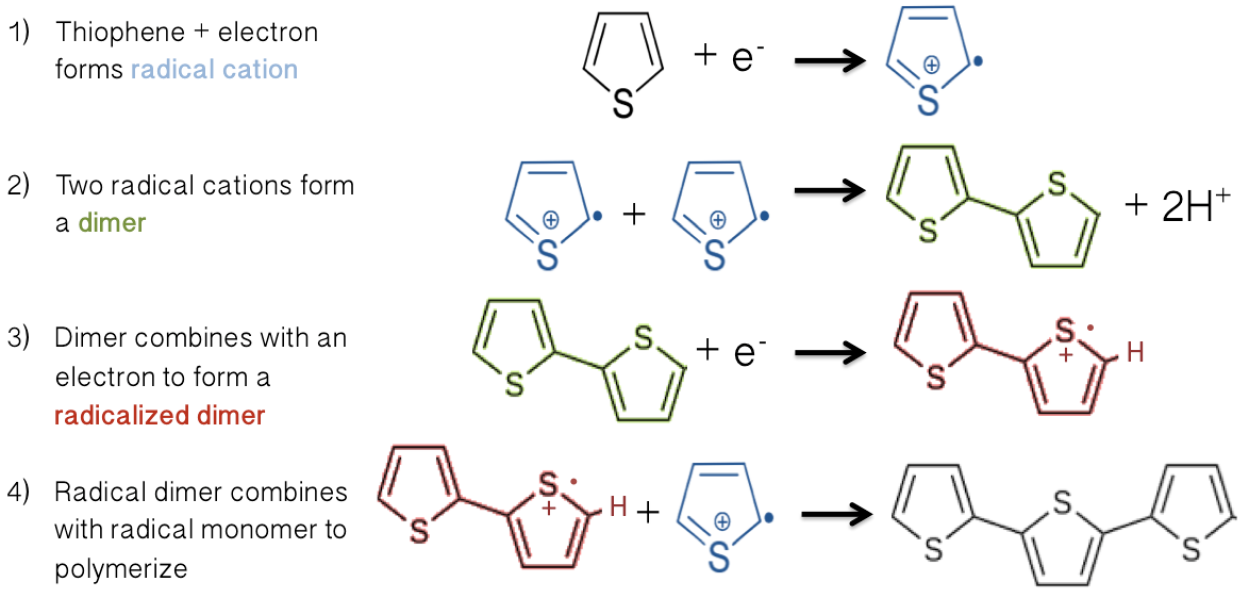

Figure 4.4: Under electropolymerization, a constant voltage applied relative to an Ag/AgCl reference electrode and platinum counter electrode, is expected to polymerize thiophene under the following steps: (1) thiophene combines with an electron to form its radical cation, (2) the radical cation combines with another radical cation and forms a dimer + 2 hydrogen ions, (3) a dimer combines with an electron to form its radical form, and (4) the radical dimer combines with a radical monomer to polymerize.

2. Surface state-induced bending, wherein surface states cause local band bending, even in intrinsic semiconductors, due to transfer of charge carriers from the bulk to the surface state until the surface state and bulk are in equilibrium.

3. Absorption-induced bending, wherein equilibriation with adsorbed donor or acceptor molecules causes surface bending. In addition to surface bending, a steep potential drop forms across the Helmholtz layer, as discussed in Chapter 2.3.2.

4. Applied bias-induced bending, wherein an applied bias causes localized bending, distributed across the space-charge region and Helmholtz layer. For materials that are unable to achieve passive water splitting, applied biases are utilized to induce more efficient charge separation.

4.3 Approaches to employing semiconducting polymers

Recent approaches to increasing photocurrent and decreasing onset voltage attempt to increase conversion efficiency, absorbing more of the solar spectrum by either using dye-

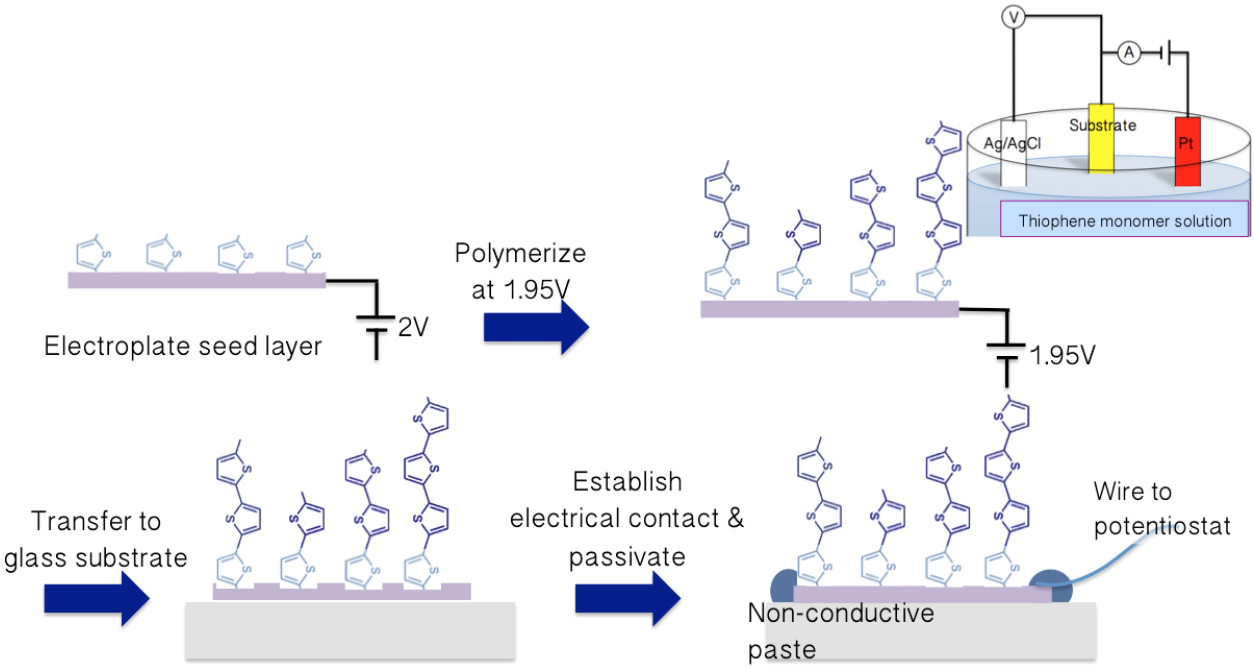

Figure 4.5: Fabrication of an electropolymerized thiophene-based electrode. First, a seed layer is deposited at 2V and allowed to polymerize at 1.95V for 60 s on a conductive substrate. After the material is electropolymerized, the entire substrate is glued onto a glass substrate and electrically insulated. Finally, electrical contact is established using conductive tape and insulated wiring. The sample is passivated using epoxy to isolate the active material and to ensure that only the active material is in contact with the aqueous solution.

sensitizers or using catalysts to lower overpotential needed to split water.(Xu et al., 2017) Some organic dye-sensitizers enhance performance by increasing light absorption; the bulk material provides a stable charge-transport base for the moisture-sensitive organic material.(Li et al., 2015; O'regan and Grätzel, 1991) The addition of hydrogen evolution or oxygen evolution catalysts to water splitting materials is also crucial to increasing photocurrent and decreasing onset voltage. Indeed, some semiconducting materials show little observable photocurrent without a catalyst. Only recently have devices with organic material as the bulk material (as opposed to a dye-sensitized one) been realized as effective water splitting photoelectrodes.(Haro et al., 2015)

Conductive polymers have been found to exhibit characteristics favorable for many applications, such as gas sensors, LEDs, FETs, or photovoltaics.(Gusain et al., 2017; Lee et al., 2013) Moreover, due to optical properties in organic electronics, efforts toward cheaper, more efficient, and more robust pathways to polymerization, were developed, such as ZieglerNatta, electrodeposition, Negishi, and Suzuki.(Morin et al., 2016) Of these, electrodeposition, in which monomer-rich electrolyte solutions undergo polymerization under electric current at

the substrate-electrolyte interface, has been shown to achieve rapid, robust, conformal deposition over a highly texturized, highly porous substrates.(Jiang et al., 2013; Gurrappa and Binder, 2008)

Though cheaper, thiophene-based materials, such as poly-3hexylthiophene (P3HT), have been used widely in photovoltaic applications(Mihailetchi et al., 2006; Kim et al., 2006) and in organic electronic or optoelectronic devices,(Lee et al., 2010) P3HT has proven difficult to use as a water splitting material because of its susceptibility to moisture. Previous work utilizing thiophene-based polymers attempt to stabilize the material with oxide coatings such as titanium dioxide. However, this presents a trade-off between stability and performance: thicker TiO_2 passivation layers allow for more stable hydrogen generation ($>$ 3h), but also limit solar absorption and decrease conductivity, lowering photocurrent. Despite recent advances in polymerization techniques, existing work on bulk organic materials for water splitting focus on various methods of spin-coating.(Li et al., 2015) However, these methods significantly limit potential of sophisticated fabrication of devices. In particular, texturization of substrates has been shown to increase active area, solar absorption, and improve charge separation.(Van De Krol, 2012) By limiting device architectures to planar substrates, existing methods such as spin-coating reduce efficacy of organic substrates in relation to well-known metal oxide semiconductors, of which studies in texturization are numerous.(Shao et al., 2018; Park et al., 2017)

This work presents proof of concept demonstrations of electroplated polymer materials for photocatalytic water splitting.(Roncali, 1992) By using polythiophene (PT), we are able to produce an n-type, thiophene-based PEC device. By electropolymerizing PT, we dope it in situ, allowing for hole and electron transport into the electrolyte and to the counter electrode, respectively (Figure 6.1).

4.3.1 Electrode Design

Figure 4.2 shows a conceptual realization of the water splitting system. When the system is illuminated in an n-type semiconductor, charge separation occurs, band bending allows holes to enter into the electrolyte, and electrons flow into the counter electrode. Furthermore, since electron affinity of polythiophene allows its conduction and valence bands to straddle the red/ox potentials of the water splitting system, PT is a good candidate material for water splitting. The detailed band diagram of the tin electrical contact, PT, and electrolyte are shown in Figure 5.2. Thus, electroplated PT, with favorable band structure for both solar absorption and photocatalysis is able to achieve V_{on}=0 V vs. Ag/AgCl, even without the use of a surface oxygen- or hydrogen- evolving catalyst.

For this paper, we utilize spin-coated P3HT devices as reference devices for comparison purposes. Spin-coated P3HT was chosen for its popularity in the literature and its comparable band structure when compared to PT. While both are thiophene-based, they also exhibit comparable bandgaps (in the visible range).

4.4 Device Fabrication

A two-step electropolymerization (shown in Figure 4.4) process was developed to (1) deposit a seed layer and (2) subsequently polymerize the seed layer as shown in Figure 4.5. Alloyed UNS S30100/S30200/S30400 full hardened stainless steel shim (0.002 in. ASTM-A-666, TBI Inc.) is used as the substrate for electropolymerized PT. 0.1 M tetrabutylammonium hexafluorophosphate and 0.1 M thiophene monomer in acetonitrile comprise the electroplating solution. Platinum wire acts as the counter electrode and Ag/AgCl as the reference electrode. Multiple concentrations of thiophene monomer were used to investigate the effects of concentration on the polymerization process. It was found that higher concentrations on the order of 0.1 M and above yielded more uniform film thicknesses, with polymerization able to reach the center of a planar substrate. Concentrations on the order of 0.01 M, in contrast, either yielded no significant electrodeposition. A two-step electropolymerization process was developed:

1. 10-second seed layer deposition with Vbias = 2V vs. Ag/Ag+; and
2. a 60-second film deposition with Vbias = 1.95V vs. Ag/Ag+. The conductive electrode is passivated onto a glass substrate using epoxy.

The final electropolymerized device is shown in Figure 4.6c.

The proposed electropolymerization mechanism is shown in Figure 4.4. First, the thiophene monomer combines with an electron, becoming a radical cation. The combination of two radical cations form a single dimer of polythiophene, with a by-product of two protons. Since dimers are more easily oxidized than monomers, the dimer then forms its radical form. When a radicalized dimer combines with a radical cation, polymerization begins to occur. It is important to also note that since electron transport occurs much more quickly than monomer diffusion in the electropolymerization electrolyte, there is an assumed high concentration of radicals around the surface of the electrode surface at all times.

A reference P3HT electrode is fabricated by spin coating P3HT dissolved in 1,2 dichlorobenzene or chloroform at varying concentrations from 20–30 mg/mL overnight while heated to 70°C. Spin rate was also varied from 400–800 RPM. Quartz substrates were used to isolate photocatalytic properties. The electrode is then thermally annealed at 200°C for 30 min. A top-down view of the spin-coated quartz wafer is shown in Figure 4.6.

4.4.1 Substrate Limitations

To prepare the final device, the electrode is then affixed onto a glass microscope slide and electrical contact is established using copper tape and insulated tin wire. To electrochemically isolate the P3HT from the copper tape and wire, epoxy was used to passivate the P3HT. The final P3HT device is shown in Figure 5c. Electrical connection was maintained

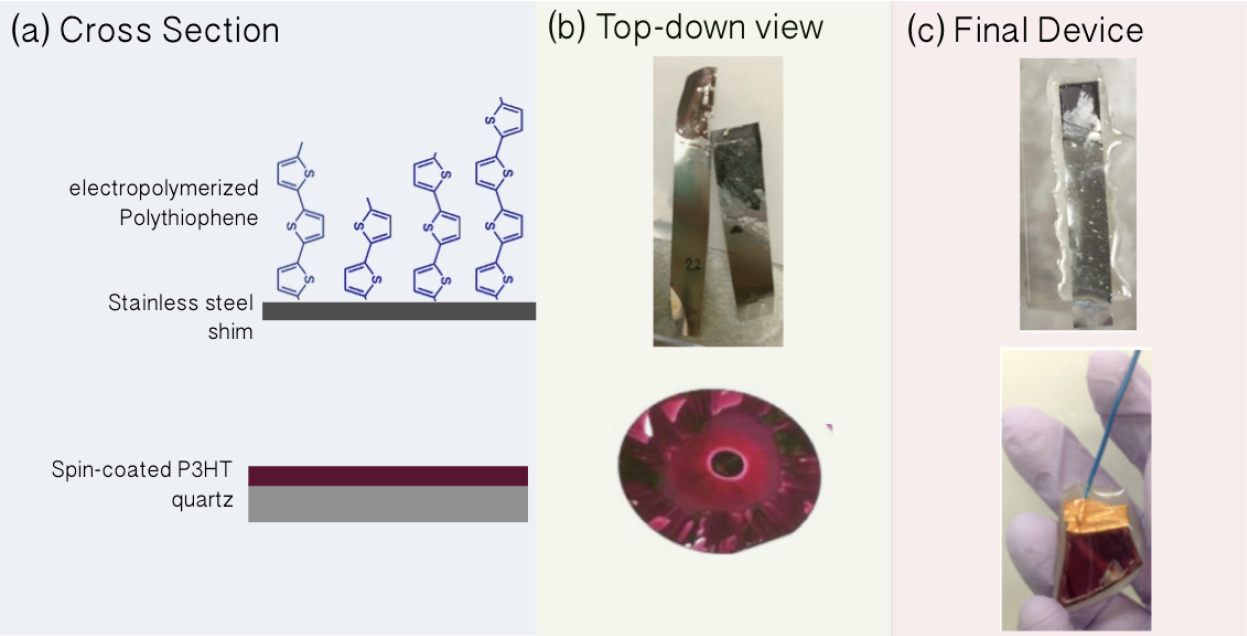

Figure 4.6: (a) Cross sectional view of both electropolymerized PT and spin-coated P3HT on quartz. (b) top-down view. (c) Final device, with both electrodes fully passivated using epoxy on a glass substrate.

to the P3HT (front side of the device), rather than its substrate. While quartz was chosen in order to isolate the performance of the polymer material (both electrically and electrochemically), electrodeposition necessitates a conductive substrate for polymerization to take place on the interface of the electrolyte and electrode. That is, electropolymerization on a quartz substrate would be impossible. Thus, stainless steel was chosen for its conductivity and relative electrochemical isolation (does not show water splitting, as compared to substrates such as silicon or copper oxides).

4.5 Electrode Testing

The electrode is tested using a three-electrode setup. Electrodes were tested electrochemically using a Ref 600 Gamry Potentiostat. Linear Sweep Voltammetry was conducted in dark and lit conditions under a Xenon lamp (Asahi MAX-303). The electrodes are further isolated from light using an isolation chamber made of Thorlabs Blackout Hardboard. The samples were tested vs. Ag/AgCl from -1 V to 0 V or 0 V to 1 V (depending on majority carrier in the electrode) with a platinum counter electrode in 0.5 M H_2SO_4 electrolyte solution at a scan rate of 50 mV/s.

4.6 Characterization

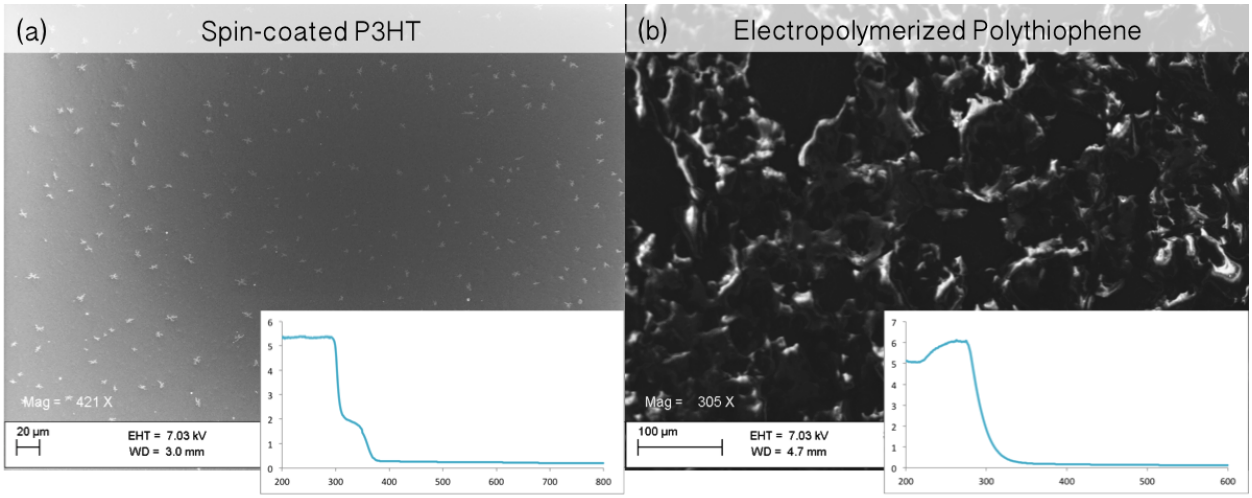

Figure 4.7: Fabrication results: SEM images of (a) spin-coated film, with relatively conformal and uniform coverage; (b) electropolymerized polythiophene film, showing increased texturization of the film; (inset) UV/Vis absorption spectra for spin-coated P3HT and electropolymerized polythiophene, respectively.

Scanning electron microscopy (SEM) images of spin-coated P3HT show uniform thickness and conformal coating of the substrate up to hundreds of microns in area (Figure 6.3). A top-down view of the spin-coated P3HT is shown in Figure 4.6b. In contrast, electropolymerized PT devices show relatively uneven coverage due to non-conformal seed layer deposition and polymerization, as shown in Figure 4.6b. SEM images of electropolymerized PT also show significant surface texturization, consistent with uneven polymerization across the surface of the stainless steel, as well as pinholes, as can be seen in the top left corner of Figure 6.3. Furthermore, UV/Vis spectra (Figure 6.3 inset) demonstrate that the bandgaps of the PT and P3HT are indeed comparable, 3.7 eV and 3.3 eV, respectively. Both materials exhibit high absorption in UV, with optical absorption edge in the UV-Vis/Vis range. While both materials exhibit a sharp decrease in absorption around 300 nm, P3HT exhibits extended absorbance, nearing the visible range. To confirm electropolymerization, X-Ray Photoelectron Spectroscopy (XPS) was conducted for devices having undergone electropolymerization with a low-concentration (0.01 M) thiophene monomer solution and a high concentration (0.1 M) solution. As shown in Figures 6.4a and 6.4b and discussed in Section 6.2, low concentration solutions failed to yield any significant electroplating of PT, as seen by the lack of noticeable sulfur. In contrast, the XPS for plated thiophene (Figure 6.4c) shows significant sulfur peaking with binding energy 162–172 eV (Figure 6.4d). This further proves that the presence of PT on the stainless steel shim is not simply residual plating solution but rather polymerized PT onto the substrate.

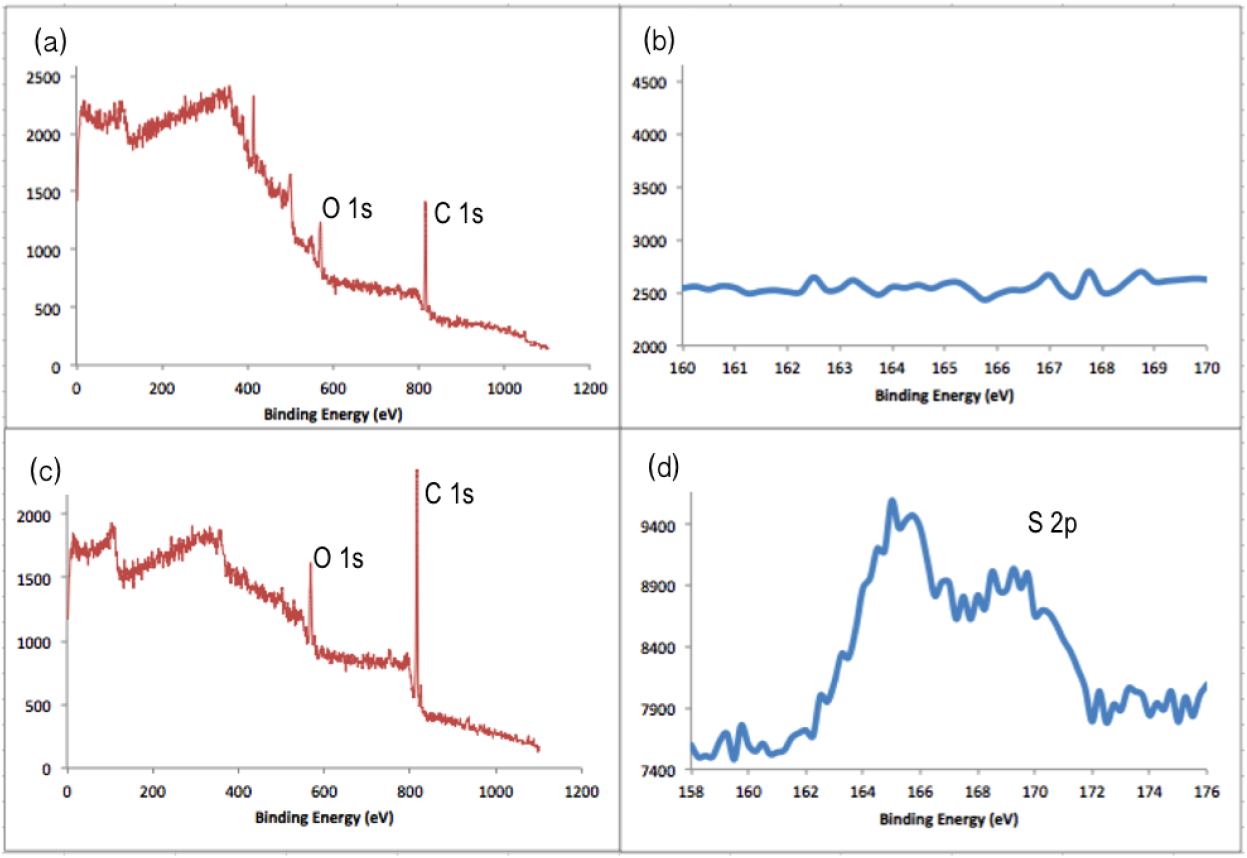

Figure 4.8: Characterization by XPS shows (a) full scan of stainless steel shim in a 0.01 M plating solution, (b) scan of sulfur peaks, showing no discernible sulfur, (c) full scan of stainless steel in a 0.1 M plating solution, (d) scan of sulfur. This proves that thiophene detected on the surface was not just a result of being submerged in the solution but rather a result of electrodeposition.

4.7 Photocurrent Testing

Figure 6.8 shows photocurrent measurements of the spin-coated P3HT device and the electropolymerized PT devices. While significant photocurrent is exhibited in the linear sweep voltammetry of both devices, spin-coated devices showed poor onset voltage (-0.5 vs. Ag/AgCl). The electropolymerized device shows $V_{on} < 0$ V vs. Ag/AgCl.

The use of electropolymerization allows for increased texturization of the electrode device by taking advantage of nucleation during the seed layer step. Under SEM, we observe a highly texturized surface on top of the flat conductive substrate. As nucleation tends to occur at point defects on the substrate, the surface of electropolymerized PT exhibits increased surface area. However, as photocurrent is not uniformly larger in the electropolymerized device as compared to that of the spin-coated device, it is unlikely that larger surface area accounts

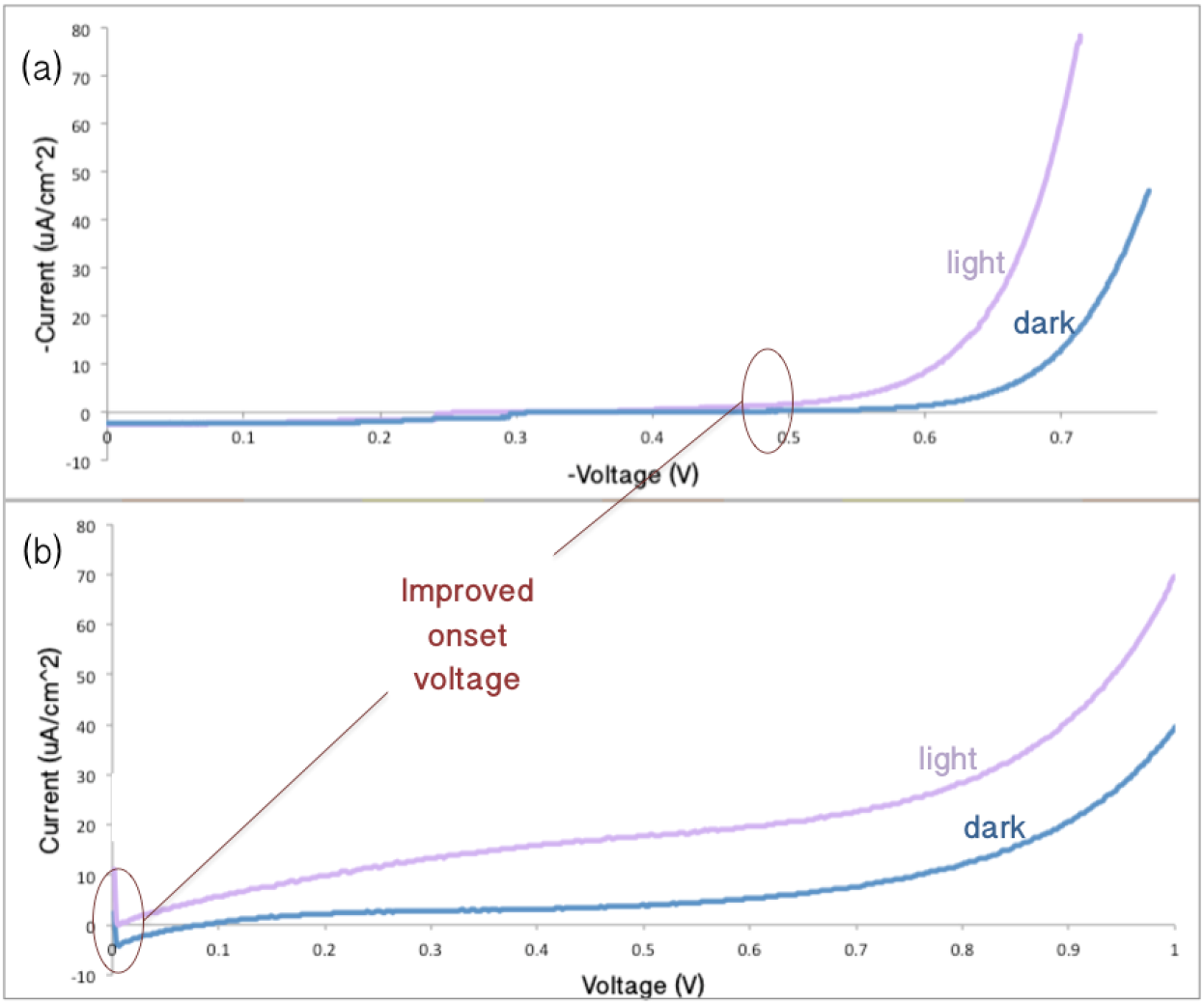

Figure 4.9: Photocurrent results for (a) spin-coated, p-type P3HT and (b) electropolymerized, n-type polythiophene, showing significantly improved onset voltage when compared to spin-coated P3HT.

for the entirety of the improved water splitting performance. Moreover, since P3HT shows elevated absorption as compared to that of electropolymerized PT, it is further unlikely that band structure accounts for improved water splitting of the electropolymerized sample.

We posit that superior onset voltage results from improved alignment relative to substrate. Previous literature has shown that the direction of electron flow is dependent on hydrophobicity of elements in the polymer materials, as well as the hydrophobicity of the substrate.(Mihailetchi et al., 2006; Kim et al., 2006) For example, on a hydrophobic surface, hydrophobic hexyl groups in P3HT are expected to preferentially align to the surface of the substrate, causing electron flow parallel to the surface of the substrate. Similarly, with

P3HT on a hydrophilic surface, electron flow is expected to be perpendicular to the substrate surface. Thus, a hydrophilic quartz substrate was chosen for the P3HT: by decreasing the traveling distance of the charge carriers, we expect superior charge separation and water splitting performance.

Since orientation of the polymer relative to the substrate directly affects direction of electron flow, we are able to preclude alignment of the hydrophobic hexyl groups by electropolymerizing the thiophene monomer. P3HT, even with thermal annealing and substrate choice of quartz, is more difficult to align than PT because grain boundaries around areas of regioregularity in P3HT disrupt electron flow to the substrate (and thus to the counter electrode). That is, P3HT, with hexyl groups, is more likely to be misaligned and hinder electron transport, even when deposited onto a hydrophilic surface to minimize carrier distance. With our electropolymerization method, by precluding alignment, we expect to decrease barriers to carrier flow, allowing for more efficient conversion of solar energy into H_2–as shown by the excellent onset voltage (0 V vs. Ag/AgCl) for the electropolymerized device as compared to the poor onset voltage of the spin-coated device.

Moreover, electroplating has the potential to open pathways toward PT deposition onto porous conductive structures such as activated carbon structures, carbon nanotube forests, and nanowire arrays. By using a highly porous material, one can increase light absorption by using the geometry of the material to harvest reflected light. Porous materials are also able to increase active material while maintaining small minority carrier distances, preserving increased charge separation efficiency.

4.8 Conclusions

This work presents first demonstrations of electropolymerized organic semiconducting materials (PT) for PEC water splitting. As such, these devices show drastic improvement in V_{on} over conventional spin-coated P3HT devices due to superior charge separation and texturization using the electropolymerization method. As compared to spin-coated P3HT (with V_{on} = -5.5 V vs. Ag/AgCl), EP-PEC devices achieve V_{on} = 0 V vs. Ag/AgCl. As such, electroplating has the potential to open pathways toward more robust deposition of organic semiconductor PEC materials onto porous conductive substrates.

Chapter 5

Titanium dioxide photocatalysis

Hybrid Zinc Oxide (ZnO)/Titanium Dioxide (TiO_2) nanowire arrays for potential applications in solar-powered hydrogen gas (H_2) harvesters are presented. High aspect ratio TiO_2 nanowire arrays are based on a hybrid fabrication process using hydrothermal ZnO nanowires as a core template and atomic layer deposition (ALD) of TiO_2 as the active material. High aspect ratio hybrid nanowires over 10 μm tall exhibited improved stability over bare ZnO nanowires. By utilizing ultra-precise, highly conformal ALD, precise and controllable films of TiO_2 were shown to accomplish excellent onset voltage due to increased surface area and improved charge separation. As such, these structures can potentially open up a new class of micro/nano fabrication for efficient photocatalytic gas harvesting systems.

In this chapter, metal oxide semiconductors for photocatalytic water splitting will be introduced. The theory and principles of (1) band bending for water splitting; (2) material considerations; and (3) geometrical considerations will be discussed, and a demonstration of these principles using TiO_2-coated ZnO nanowires will be presented.

5.1 Introduction

Hydrogen as a fuel source has gained attention as a clean-burning liquid fuel alternative to fossil fuels. It has been estimated that 37.7 Mt/yr of hydrogen alone would be enough to replace the coal currently utilized in the United States.(Yildiz et al., 2005) However, current methods of hydrogen (H_2) production are limited. Most H_2 in the United States is produced by steam reformation: burning methane with high-temperature steam to create H_2 and carbon dioxide as a byproduct ($CH_4 + H_2O$ (+ heat) $\rightarrow CO_2 + 3H_2$). Other methods include the electrolysis by solar cells, renewable liquid reformation, and fermentation, which are plagued by low solar-energy-to-water efficiency, low yields, and poor selectivity.(DOE)

In contrast, photoelectrochemical (PEC) water splitting has the potential to passively convert solar energy into H_2 more effectively than electrolysis by using photovoltaics (PV). PEC water splitting is capable of higher yield and selectivity, without carbon emissions as

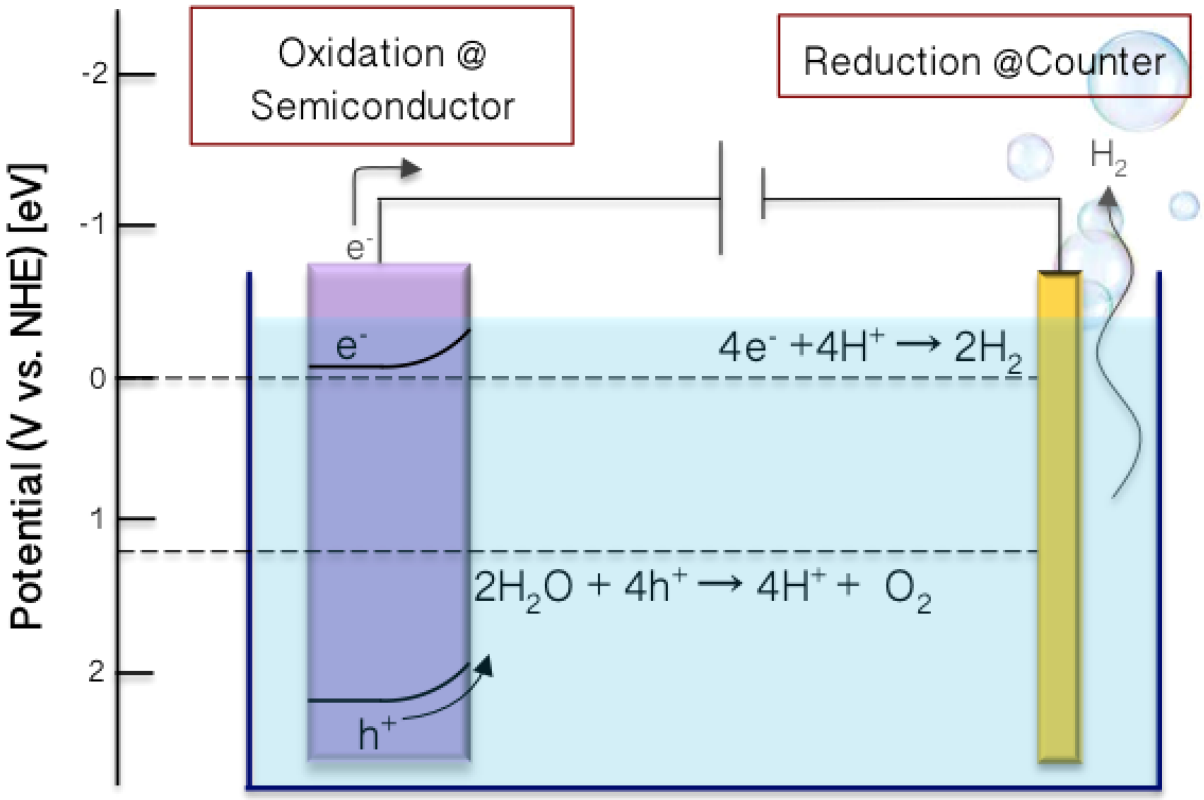

Figure 5.1: Water splitting cell: incident light creates photo-generated electron-hole pairs. Given an appropriate band structure (straddling water reduction/oxidation potentials) holes and electrons will oxidize water at the photoanode and reduce resulting H^+ ions at the cathode, respectively. These reactions result in oxygen and hydrogen gas production.

a byproduct. Photogenerated electron/hole pairs are utilized in the PEC process to oxidize water ($2H_2O + 4h^+ \rightarrow 4H^+ + O_2$) and reduce resulting H^+ ions ($4e^- + 4H^+ \rightarrow 2H_2$) at the semi-conductor/electrolyte interface while submerged in an aqueous medium as shown in Figure 6.1.(Zou et al., 2001) In contrast to PV electrolysis, this process is theoretically more efficient since the PEC process experiences fewer losses because it is no longer necessary to stack multiple PV cells to attain the required bias voltage. Furthermore, since water splitting is easily scalable with the area of the semiconducting material, it is ideal for large-scale, high yield hydrogen harvesting. The selectivity of the PEC process is tunable with the band structure: E_g must be positioned correctly to allow for the red/ox reactions necessary to split water: conduction band should be above the reduction potential, and valence band should be below the oxidation potential.

5.2 Background

After Fujishima and Honda's first report of water splitting using an n-type TiO_2 electrode,(Fujishima and Honda, 1972) numerous studies have been conducted to achieve stable and efficient PEC systems using materials responsive to solar spectrum. (Khaselev and Turner, 1998; Bak et al., 2002; Mor and Varguese, 2005) However, the state-of-art devices show three major drawbacks: (1) low conversion efficiency due to recombination and poor quality of materials; (2) high onset voltages (requiring a voltage bias to begin the red/ox of water); and (3) poor material stability in the photocatalytic process.(Ni et al., 2007) Thus, many subsequent research projects have focused on either stabilization layers or texturization of the surface to increase conversion efficiencies in a highly oxidizing (aqueous) environment.(Paracchino et al., 2011; Liu et al., 2013a)

5.3 Band Bending in Metal Oxide Photoanodes

The photocatalytic H_2 gas harvesting system consists of a photoelectrode and a counter electrode submerged in an aqueous electrolyte solution. In the photoelectrode, light absorption generates electron-hole pairs to promote electrons from the valence band to the conduction band. A Schottky barrier is formed at the photoelectrode-electrolyte interface. With properly chosen electrolyte solution (potential) and photoelectrode (Fermi level), minority carriers move into the electrolyte and begin reduction/oxidation (depending on whether the photoelectrode is p- or n-type) of water. Majority carriers oxidize/reduce water at the counter electrode-electrolyte interface. Figure 5.2 shows the energy band diagram for this specific photocatalytic system using an n-type, TiO_2 photoanode.

Efficient, low-cost, and scalable PEC water splitting systems have limited photoelectrode selection. Photo electrodes must have a suitable band structure for absorbing as much solar energy as possible. The minimum band gap for photoelectrode materials is determined by the required Gibbs free energy (1.23 eV) for water splitting plus thermodynamic loses (0.3 eV-0.4 eV) and overpotentials for driving chemical reactions (0.4 eV-0.6 eV). Consequently, the energy band gap should be higher than 1.9 eV for ensuring sufficiently fast energetics. However, photoelectrode band gaps must also encompass the water reduction (0 V) and oxidation (-1.23 V) potentials for the redox half-reactions. Hence the ideal value of the energy band gap of the photo absorber material should be placed between 1.9 eV and 3.2 eV while encompassing redox half-reaction potentials.This section addresses the principles of operation of a photoanode water splitting material, focusing on metal oxide semiconductors, adapted from Van De Krol (2012).

5.3.1 Formation of the Space Charge Layer

Upon illumination, photogenerated electron-hole pairs take part in charge transfer across the semiconductor-electrolyte interface, forming what is known as a space charge region.

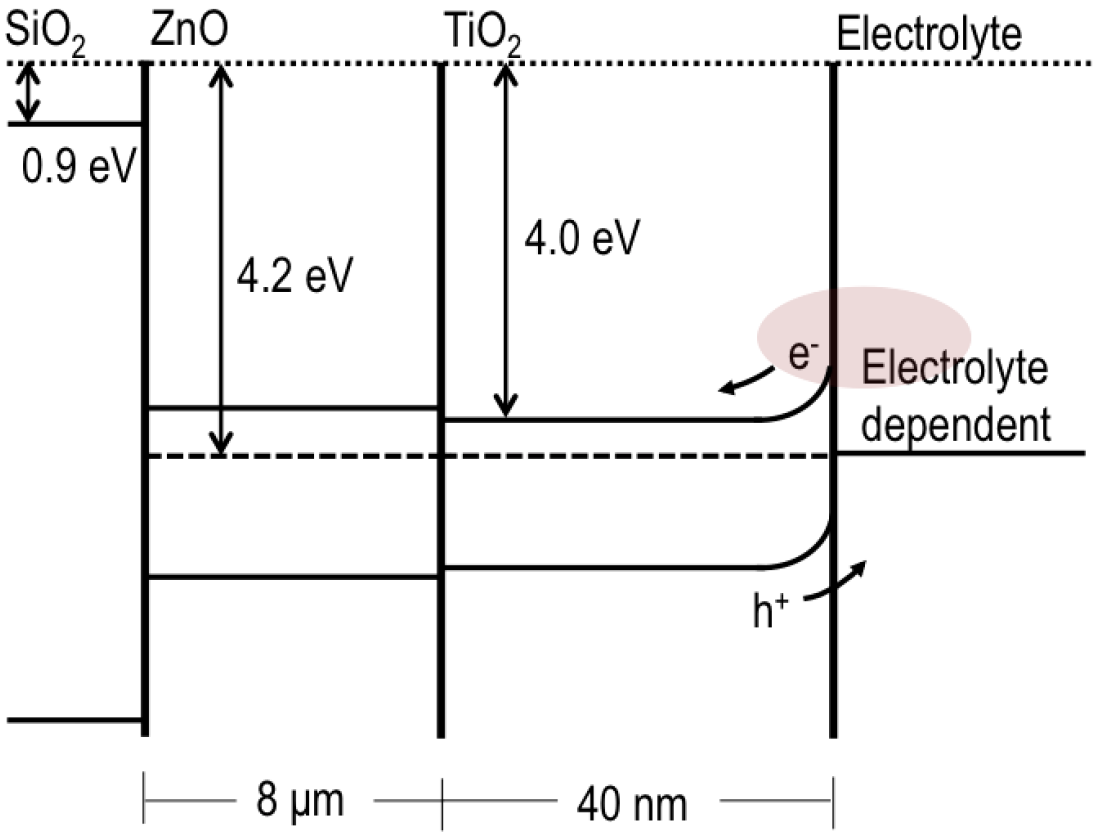

Figure 5.2: Proposed band gap structure of TiO_2@ZnO: high aspect ratio TiO_2 experiences charge separation at the electrolyte-TiO_2 interface, moving holes into the electrolyte and electrons into the single-crystalline ZnO nanowire.

This region forms a built-in electric field responsible for separation of electons and holes, preventing recombination and allowing for efficient photocatalysis.

Semiconductors brought into contact with a material (metal or semiconductor) with a differing Fermi level, will equilibriate by transferring charges across the junction. In a p-n junction, for example, majority carriers will flow across the boundary, causing a depletion layer (lack of mobile charges) on either side of the p-n interface. Similarly, in a metal oxide semiconductor, water molecules dissociate and adsorb onto the surface of the metal oxide, resulting in -OH surface termination groups. These -OH groups comprise electronic surface states which are occupied by photogenerated electrons. Charge transfer takes place between the bulk and modified surface until the system has equilibriated, and the potential barrier is too large for bulk electrons to cross (see Figure 5.3).

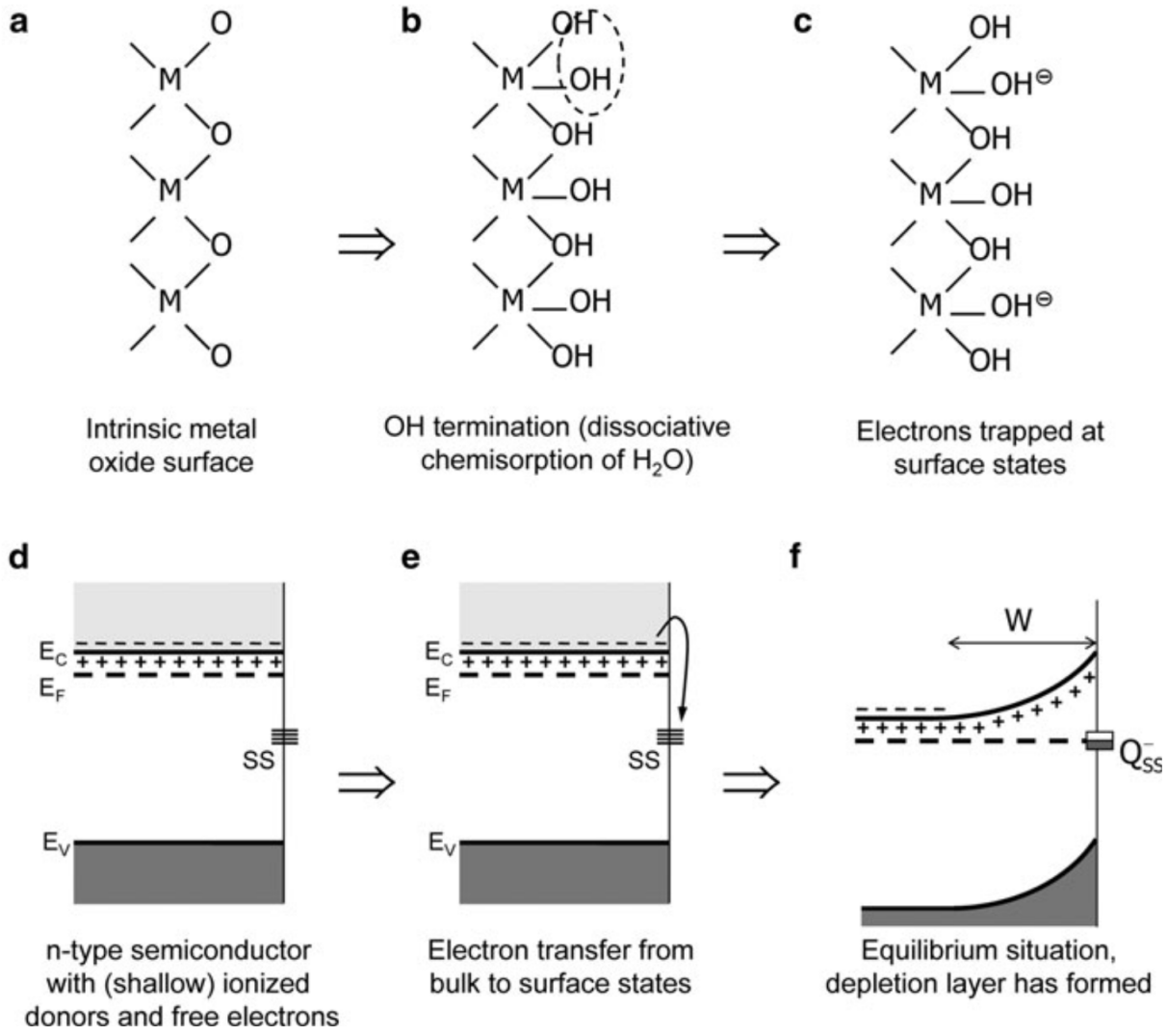

Figure 5.3: Conceptual illustration of the formation of depletion layers in metal oxides, where dissociative H_2O forms OH^--terminated groups on the surface of the metal oxide.(Van De Krol, 2012)

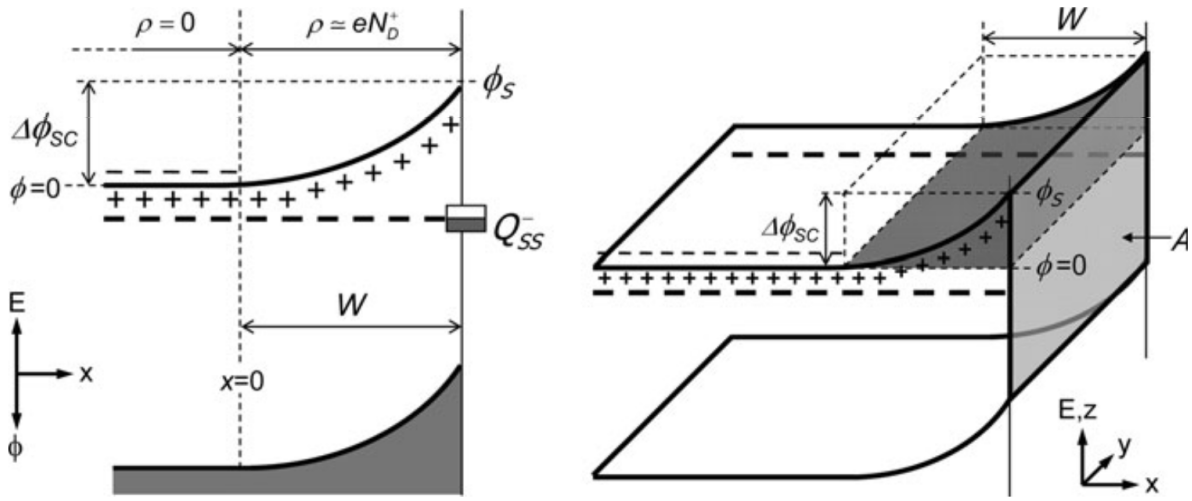

Figure 5.4: Visualization of the depletion layer in a metal oxide semiconductor. In this scheme, mobile holes flow into solution. (Van De Krol, 2012)

5.3.2 Depletion Layer

Upon formation of a depletion layer, an potential drop across the space charge layer occurs (as shown in Figure 5.4), and the resulting charge in the space charge region can be described as (Van De Krol, 2012)

$$Q_{SC} = \sqrt{2\epsilon_0 \epsilon_r e N_D A^2 \ (\ \phi_{SC} - \frac{kT}{e})} \tag{5.1}$$

where ϵ_0 is the vacuum permittivity, ϵ_r is the relative permittivity, N_D is the concentration of donors, A is the surface area of the semiconductor, ϕ_{SC} is the potential of the space charge, k is Boltzmann's constant, and T is temperature. This space charge region allows holes to move freely into solution, while creating a potential barrier for electrons.

However, other types of space charge layers can form in a semiconductor, including inversion, deep depletion, and accumulation layers (see Figure 5.5), which occur depending on Fermi level positioning before equilibrium. In inversion, the equilibrium Fermi level crosses the mid bandgap energy; this corresponds to a scenario in which a layer of minority carriers builds at the interface. For a deep depletion scenario, these minority carriers are consumed faster than they are generated, leaving an insulating surface layer. Finally, accumulation layers occur when an excess of minority carriers adsorb onto the surface, resulting in free majority carriers that accumulate near the surface.

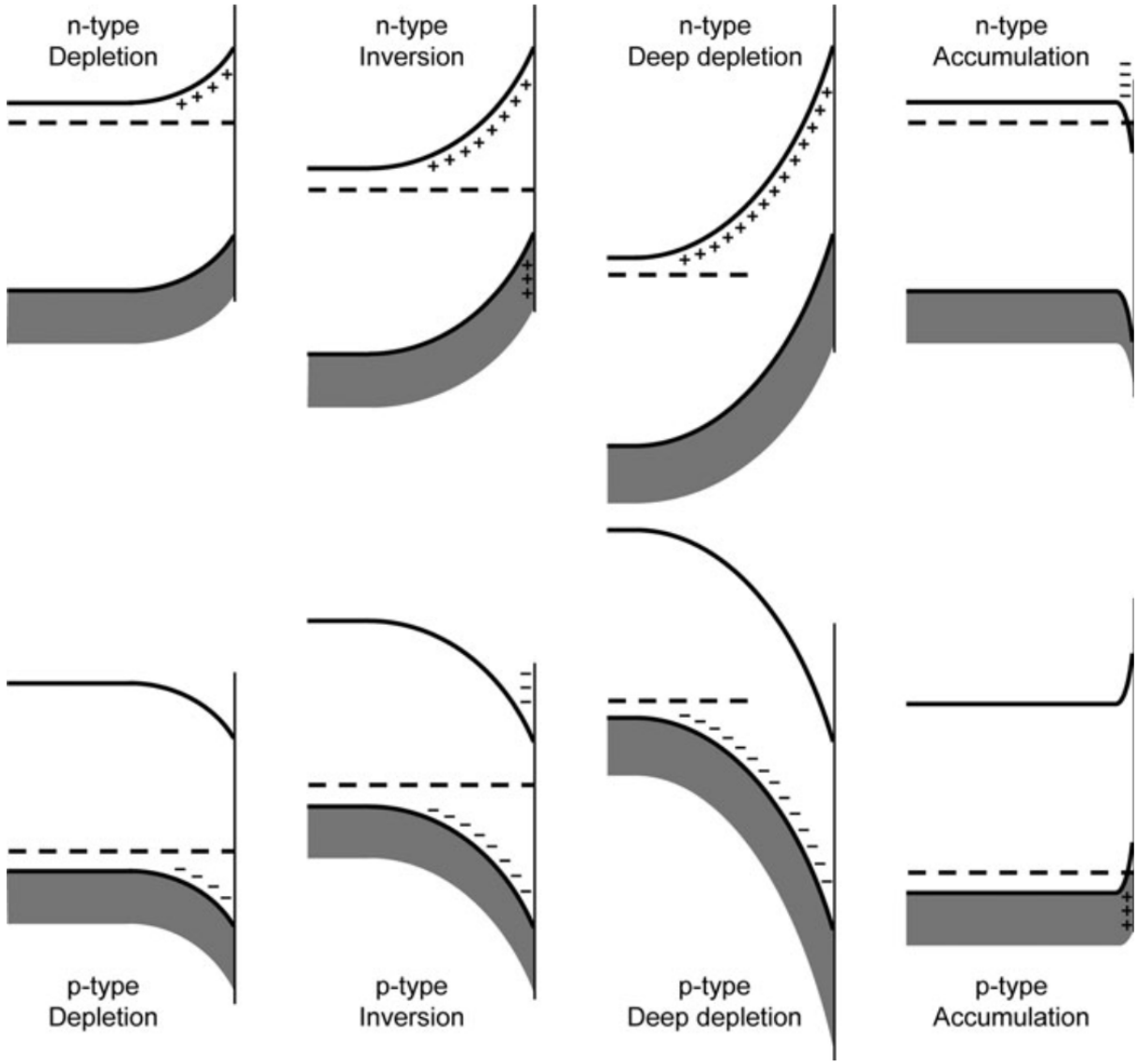

Figure 5.5: Band gap representation of depletion, inversion, deep depletion, and accumulation for n- and p-type electrodes. (Van De Krol, 2012)

5.3.3 Electrode-Electrolyte Interface

As in aqueous-electrolyte supercapacitors, a large potential drop across the Helmholtz layer, followed by a smaller potential drop across the Guoy-Chapman layer, dominate the electrical behavior at the electrode-electrolyte interface. However, there is no ion insertion at the surface of the material, as can be seen in certain pseudocapacitors. The structure of the electrode-electrolyte interface is discussed in more detail in Section 2.3.2.

5.4 Material choice

In the past, nanowires have shown three distinct improvements over un-textured substrates: (1) enhanced light trapping due to light concentrating properties of standing nanowires; (Krogstrup et al., 2013) (2) increased surface area, leading to increased active surface sites upon which water splitting can occur; and (3) reduced minority carrier distances, decreasing the rate of recombination and increasing charge separation.(Van De Krol, 2012) TiO_2 is an intrinsically n-type semiconductor material with an energy band gap of 3.2 eV. (Weber and Dignam, 1986) Its band edge positions straddle water redox potentials as shown in Figure 5.2. Moreover, TiO_2 production is well-known in the semiconductor industry, as TiO_2 is highly stable, even in a highly oxidizing aqueous environment. However, the state-of-art TiO_2 usage as a PEC photoanode is plagued by lower photocurrent due to poor light absorption. Moreover, previous work on texturizing TiO_2 is not able to produce high aspect ratio TiO_2 nanowires due to undesirable compact layers that can be observed at the bottom of the wire arrays.(Bolton et al., 1985) In this work, we fabricate high aspect ratio ZnO/TiO_2 nanowire arrays using a hybrid hydrothermal/atomic layer deposition (ALD) process. After growing the high aspect ratio ZnO nanowires using the hydrothermal methods, a uniform coating of TiO_2 was applied by ALD. The resulting structures show excellent onset voltage due to enhanced charge separation, which is induced by the geometry of our devices: by increasing the aspect ratio, travel distance of the minority carriers into the solution is reduced. Furthermore, TiO_2-coated ZnO nanoarrays show improved chemical stability over bare ZnO nanoarrays in aqueous solutions during photocatalysis.

5.5 Fabrication

A two-step hybrid process was used to fabricate the PEC water splitting devices, as shown in Figure 5.6. First, zinc oxide (ZnO) nanowires are fabricated by a hydrothermal process, serving as the template structure upon which the active material is deposited. Second, atomic layer deposition (ALD) was used to deposit 40 nm TiO_2. To fabricate ZnO, a seed solution of zinc acetate (Sigma) and ethanol were drop-casted onto n-type Si (100) wafers. The solution was left to form a quantum dot network on the surface of the Si wafers, rinsed with ethanol, and dried under nitrogen environment. The process was repeated 3 times to ensure adequate quantum dot formation. The wafer is annealed at 350 °C for 30 min to ensure

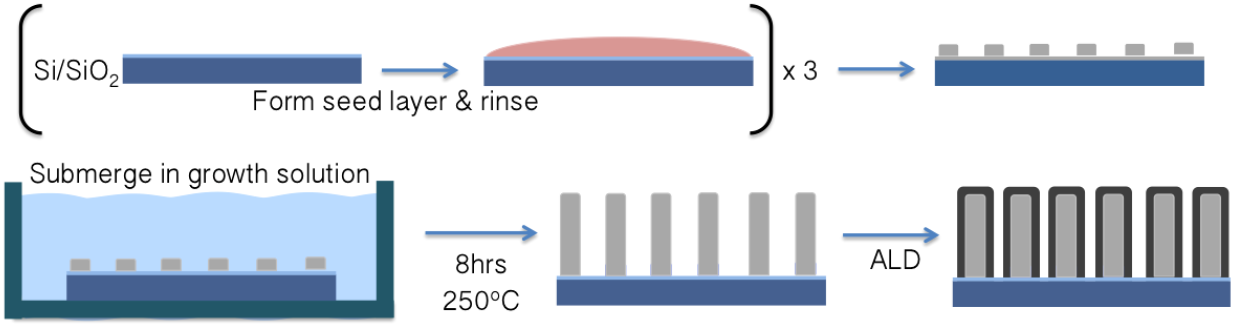

Figure 5.6: A hybrid ALD/hydrothermal process is used to fabricate the TiO_2@ZnO nanowires. ZnO nanowires are grown hydrothermally. First, a quantum dot seed layer is formed on the surface of an oxidized silicon wafer. The seed layer forms the basis upon which the nanowires grow. Next, the wafer is submerged into Zn-rich growth solution for 8 hours at 250°F; nanowire height can be tuned via growth time. Finally, the ZnO nanowires are coated with TiO_2 using ALD.

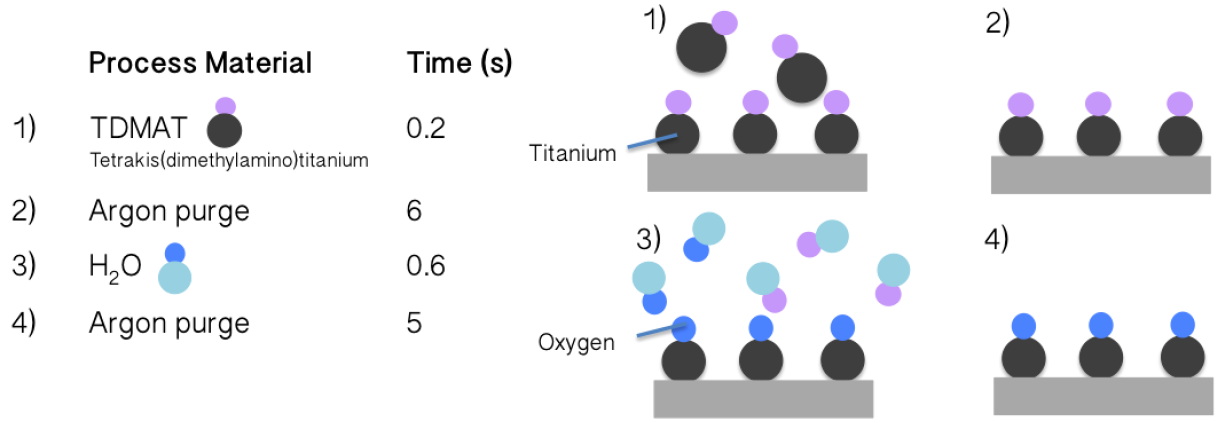

Figure 5.7: Process flow for ALD TiO_2. TDMAT is adsorbed onto a substrate and the excess is purged by argon. Next, H_2O enters the chamber and reacts with TDMAT in a self-limiting reaction; the excess H_2O and byproducts are purged by argon.

seed layer adhesion onto the wafer before submerged in a growth solution containing zinc nitrate hexahydrate (Sigma), hexamethylenetetramine (Sigma), and ammonium hydroxide (Alfa Aesar) at 90 °C for 8 hrs. The wafer was removed from the solution and cleaned with deionized water.

After drying the samples, uniform deposition of TiO_2 over ZnO nanowires was performed using ALD, as shown in Figure 5.7. ALD, a highly precise chemical vapor deposition method, creates uniform, conformal coverage of polycrystalline TiO_2 using a self-limiting reaction. To deposit TiO_2, Tetrakis(dimethylamido)titanium (TDMAT) was introduced into the deposi-

tion chamber through an Argon carrier gas and allowed to adsorb onto the substrate surface for 0.6 s. Excess (unadsorbed) TDMAT was removed from the chamber with Argon gas for 5 s. Next, H_2O was introduced for 0.25 s, beginning a self-limiting reaction with adsorbed TDMAT. The excess H_2O and reaction byproducts were removed with Argon gas for 5 s, leaving a single layer of TiO_2. In this way, gaseous precursors were introduced in a systematic and cyclic manner to create a self-limiting reaction–one layer of TiO_2 was deposited per cycle. This makes ALD an ideal deposition method for high quality, Ångström-level precision over very high aspect ratio substrates. The ZnO nanowire array was coated by 1000 cycles of thermally grown ALD TiO_2 (0.4/cycle) at a process temperature of 250°C, as reported in a previous work.(Park et al., 2017)

5.6 Cell efficiency

The ultimate efficiency of a cell (adapted from (Hisatomi et al., 2014)) can be described by the following equations. First, the solar-to-hydrogen efficiency is:

$$STH = \frac{Representative\ H_2\ output\ energy}{Energy\ of\ incident\ solar\ light} = \frac{r_{H2} \times \Delta G}{P_{sun} \times S} \tag{5.2}$$

where r_{H2} is the rate of hydrogen production; ΔG is the change in Gibbs energy; P_{sun} is the energy flux of irradiation; and S is the area of the electrode. However, electrodes that require a bias voltage in order to produce measurable photocurrent require voltage compensation in order to calculate cell efficiency. Therefore, the applied-bias-compensated solar-to-hydrogen efficiency and a half-cell (to be used with a two-electrode cell) is employed:

$$AB - STH = \frac{I \times \eta_F \times (V_{th} - V_{bias})}{P_{sun}} \tag{5.3}$$

where I is the photocurrent density; η_F is the faradaic efficiency, V_{th} is the theoretical voltage for water splitting (1.23 V); and V_{bias} is the applied bias potential. The half-cell STH for a photoanode is therefore:

$$HC - STH = \frac{I \times (E_{O_2/H_2O} - E_{RHE})}{P_{sun}} \tag{5.4}$$

where E_{O_2/H_2O} is the theoretical standard electrode potential for the $O_2 + 4H^+ + 4e^- \rightarrow 2H_2O$ reaction vs. RHE, and E_{RHE} is the pH-dependent potential of the photoanode in the electrolyte is represented as:

$$E_{RHE} = E_{measured} - E^0_{Ag-AgCl} + \frac{RTln10}{F}pH \tag{5.5}$$

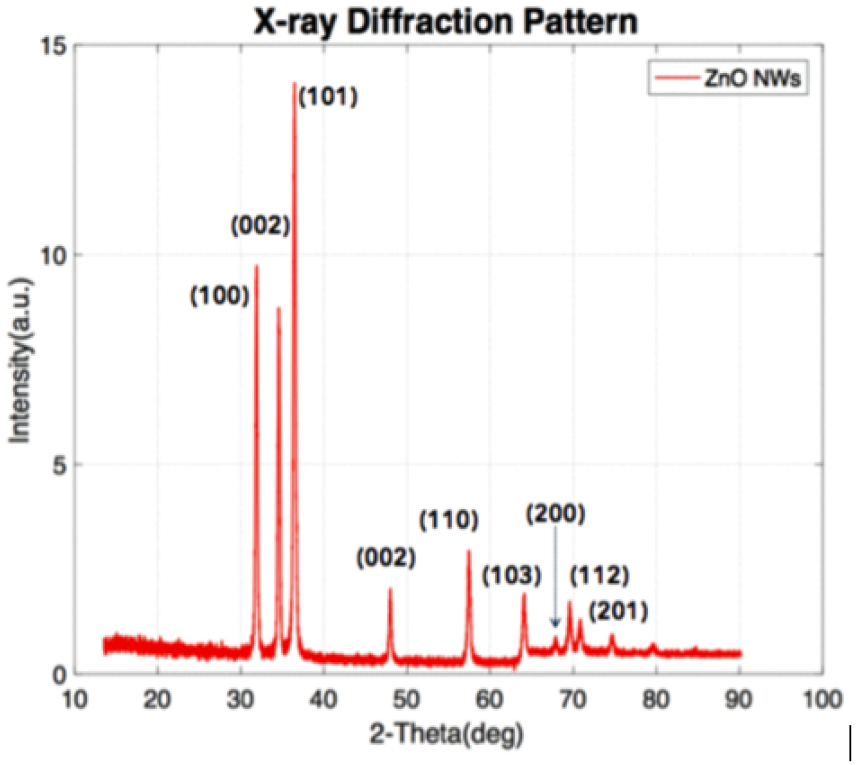

Figure 5.8: X-ray diffraction pattern of ZnO nanowires, confirming both elemental composition and high crystallinity.

where $E_{measured}$ and $E^0_{Ag-AgCl}$ are the potential measured relative to an Ag/AgCl reference electrode and the standard potential of the Ag/AgCl reaction, respectively. R, T, F are the gas constant, temperature, and Faraday constant, respectively. Therefore, the cell efficiency is not only dependent on the measured photocurrent density but also the applied bias potential. Furthermore, texturization, catalysts, and co-electrodes to promote charge separation have been readily shown as methods to increase photocurrent, while fewer work exists on methods to decrease onset voltage, aside from material choices.

5.7 Characterization

The phase structure of hydrothermally grown ZnO nanowires was characterized using powder X-ray diffraction (XRD). Figure 5.8 displays the X-ray diffraction peaks confirm excellent crystallinity and hexagonal wurtzite ZnO phase. (JCPDS card No. 36-1451). The surface morphology of the nanowire array was analyzed using a field emission scanning electron microscopy (FESEM). SEM images before ALD processing show highly ordered, 10 μm tall nanowires with diameters of less than 50 nm. Furthermore, the nanowires show polygonal cross-sections, implying single-crystalline nature (Figure 6.3a, d, g). SEM images of the

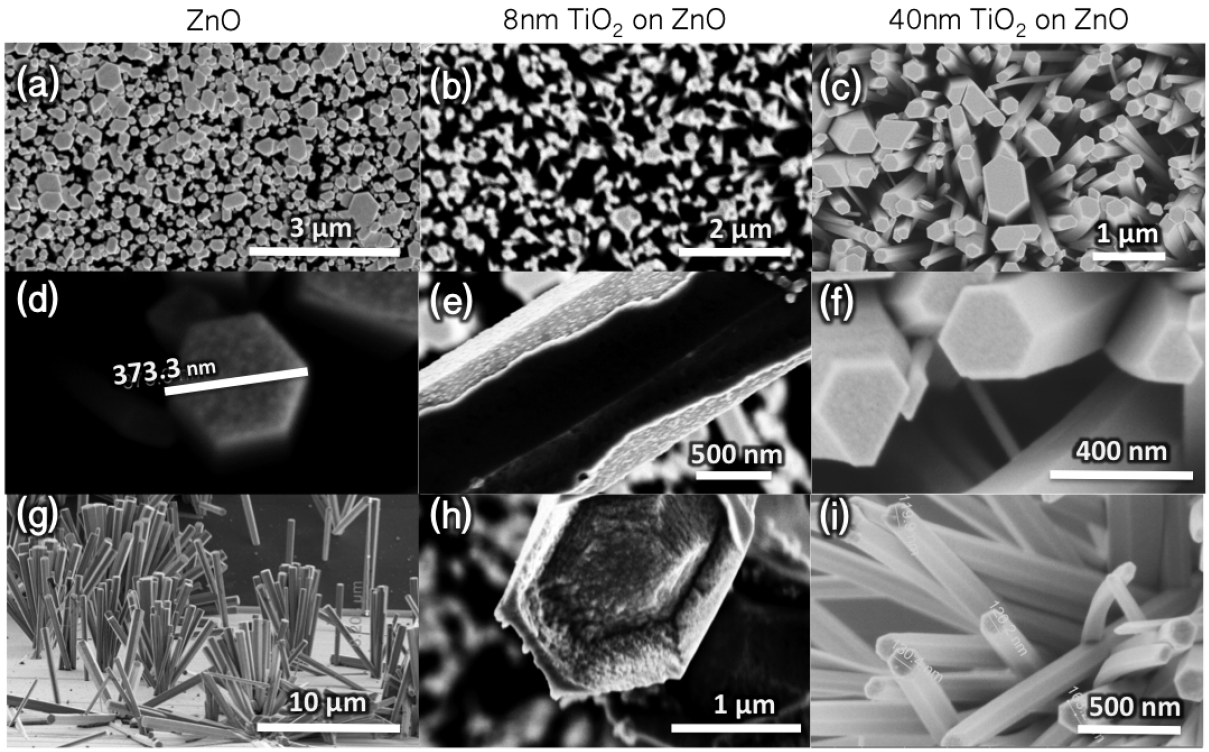

Figure 5.9: SEM images of ZnO, 20 cycles TiO_2@ZnO (incomplete coverage), and 1000 cycles TiO_2@ ZnO (complete and conformal coverage). (a) top-down view of ZnO nanowire forest, (b) top-down view of 20 cycles-TiO_2-coated ZnO nanowire forest, (c) top-down view of 1000 cycles-TiO_2-coated ZnO nanowire forest, (d) single nanowire view of ZnO, showing hexagonal shape (single-crystalline), (e) single nanowire view of 20 cycles TiO_2 on ZnO, showing incomplete coverage, (f) conformally and fully coated 1000 cycles TiO_2@ZnO, (g) side-view of ZnO nanowires, (h) side-view of 20 cycles TiO_2@ZnO, (j) side-view of 1000 cycles TiO_2@ZnO.

nanowire array post-ALD shows complete coverage of TiO_2. As shown in Figure 6.3a and b, a single ZnO nanowire is uniformly coated by TiO_2 when coated with at 1000 ALD cycles (Figure 6.3c, f, j), as opposed to 20-cycle coatings of TiO_2, which shows incomplete coverage (Figure 6.3b, e, h). A transmission electron microscopy (TEM) was employed for the characterization of the single nanowire. Figure 5.10a exhibits a single ZnO nanowire with hexagonal cross section. Figure 5.10b shows complete and conformal coverage of 1000-cycle TiO_2 on ZnO nanowries. In contrast to previous work on TiO_2, we are able to achieve tall, highly ordered ZnO/TiO_2 arrays. By using ALD to deposit a thin coating of TiO_2, we have further limited the distance of travel for minority carriers, minimizing recombination and ensuring better charge separation. The favorable geometry and high quality coating with ALD allows us to achieve stable devices with excellent onset voltage, producing photocurrent

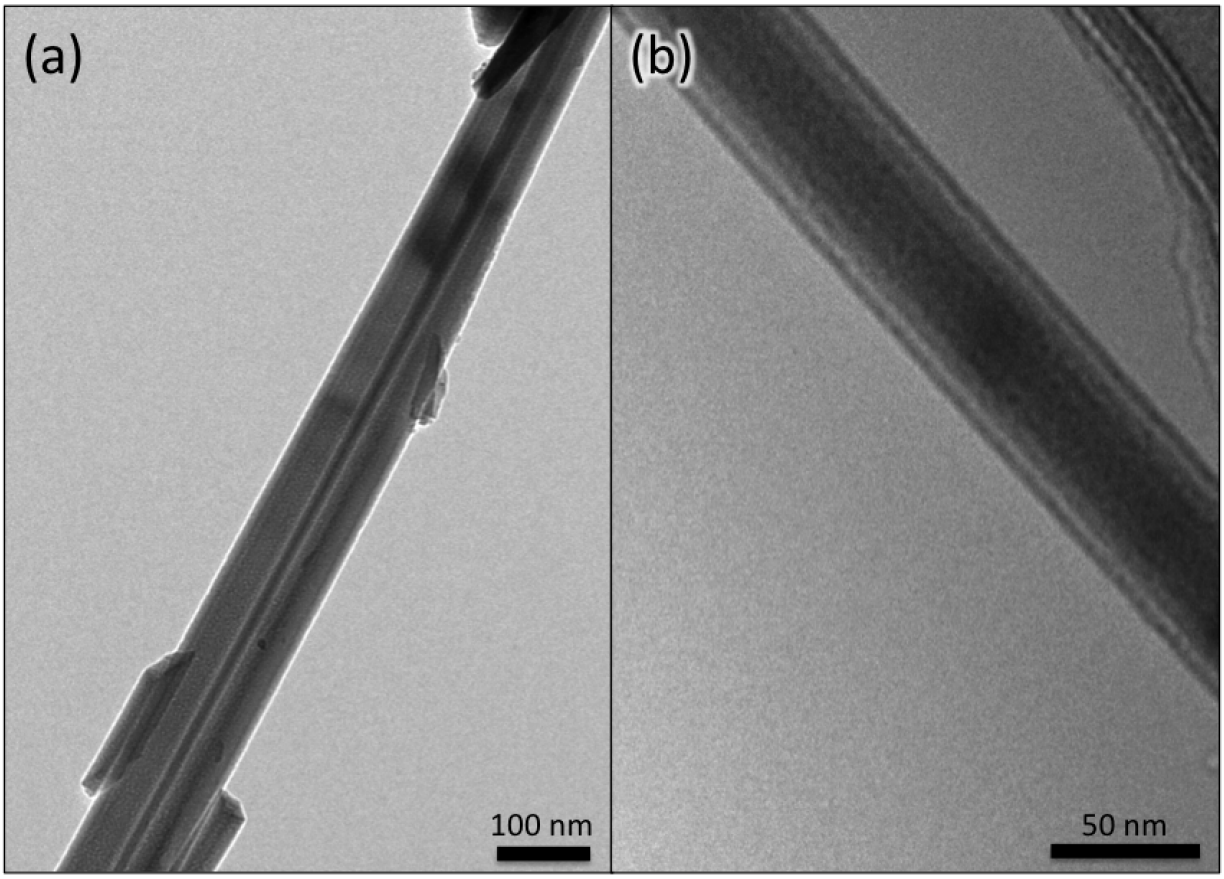

Figure 5.10: (a) TEM image of a lone ZnO nanowire, with hexagonal shape. (b) TEM image of 1000 cycle TiO_2@ZnO nanowire, showing conformal coverage along the body of the nanowire.

at extremely low bias voltage.

5.8 Results

Electrical contact is established using copper tape and insulated tin wire. To isolate the active material, electrodes were passivated onto a glass substrate using epoxy. Photoelectrochemical water splitting was tested using a 3-electrode set-up in 0.5 M H_2SO_4 solution vs. Ag/AgCl with a platinum wire as the counter electrode. An Asahi, AM 1.5 Xenon lamp was used as the solar simulator and the system was enclosed in TB4 Thorlabs black-out hardboard (5 mm thick with foam core). Electrochemical measurements were conducted using a Gamry Ref. 600 potentiostat (Figure 5.11b). Linear sweep voltammetry was conducted from 0 V vs. Ag/AgCl to 1 V vs. Ag/AgCl, since the aqueous solution had an electrochemical voltage

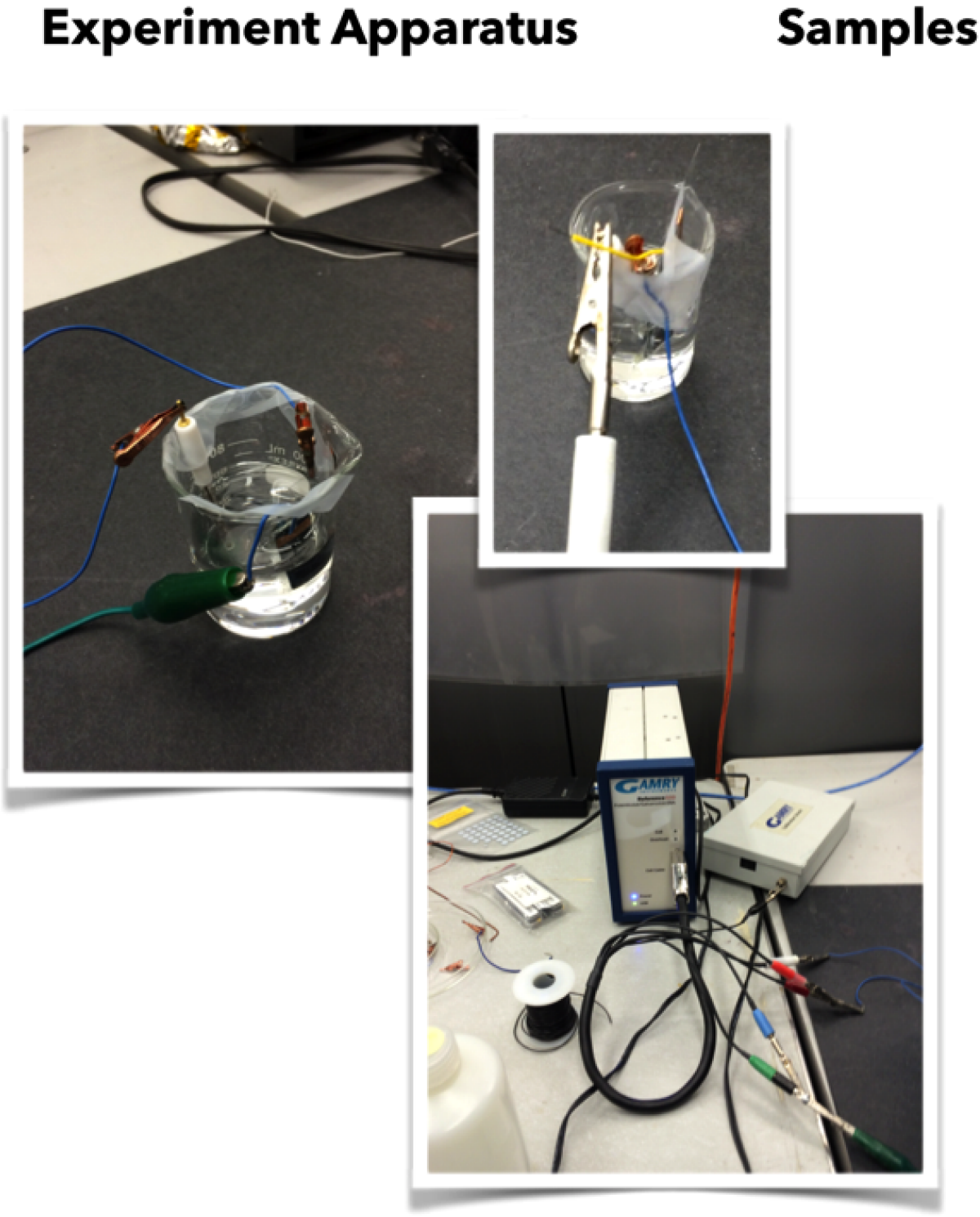

Figure 5.11: The cell is tested electrochemically using a Gamry Ref. 600 with a 3-electrode setup vs. Ag/AgCl. The counter electrode is platinum.

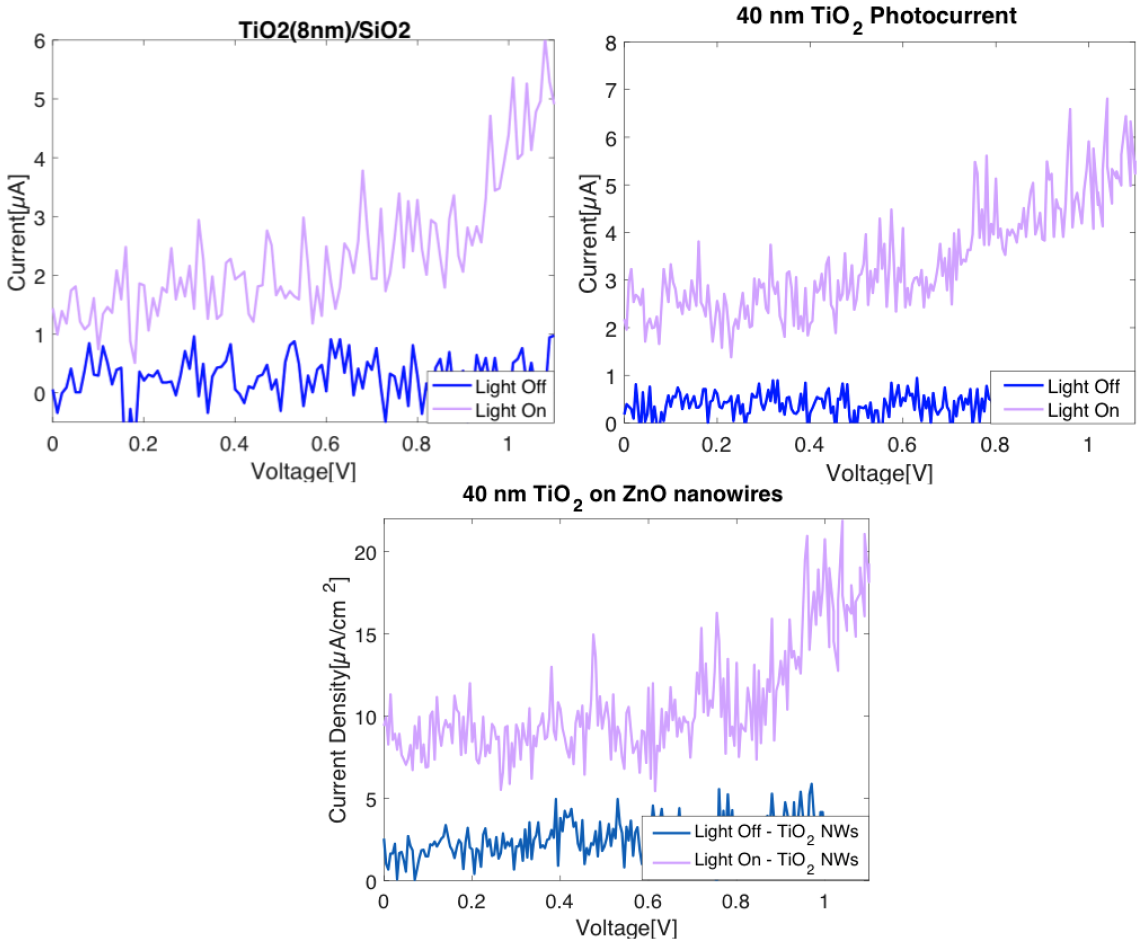

Figure 5.12: Linear sweep voltammetry under lit and dark conditions. (a) planar 20 cycle TiO_2 on silicon shows photoresponse, with photocurrent ranging from 1–5 μA. (b) planar 1000 cycle TiO_2 on silicon shows photocurrent ranging from 1-6 μA. (c) high aspect ratio TiO_2@ZnO show significantly increased photocurrent (1 order of magnitude increase).

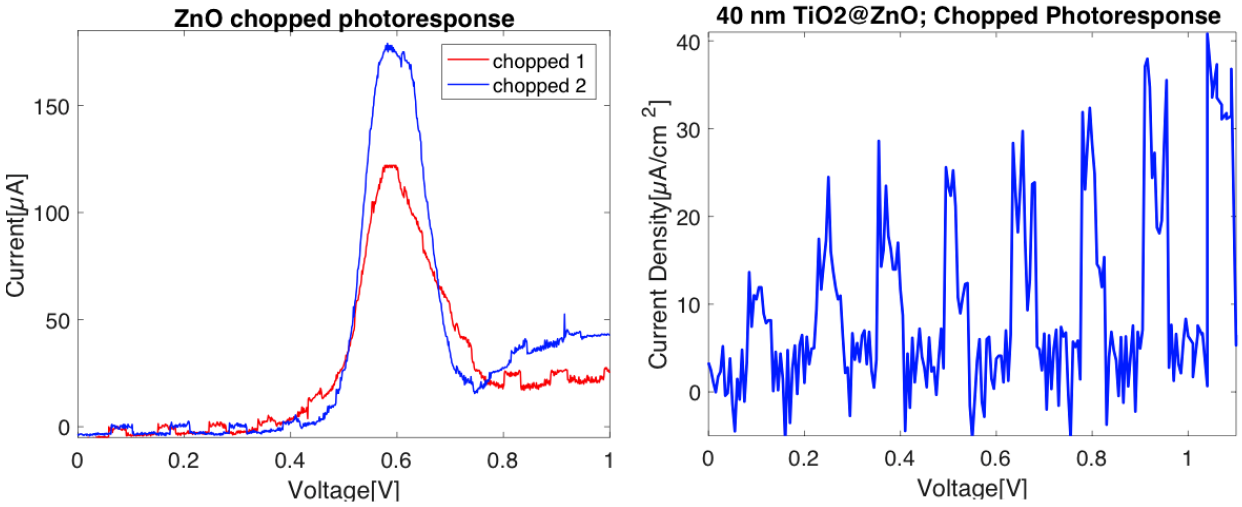

Figure 5.13: Chopped scans (alternating dark and lit conditions) for (a) bare ZnO nanowires. As can be seen by the linear sweep, hydrothermally grown ZnO nanowires exhibit undesirable side reactions, which obscure photocurrent and compromise stability of the device. In contrast, (b) 1000 cycle TiO_2 shows no such reactions, and significant difference between on/off conditions.

limit of 1.2 V (standard electrode potential of 1.23 V for the $O_2 + 4H^+ + 4e^- \rightarrow 2H_2O$ reaction). The scans were conducted in dark conditions (covered in a black-out cardboard housing) and light conditions, as well as chopped light–dark alternating with light.

5.9 Discussion

As shown in Figure 5.12, the ALD TiO_2 show significant differences in current outputs between light and dark conditions, implying photocurrent under lit conditions, with photocurrent increasing with increasing voltage. While the signal-to-noise is poor due to the low photocurrent, Figure 5.12 also shows that photocurrent is generated at very low voltages (low onset voltage). The planar structure made of 1000-cycle TiO_2 coatings shows only marginal improvement in photocurrent over that of 20-cycle TiO_2 (Figure 5.12a, b) structure, while texturized TiO_2 as shown in Figure 5.12c, has significantly increased photocurrent, almost an order of magnitude higher at 0 V vs. Ag/AgCl. Furthermore, it is noted that the electrode performances in these tests are in the absence of surface catalysts, which have been shown to greatly increase detectable photocurrent.

As seen in Figure 5.13a, the PEC response of the bare ZnO nanoarray is mostly obscured by side reactions, despite cleaning the ZnO with ethanol and DI water. The side reactions cause peaking and sharp increases in current. However, when coated with ALD TiO_2, the electrode is significantly more stable (Figure 5.13b). The results suggest that the

hydrothermal growth method for ZnO results in impurities and instabilities that make the ZnO nanowire array unsuitable for photocatalytic water splitting. However, these instabilities are not observed in the ALD TiO_2-coated samples, implying that TiO_2 is the material to stabilize the system as demonstrated in a previous work.(Liu et al., 2013b)

Since the grain boundaries of ALD TiO_2 are potential recombination sites, the TiO_2 susceptible to low performance as a PEC electrode. In contrast, the ZnO nanowires are single-crystalline and less vulnerable to recombination sites and by limiting the TiO_2 to a 40 nm coating on the ZnO nanowire, travel distance of minority carriers to a single-crystalline substrate is greatly reduced, promoting conductivity and reducing recombination. Since the band gap of ZnO relative to TiO_2 is smaller, the generated photoelectrons in TiO_2 should not experience build-up and subsequent recombination at the semiconductor junction.

5.10 Conclusion

High aspect-ratio and vertically ordered ZnO/TiO_2 nanoarrays as long as 10μm and less than 50nm in diameter were successfully synthesized for applications in solar-powered hydrogen (H_2) gas harvesters. Hybrid hydrothermal/ALD processing was used to achieve high aspect ratio and high quality nanowire arrays. Surface morphology and phase structure were analyzed to confirm TiO_2-coated ZnO nanowires. Photoelectrochemical responses of synthesized nanowires were measured to investigate their performance as hydrogen gas harvesters. Nanowires with TiO_2 demonstrated improved stability over bare ZnO nanowires during photocatalysis with low bias voltage. Results show that favorable geometry and high quality nanowires not only enhanced chemical stability but also improved required bias voltage to yield photocurrent.

Chapter 6

ALD Black Titania

This work presents the first demonstration of atomic layer deposited (ALD) black titania (b-TiOx), to the best of our knowledge. By fabricating b-TiOx using ALD we have accomplished four distinct achievements: (1) development of a direct deposition method of b-TiOx without the need for deoxygenation annealing, as required by current fabrication processes; (2) the ability to deposit b-TiOx onto highly porous materials with *Å*ngstr*ö*m-level precision; (3) increased response to the solar spectrum over TiO_2, as demonstrated by >10x improvement in detectable photocurrent when compared to TiO_2; (4) >7x improvement in capacitance when comparing a b-TiOx supercapacitor to a TiO_2 supercapacitor. As such, this work allows for more robust and precise black titania deposition, opening up new possibilities of devices based on b-TiOx.

In this chapter, previous approaches to fabricating black titania, propeties and applications of black titania, a material first synthesized in 2011, will be introduced. A new, direct deposition method using atomic layer deposition will then be introduce, and first demonstrations of ALD black titania for photocatalytic water splitting shown.

6.1 Introduction

Conventional titanium dioxide (TiO_2) remains one of the most widely studied metal oxide semiconductors for MEMS applications, known for its chemical stability under highly oxidizing environments and ability to absorb ultraviolet (UV) light. However, its bandgap of 3.05 eV renders it incapable of absorbing most of the solar spectrum (UV accounts for <5 % of the solar spectrum). TiO_2 is also electrically insulating. In the past decade, black titania (b-TiOx), oxygen-deficient TiO_2, has emerged as an alternative to conventional TiO_2. Increased oxygen vacancies allow for bandgap narrowing, (Chen et al., 2011) improve solar absorption, (thus, b-TiOx′ black color) (Chen et al., 2011) and increase supercapacitive performance.(Lu et al., 2014)

However, all state-of-the-art fabrication techniques require de-oxygenating annealing of

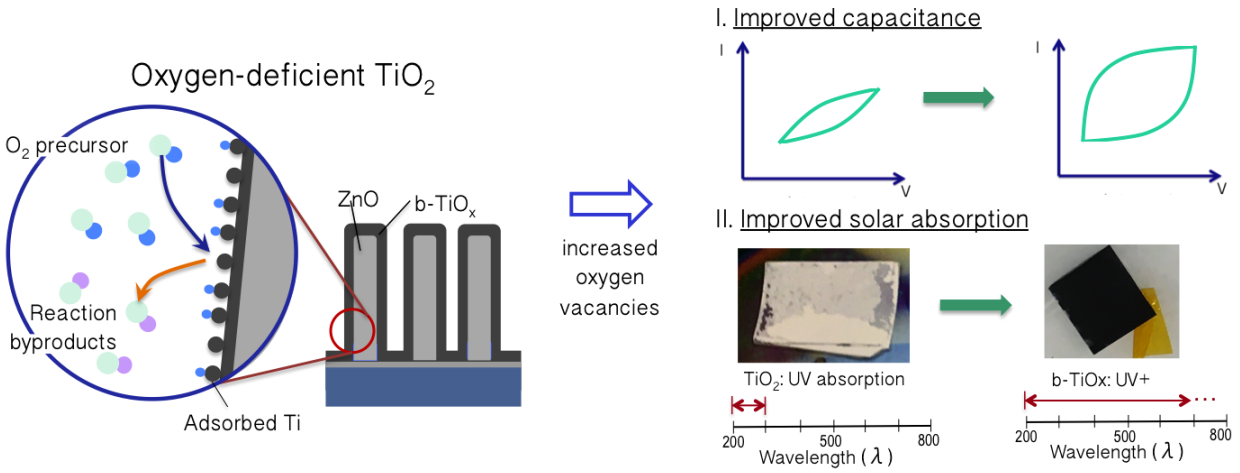

Figure 6.1: Ti- and O_2-containing ALD gas-phase precursors designed to form self-limiting form black titania (b-TiOx) without de-oxygenation. By carefully controlling oxygen precursors that are allowed to react onto the surface of the highly texturized substrate, we are able to induce increased oxygen vacancies in b-TiOx lead to improved (1) photocurrent due to increased light absorption of the solar spectrum and (2) capacitance due to increased conductivity, and (3) noticeable optical change in color.

TiO_2, usually in the presence of hydrogen gas.(Chen et al., 2011) The first discovery of b-TiO_2 consisted of hydrogen annealing of commercial TiO_2 at 20 bar, 500°C for 5 days.(Lu et al., 2014) Various work has been able to reproduce b-TiOx fabrication via annealing under a hydrogenated condition for long periods of time, (Chen et al., 2011) as well as achieving different colors of TiOx, such as pale yellow or grey.(Lu et al., 2014) Though hydrogenated TiOx has been able to achieve the band gap narrowing to create b-TiOx, work centered around annealing in a low-oxygen environment, such as a 5 % H_2/95 % Ar mixture, has also been shown to produce TiO_2 nanoparticles of varying colors. (Shin et al., 2012)

Attempts to texturize b-TiOx in the literature begin with a texturized TiO_2 substrate, with annealing maintaining the original texturization. As in previous reports of b-TiOx fabrication, annealing TiO_2 nanotubes under varying low-oxygen conditions were shown to yield TiOx nanotubes of varying colors. (Liu et al., 2014)

Recent attempts to fabricate b-TiOx without hydrogen annealing consist of co-heating aluminum and TiO_2 at 850°C and 500°C, respectively, for 4 hours. (Cui et al., 2014) Attempts at co-reduction of Ti-containing precursors with other metals, such as co-reduction of $TiCl_3$ with Zn at 180°C for 6 hrs, do not produce b-TiOx, but rather grey to dark blue TiOx. (Zhao et al., 2014) Similarly, high voltage electrochemical reduction of titanium foil under highly oxidizing conditions is able to yield b-TiOx but requires large overpotentials (40–60 V) and post-treatment. (Li et al., 2014)

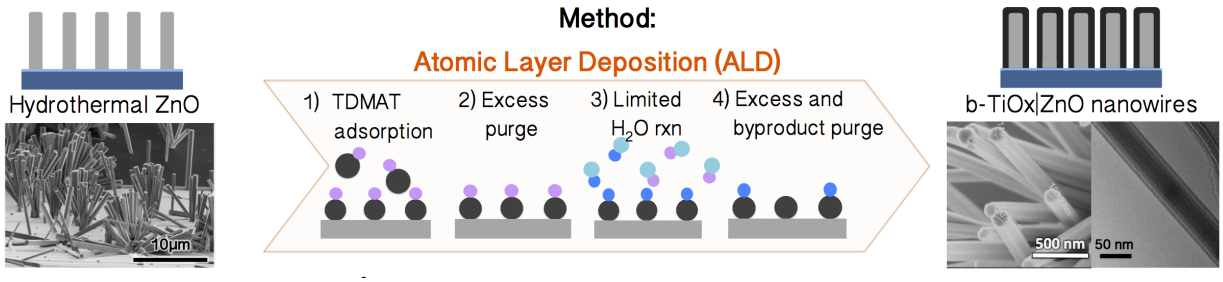

Figure 6.2: Process flow for b-TiO_2 ALD. TDMAT adsorbs and excess is purged by argon. Next, H_2O reacts with TDMAT in a self-limiting reaction; the excess H_2O and byproducts are purged.

In contrast, our system allows for a more precise, direct, layer-by-layer deposition of de-oxygenated TiO_2 over texturized and high-aspect ratio substrates with excellent conformality. This is achieved by ALD, a thin film deposition technique that uses a sequential pulsing of Ti- and O-containing gaseous precursors to achieve highly conformal, highly precise coatings. By limiting oxygen reactants in the chamber, we are able to achieve de-oxygenated b-TiOx without the need for deoxygenation. The b-TiOx showed increased conductivity (>7x improvement in capacitance, as compared to ALD-TiO_2) and significantly increased photocurrent (>10x improvement over ALD-TiO_2) (Figure 6.1).

6.2 Fabrication

B-TiOx is deposited by ALD in a Cambridge Fiji tool. First, Tetrakis(dimethylamido)titanium (TDMAT) is flown into the chamber using an argon (Ar) carrier gas at 260 sccm for 0.2 s; TDMAT adsorbs onto the surface of the substrate and excess is purged via Ar for 5 s. Next, H_2O is introduced via 260 sccm Ar carrier gas for 0.06 s. Excess H_2O and reaction byproducts are purged via Ar for 5 s. The process is repeated to grow b-TiOx with a growth rate of roughly 0.4 $\AA$/cycle (Figure 6.2). The ZnO nanowire array was coated by 1000 cycles of b-TiOx recipe under a process temperature of 250 °C.

The ZnO substrate was grown via quantum dot seed network formation and subsequent hydrothermal growth. (Park et al., 2017) First, a seed solution of zinc acetate (Sigma) and ethanol were drop-casted onto n-type Si (100) wafers. The solution was left to form a quantum dot network on the surface of the Si wafers, rinsed with ethanol, and dried under a nitrogen environment. The process was repeated 3 times to ensure adequate quantum dot formation. The wafer is annealed at 350 °C for 30 min to ensure seed layer adhesion onto the wafer before being submerged in a growth solution of zinc nitrate hexahydrate (Sigma), hexamethylenetetramine (Sigma), and ammonium hydroxide (Alfa Aesar) at 90 °C for 8 hrs. The wafer was removed from the solution and cleaned with deionized water. Electrochemical characterization was performed using a 3-electrode set-up in 0.5 M H_2SO4

solution vs. Ag/AgCl with a platinum wire as the counter electrode.

6.3 Performance Parameters

Electrochemical measurements were conducted using a Gamry Ref. 600 potentiostat. Linear sweep voltammetry and cyclic voltammetry was conducted from 0 V vs. Ag/AgCl to 1 V vs. Ag/AgCl, since the aqueous solution had an electrochemical voltage limit of 1.2 V (standard electrode potential of 1.23 V for the $O_2 + 4H^+ + 4e^- \rightarrow 2H_2O$ reaction).

For photoelectrochemical performance, an Asahi AM 1.5 Xenon lamp was used as the solar simulator, and the system was enclosed in TB4 Thorlabs black-out hardboard (5 mm thick with foam core). Photoelectrochemical scans were conducted in dark conditions and light conditions. Samples were prepared by first establishing electrical contact using copper tape and insulated tin wire. To isolate the active material, electrodes were passivated onto a glass substrate using epoxy.

6.4 Characterization

SEM images of b-TiOx-coated ZnO nanowire arrays, as well as corresponding EDS spectra, are shown in Figures 6.3 and 6.5. The nanowires are roughly 1 μm in diameter and grow to 8 μm in height with conformal and complete coverage of b-TiOx. Previous work conducted on the ZnO nanowires show single-crystalline ZnO with hexagonal wurtzite ZnO phase. (Park et al., 2017) The EDS spectra of the entire system confirm oxygen deficiency, as Ti:O is less than 1:2, even accounting for oxygen in ZnO nanowires. Figure 6.4 shows the XPS spectra for the b-TiOx, and show the binding energies for Ti and O, respectively, showing $Ti_2p_3/2$, $Ti_2p_1/2$, and O(1s), with no significant impurities or dopants other than surface carbon impurities. Optical images also show a distinct color change from white to black (see Figure 6.6).

6.5 Electrochemical Testing

As shown in previous works (Kao et al., 2016), increased oxygen vacancies in a TiO_2-based matrix will increase capacitance due to induced charge storage under the surface of the electrode. Capacitive abilities of planar TiO_2, planar b-TiOx, and b-TiOx—ZnO nanowire arrays were tested using cyclic voltammetry in 0.5 M H_2SO4 vs. Ag/AgCl, as shown in Figure 6.7. Planar TiO_2, an insulator, showed capacitance of 5.9 μF/cm2. By using oxygen vacancy-rich b-TiOx, the capacitance increased >7x, reaching 42 μF/cm2. The deposition method of ALD also allows for the deposition of b-TiOx over high surface area mateirals such as ZnO nanowires. By increasing the surface area of the active b-TiOx, thus increasing the active storage area of the system, we are able to achieve a capacitance of 2100 μF/cm2. ALD

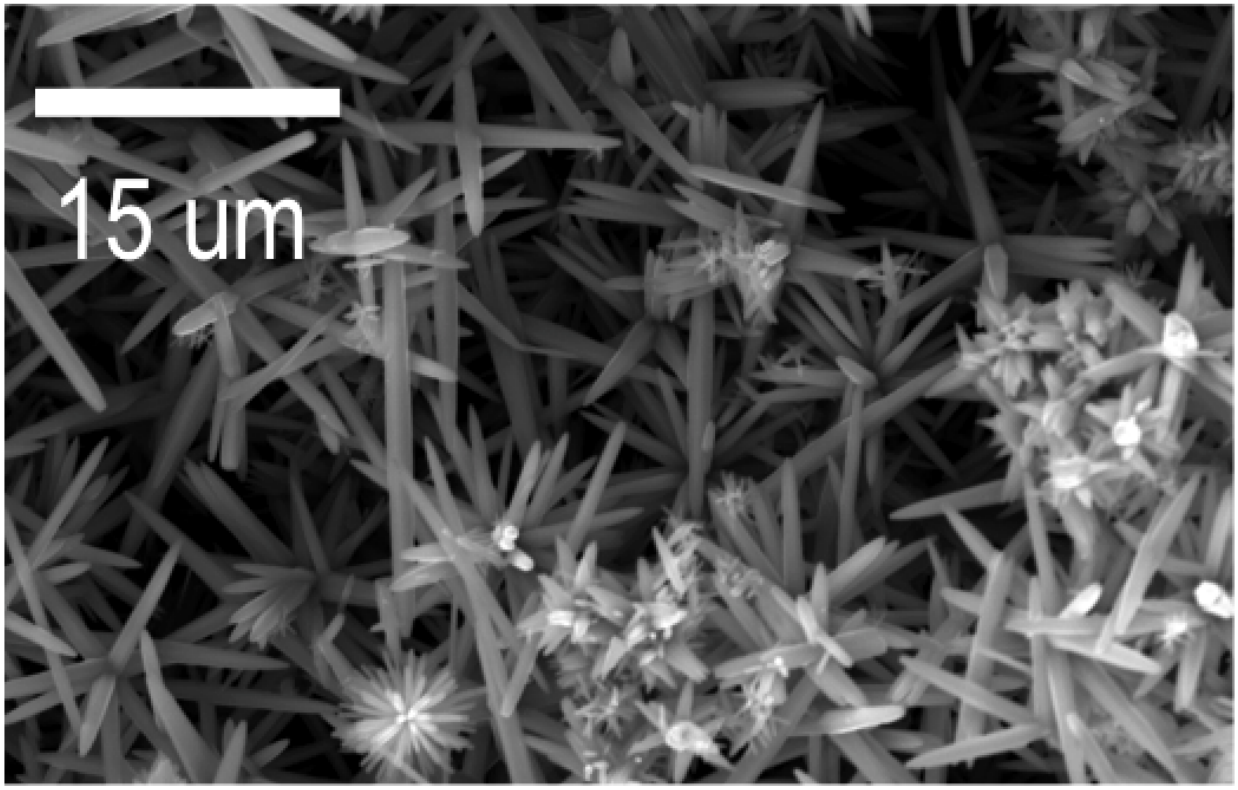

Figure 6.3: SEM images of b-TiOx-coated ZnO nanowires.

b-TiOx and ALD TiO_2 were used as PEC hydrogen harvesting materials, as shown in Figure 6.8. Indeed, TiO_2 was the first material used to show water splitting effects, the phenomenon whereby photogenerated electron-hole pairs oxidize and reduce water, forming oxygen and hydrogen gas (Fujishima and Honda, 1972). However, efficient TiO_2-based PEC cells have yet to be found, since TiO_2′s large bandgap only allows absorption in the UV range. Under testing in a lit and dark condition for PEC water splitting activity; ALD b-TiOx on ZnO nanowires generate detectable photocurrent an order of magnitude greater than that of ALD TiO_2 on ZnO nanowires. The increased photocurrent indicates b-TiOx′ improved absorption of the solar spectrum as compared to that of TiO_2. As reported in previous work, ALD TiO_2 has been shown to be a stabilization layer for the ZnO nanowires, which, when grown using a hydrothermal method, show undesirable side reactions that eclipse the photoelectrochemical effect. (Park et al., 2017) Similarly, ALD-b-TiOx also shows stabilization effect for the ZnO nanowires, with no undesirable peaking under lit or dark conditions, indicating that b-TiOx, though it has a smaller bandgap, is capable of similar stability uses as TiO_2.

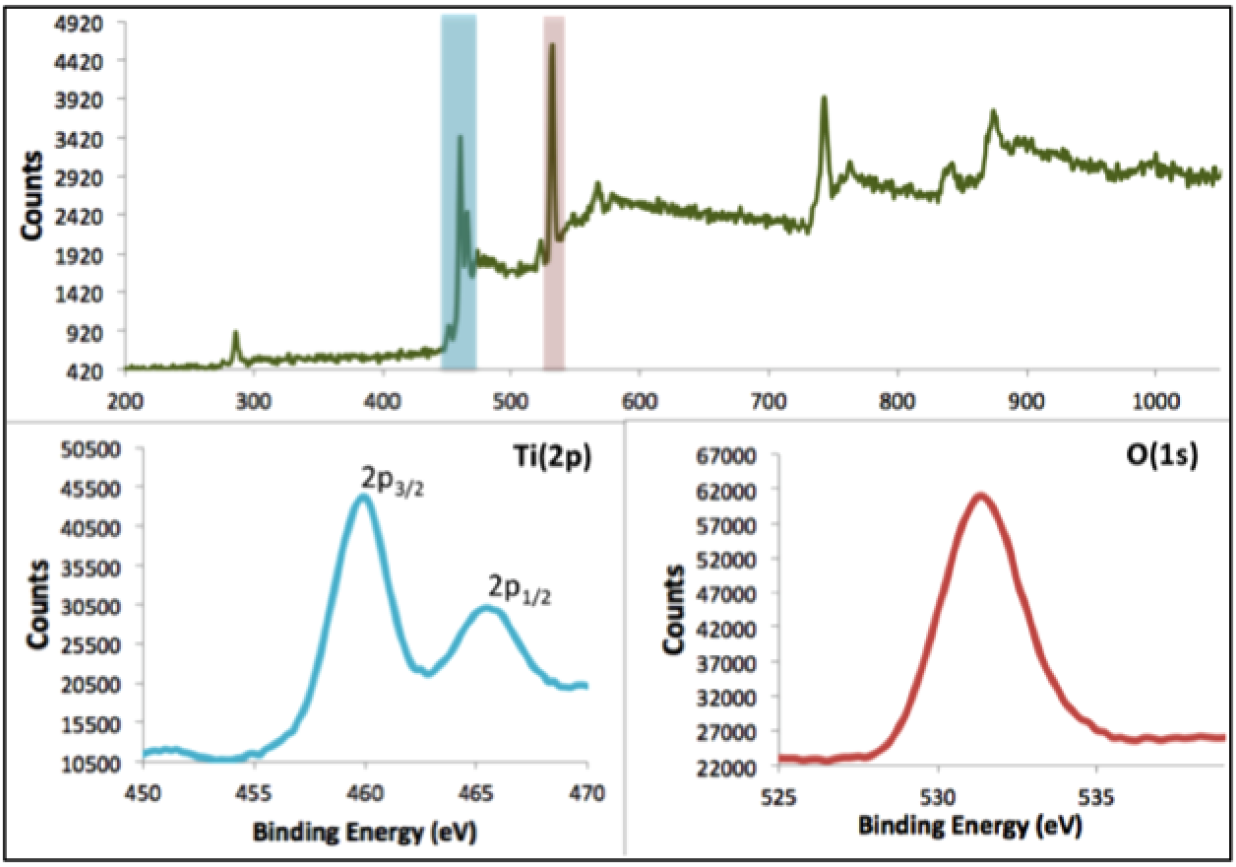

Figure 6.4: Corresponding XPS of b-TiOx show expected binding energies consistent with Ti2p3/2, Ti2p1/2, and O, without any dopants or impurities.

6.6 Conclusion

By utilizing ALD, we were able to achieve direct, precise, conformal coatings of b-TiOx over high surface area ZnO nanowire arrays, via limiting oxygen precursor allowed to react on the surface of the substrate. By inducing oxygen vacancies within the TiO_2 matrix, we are able to achieve increased capacitance when used as a supercapacitor material, as well as increased solar absorption over TiO_2. Detectable photocurrent (between lit and dark conditions) on an ALD b-TiOx-based photoelectrochemical device was two orders of magnitude larger than that of a conventional ALD TiO_2 device. Additionally, ALD b-TiOx was able to show the same stabilization properties that conventional ALD TiO_2 show on ZnO nanowires, compared to previous work.

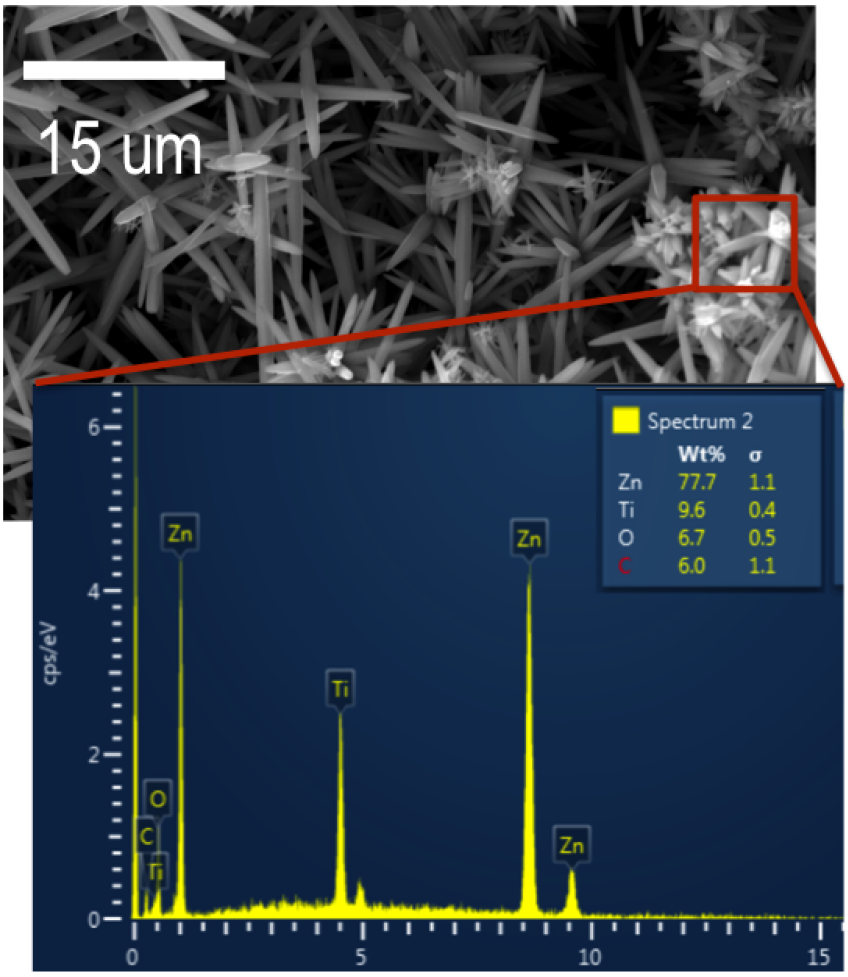

Figure 6.5: SEM/EDS images of b-TiOx—ZnO arrays. ZnO nanowires are about 1 μm in diameter and grow up to 10 μm in height. EDS shows Ti:O at a ratio less than 1:2, after accounting for the oxygen in ZnO.

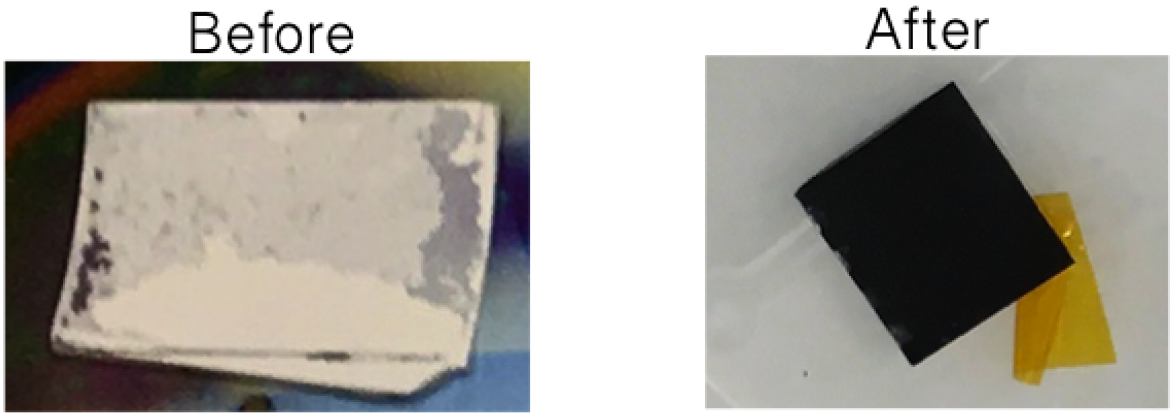

Figure 6.6: Before and after deposition of b-TiOx on ZnO nanowire arrays.

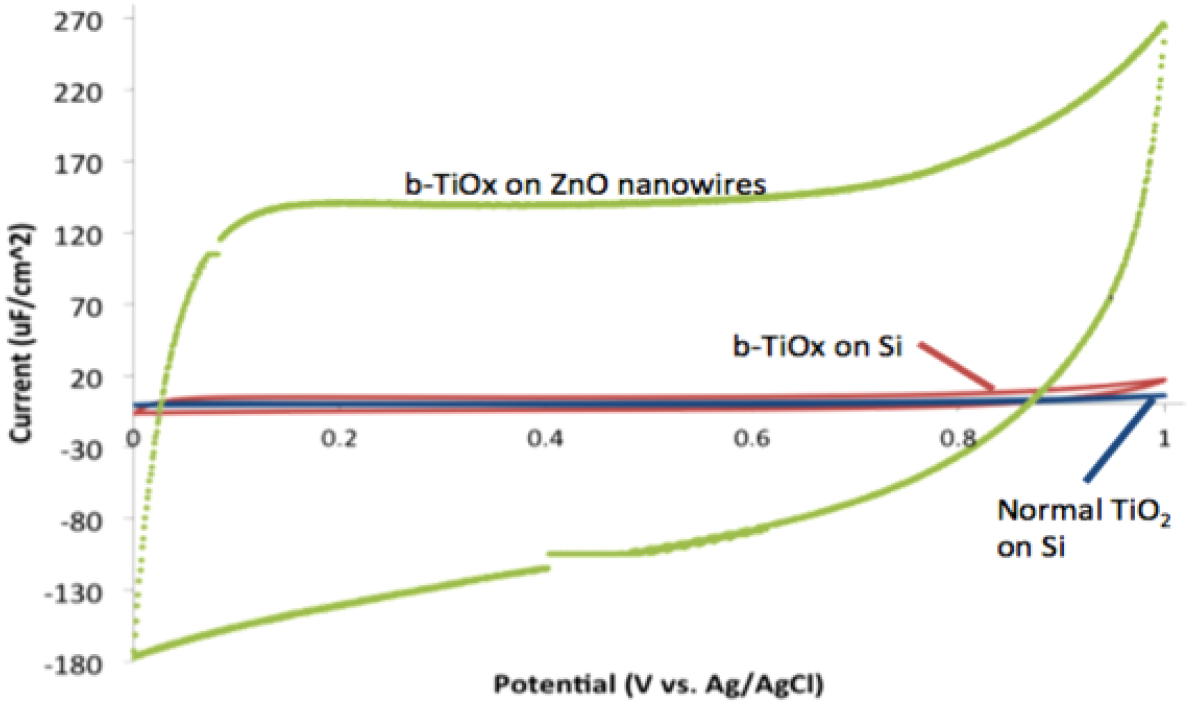

Figure 6.7: Cyclic Voltammograms of supercapacitive performance, corresponding to 2100 μF/cm^2 for b-TiOx on ZnO nanowires (green). For planar substrates, b-TiOx (red) shows >7x improvement in capacitance over that of TiO_2 (blue).

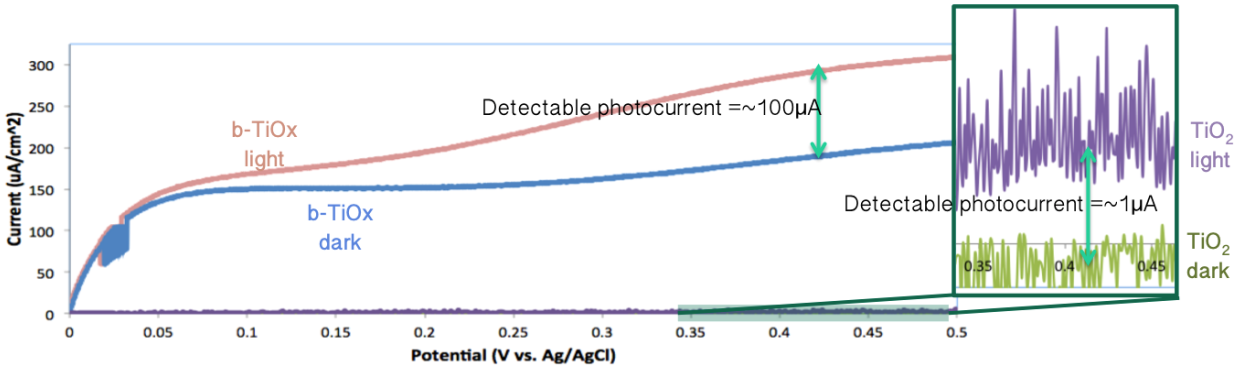

Figure 6.8: Photocurrent measurements under dark and lit (under Xenon lamp) conditions for both b-TiOx and TiO_2 (shown magnified in inset). Photoresponse is quantified by photocurrent: the difference in current between the two conditions. The photocurrent of b-TiOx is 100x that of TiO_2.

Chapter 7

Conclusion

As introduced in the Introductory chapter, the scope of this dissertation was to leverage (1) physical device architecture manipulation, and (2) electrochemical surface reactions to drastically improve energy storage and conversion devices.

The TiN-coated CNTs were able to achieve drastic improvement over bare CNTs for supercapacitor applications. While current technology is limited to a two-step deposition process, or processes with poor conformality such as sputtering, we have achieved a conformal and precise coverage of TiN onto high aspect ratio porous CNT forests for supercapacitor applications. Analysis of our TiN-CNT architecture shows excellent performance and charge capacity, with the ability to increase performance by taking advantage of the flexibility offered by the precise ALD process. Furthermore, the electrode is relatively stable, with the potential for higher stability using different electrolytes or film thicknesses.

Due to the ability of $FePO_4$ to intercalate lithium ions, we are able to demonstrate superior capacitive effects using $FePO_4$-PPY, reaching 3.6 mF/cm^2 (more than 3x the performance of bare PPY films), and 20.8 mF/cm^2 in $FePO_4$-CNTs (more than 20x improvement over bare CNTs). $FePO_4$ cathodes, which have recently come to attention as lithium-ion battery anodes, are limited in performance due to poor conductivity. However, this work presents low temperature, solution-processed synthesis 2D $FePO_4$ sheets, a novel multiple-precursor method for producing 2D materials. These sheets can be loaded onto conductive materials such as PPY and CNTs easily. As such, the development of 2D $FePO_4$ sheets opens up new avenues into highly conductive, high-performance electrochemical electrodes.

In improving energy conversion, we presented first demonstrations of electropolymerized organic semiconducting materials (PT) for PEC water splitting. As such, these devices show drastic improvement in V_{on} over conventional spin-coated P3HT devices due to superior charge separation and texturization using the electropolymerization method. As compared to spin-coated P3HT, with V_{on} = -5.5 V vs. Ag/AgCl, EP-PEC devices achieve V_{on} = 0 V vs. Ag/AgCl. As such, electroplating has the potential to open pathways toward more robust deposition of organic semiconductor PEC materials onto porous conductive substrates.

High aspect-ratio and vertically ordered ZnO/TiO_2 nanoarrays as long as 10μm and less than 50nm in diameter were successfully synthesized for applications in solar-powered hydrogen (H_2) gas harvesters. Hybrid hydrothermal/ALD processing was used to achieve high aspect ratio and high quality nanowire arrays. Surface morphology and phase structure were analyzed to confirm TiO_2-coated ZnO nanowires. Photoelectrochemical responses of synthesized nanowires were measured to investigate their performance as hydrogen gas harvesters. Nanowires with TiO_2 demonstrated improved stability over bare ZnO nanowires during photocatalysis with low bias voltage. Results show that favorable geometry and high quality nanowires not only enhanced chemical stability but also improved required bias voltage to yield photocurrent.

By utilizing ALD, we were able to achieve direct, precise, conformal coatings of b-TiOx over high surface area ZnO nanowire arrays, via limiting oxygen precursor allowed to react on the surface of the substrate. By inducing oxygen vacancies within the TiO_2 matrix, we are able to achieve increased capacitance when used as a supercapacitor material, as well as increased solar absorption over TiO_2. Detectable photocurrent (between lit and dark conditions) on an ALD b-TiOx-based photoelectrochemical device was two orders of magnitude larger than that of a conventional ALD TiO_2 device. Additionally, ALD b-TiOx was able to show the same stabilization properties that conventional ALD TiO_2 show on ZnO nanowires, compared to previous work.

References

A Achour, M Chaker, H Achour, A Arman, M Islam, M Mardani, M Boujtita, L Le Brizoual, MA Djouadi, and T Brousse. Role of nitrogen doping at the surface of titanium nitride thin films towards capacitive charge storage enhancement. *Journal of Power Sources*, 359: 349–354, 2017.

T Bak, J Nowotny, M Rekas, and CC Sorrell. Photo-electrochemical hydrogen generation from water using solar energy. materials-related aspects. *International journal of hydrogen energy*, 27(10):991–1022, 2002.

Michael Ball and Marcel Weeda. The hydrogen economy–vision or reality? *International Journal of Hydrogen Energy*, 40(25):7903–7919, 2015.

Galen Barbose. Renewables portfolio standards in the United States: a status update. *Washington: Lawrence Berkeley National Laboratory*, 2012.

Ray H Baughman, Anvar A Zakhidov, and Walt A De Heer. Carbon nanotubes–the route toward applications. *science*, 297(5582):787–792, 2002.

BMWi. Germany's new energy policy: Heading towards 2050 with secure, affordable, and environmentally sound energy. *Bundesministerium fr Wirtschaft und Energie (Federal Ministry of Economics and Technology*, 2012.

James R Bolton, Stewart J Strickler, and John S Connolly. Limiting and realizable efficiencies of solar photolysis of water. *Nature*, 316(6028):495, 1985.

Bundesnetzagentur. Versorgungsqualitat–SAIDI-Wert 2006-2013. *Available: http://www. bundesnetzagentur. de/DE/Sachgebiete/ ElektrizitaetundGas/ Unternehmen Institutionen/Versorgungssicherheit/ Stromnetze/ Versorgungsqualit*, 2013.

Zhengyang Cai, Bilu Liu, Xiaolong Zou, and Hui-Ming Cheng. Chemical vapor deposition growth and applications of two-dimensional materials and their heterostructures. *Chemical reviews*, 2018.

Liang Chen, Bilu Liu, Mingyuan Ge, Yuqiang Ma, Ahmad N Abbas, and Chongwu Zhou. Step-edge-guided nucleation and growth of aligned wse2 on sapphire via a layer-over-layer growth mode. *ACS nano*, 9(8):8368–8375, 2015.

Xiaobo Chen, Lei Liu, Y Yu Peter, and Samuel S Mao. Increasing solar absorption for photocatalysis with black hydrogenated titanium dioxide nanocrystals. *Science*, 331(6018): 746–750, 2011.

Jonathan N Coleman, Mustafa Lotya, Arlene O?Neill, Shane D Bergin, Paul J King, Umar Khan, Karen Young, Alexandre Gaucher, Sukanta De, Ronan J Smith, et al. Two-dimensional nanosheets produced by liquid exfoliation of layered materials. *Science*, 331 (6017):568–571, 2011.

BE Conway, V Birss, and J Wojtowicz. The role and utilization of pseudocapacitance for energy storage by supercapacitors. *Journal of Power Sources*, 66(1-2):1–14, 1997.

California Public Utilities Commission CPUC. Decision adopting energy storage procurement framework and design program. *Agenda ID# 12370 (Rev. 2)*, 2013a.

California Public Utilities Commission CPUC. CPUC sets energy storage goals for utilities. *Avalable: http://docs.cpuc.ca.gov/PublishedDocs/Published G*, 2013b.

Houlei Cui, Wei Zhao, Chongyin Yang, Hao Yin, Tianquan Lin, Yufeng Shan, Yian Xie, Hui Gu, and Fuqiang Huang. Black tio2 nanotube arrays for high-efficiency photoelectrochemical water-splitting. *Journal of Materials Chemistry A*, 2(23):8612–8616, 2014.

DOE. Hydrogen production: Biomass-derived liquid reforming. *Available: https://www.energy. gov/ eere/fuelcells/ hydrogen-production- biomass- derived-liquid- reforming*.

DOE. Grid energy storage. 2013.

Yaping Du, Zongyou Yin, Jixin Zhu, Xiao Huang, Xue-Jun Wu, Zhiyuan Zeng, Qingyu Yan, and Hua Zhang. A general method for the large-scale synthesis of uniform ultrathin metal sulphide nanocrystals. *Nature communications*, 3:1177, 2012.

Haohong Duan, Ning Yan, Rong Yu, Chun-Ran Chang, Gang Zhou, Han-Shi Hu, Hongpan Rong, Zhiqiang Niu, Junjie Mao, Hiroyuki Asakura, et al. Ultrathin rhodium nanosheets. *Nature communications*, 5:3093, 2014.

EIA. Frequently asked questions: How much U.S. energy consumption and electricity generation comes from renewable sources?. *Available: http://www. eia. gov/tools/faqs/faq. cfm?id=92t=4*, 2015.

US EIA. Monthly energy review. *Energy Information Administration, US*, 2016.

Giuseppe Fiorentino, Sten Vollebregt, FD Tichelaar, Ryoichi Ishihara, and Pasqualina M Sarro. 3d solid-state supercapacitors obtained by ALD coating of high-density carbon nanotubes bundles. In *Micro Electro Mechanical Systems (MEMS), 2014 IEEE 27th International Conference on*, pages 342–345. IEEE, 2014.

Akira Fujishima and Kenichi Honda. Electrochemical photolysis of water at a semiconductor electrode. *nature*, 238(5358):37, 1972.

David C Grahame. The role of the cation in the electrical double layer. *Journal of The Electrochemical Society*, 98(9):343–350, 1951.

Injeti Gurrappa and Leo Binder. Electrodeposition of nanostructured coatings and their characterization–a review. *Science and Technology of Advanced Materials*, 9(4):043001, 2008.

Abhay Gusain, Nirav J Joshi, PV Varde, and DK Aswal. Flexible no gas sensor based on conducting polymer poly [n-9'-heptadecanyl-2, 7-carbazole-alt-5, 5-(4', 7'-di-2-thienyl-2', 1', 3'-benzothiadiazole)](pcdtbt). *Sensors and Actuators B: Chemical*, 239:734–745, 2017.

Marta Haro, Claudia Solis, Gonzalo Molina, Luis Otero, Juan Bisquert, Sixto Gimenez, and Antonio Guerrero. Toward stable solar hydrogen generation using organic photoelectrochemical cells. *The Journal of Physical Chemistry C*, 119(12):6488–6494, 2015.

Takashi Hisatomi, Jun Kubota, and Kazunari Domen. Recent advances in semiconductors for photocatalytic and photoelectrochemical water splitting. *Chemical Society Reviews*, 43(22):7520–7535, 2014.

Xiao Huang, Shaozhou Li, Yizhong Huang, Shixin Wu, Xiaozhu Zhou, Shuzhou Li, Chee Lip Gan, Freddy Boey, Chad A Mirkin, and Hua Zhang. Synthesis of hexagonal close-packed gold nanostructures. *Nature communications*, 2:292, 2011.

C IPC and AR4 Climate Change. Synthesis report, a. *Allali, et al., Editors*, pages 23–73, 2007.

Chaoran Jiang, Savio JA Moniz, Aiqin Wang, Tao Zhang, and Junwang Tang. Photoelectrochemical devices for solar water splitting–materials and challenges. *Chemical Society Reviews*, 46(15):4645–4660, 2017.

Yingqi Jiang, Pengbo Wang, Xining Zang, Yang Yang, Alina Kozinda, and Liwei Lin. Uniformly embedded metal oxide nanoparticles in vertically aligned carbon nanotube forests as pseudocapacitor electrodes for enhanced energy storage. *Nano letters*, 13(8):3524–3530, 2013.

YQ Jiang, Qin Zhou, and Liwei Lin. Planar mems supercapacitor using carbon nanotube forests. In *Micro Electro Mechanical Systems, 2009. MEMS 2009. IEEE 22nd International Conference on*, pages 587–590, 2009.

Dragana Jugović and Dragan Uskoković. A review of recent developments in the synthesis procedures of lithium iron phosphate powders. *Journal of Power Sources*, 190(2):538–544, 2009.

Young-Si Jun, Won Hi Hong, Markus Antonietti, and Arne Thomas. Mesoporous, 2d hexagonal carbon nitride and titanium nitride/carbon composites. *Advanced Materials*, 21(42): 4270–4274, 2009.

Emmeline Kao, Chen Yang, Roseanne Warren, Alina Kozinda, and Liwei Lin. Ald titanium nitride on vertically aligned carbon nanotube forests for electrochemical supercapacitors. *Sensors and Actuators A: Physical*, 240:160–166, 2016.

Oscar Khaselev and John A Turner. A monolithic photovoltaic-photoelectrochemical device for hydrogen production via water splitting. *Science*, 280(5362):425–427, 1998.

Jeffrey T Kiehl and Kevin E Trenberth. Earth's annual global mean energy budget. *Bulletin of the American Meteorological Society*, 78(2):197–208, 1997.

Youngkyoo Kim, Steffan Cook, Sachetan M Tuladhar, Stelios A Choulis, Jenny Nelson, James R Durrant, Donal DC Bradley, Mark Giles, Iain McCulloch, Chang-Sik Ha, et al. A strong regioregularity effect in self-organizing conjugated polymer films and high-efficiency polythiophene: fullerene solar cells. *nature materials*, 5(3):197, 2006.

Peter Krogstrup, Henrik Ingerslev Jørgensen, Martin Heiss, Olivier Demichel, Jeppe V Holm, Martin Aagesen, Jesper Nygard, and Anna Fontcuberta i Morral. Single-nanowire solar cells beyond the shockley–queisser limit. *Nature Photonics*, 7(4):306, 2013.

Kiley Kroh. Germany sets new record, generating 74 percent of power needs from renewable energy. *ThinkProgress RSS*, 13, 2014.

Kristina H LaCommare. Tracking the reliability of the US electric power system: An assessment of publicly available information reported to state public utility commissions. 2008.

Seok Woo Lee, Seung S Lee, and Eui-Hyeok Yang. A study on field emission characteristics of planar graphene layers obtained from a highly oriented pyrolyzed graphite block. *Nanoscale research letters*, 4(10):1218, 2009.

Wi Hyoung Lee, Jeong Ho Cho, and Kilwon Cho. Control of mesoscale and nanoscale ordering of organic semiconductors at the gate dielectric/semiconductor interface for organic transistors. *Journal of Materials Chemistry*, 20(13):2549–2561, 2010.

Wonho Lee, Jung Hwa Seo, and Han Young Woo. Conjugated polyelectrolytes: A new class of semiconducting material for organic electronic devices. *Polymer*, 54(19):5104–5121, 2013.

Fusheng Li, Ke Fan, Bo Xu, Erik Gabrielsson, Quentin Daniel, Lin Li, and Licheng Sun. Organic dye-sensitized tandem photoelectrochemical cell for light driven total water splitting. *Journal of the American Chemical Society*, 137(28):9153–9159, 2015.

Hui Li, Zhenhua Chen, Chun Kwan Tsang, Zhe Li, Xiao Ran, Chris Lee, Biao Nie, Lingxia Zheng, Takfu Hung, Jian Lu, et al. Electrochemical doping of anatase tio 2 in organic electrolytes for high-performance supercapacitors and photocatalysts. *Journal of Materials Chemistry A*, 2(1):229–236, 2014.

Chong Liu, Jinyao Tang, Hao Ming Chen, Bin Liu, and Peidong Yang. A fully integrated nanosystem of semiconductor nanowires for direct solar water splitting. *Nano letters*, 13 (6):2989–2992, 2013a.

Mingzhao Liu, Chang-Yong Nam, Charles T Black, Jovan Kamcev, and Lihua Zhang. Enhancing water splitting activity and chemical stability of zinc oxide nanowire photoanodes with ultrathin titania shells. *The Journal of Physical Chemistry C*, 117(26):13396–13402, 2013b.

Ning Liu, Christopher Schneider, Detlef Freitag, Martin Hartmann, Umamaheswari Venkatesan, Julian Mller, Erdmann Spiecker, and Patrik Schmuki. Black tio2 nanotubes: cocatalyst-free open-circuit hydrogen generation. *Nano letters*, 14(6):3309–3313, 2014.

Haiqiang Lu, Binbin Zhao, Ruili Pan, Jianfeng Yao, Jianhao Qiu, Li Luo, and Yacong Liu. Safe and facile hydrogenation of commercial degussa p25 at room temperature with enhanced photocatalytic activity. *Rsc Advances*, 4(3):1128–1132, 2014.

Xihong Lu, Gongming Wang, Teng Zhai, Minghao Yu, Shilei Xie, Yichuan Ling, Chaolun Liang, Yexiang Tong, and Yat Li. Stabilized tin nanowire arrays for high-performance and flexible supercapacitors. *Nano letters*, 12(10):5376–5381, 2012.

GTABRJA Marland, RJ Andres, TA Boden, et al. Global, regional, and national co2 emissions. *Trends 93: A Compendium of Data on Global Change*, pages 505–584, 1994.

Valentin D Mihailetchi, HX Xie, Bert de Boer, LJ Anton Koster, and Paul WM Blom. Charge transport and photocurrent generation in poly (3-hexylthiophene): methanofullerene bulk-heterojunction solar cells. *Advanced Functional Materials*, 16(5):699–708, 2006.

GK Mor and OK Varguese. Sensor lett. 1, 42 (2003); gk mor, k. shankar, m. paulose, ok varghese, and ca grimes. *Nano Lett*, 5:191, 2005.

Pierre-Olivier Morin, Thomas Bura, and Mario Leclerc. Realizing the full potential of conjugated polymers: innovation in polymer synthesis. *Materials Horizons*, 3(1):11–20, 2016.

Meng Ni, Michael KH Leung, Dennis YC Leung, and K Sumathy. A review and recent developments in photocatalytic water-splitting using tio2 for hydrogen production. *Renewable and Sustainable Energy Reviews*, 11(3):401–425, 2007.

Valeria Nicolosi, Manish Chhowalla, Mercouri G Kanatzidis, Michael S Strano, and Jonathan N Coleman. Liquid exfoliation of layered materials. *Science*, 340(6139):1226419, 2013.

Kostya S Novoselov, Andre K Geim, Sergei V Morozov, D Jiang, Y_ Zhang, Sergey V Dubonos, Irina V Grigorieva, and Alexandr A Firsov. Electric field effect in atomically thin carbon films. *science*, 306(5696):666–669, 2004.

KS Novoselov, A Mishchenko, A Carvalho, and AH Castro Neto. 2d materials and van der waals heterostructures. *Science*, 353(6298):aac9439, 2016.

NREL. State and local governments basics portfolio standards. *Avalable: http://www. nrel. gov/ tech_ deployment/ state_ local_ governments/ basics_ portfolio_ standards. html*, 2014.

Brian O'regan and Michael Grätzel. A low-cost, high-efficiency solar cell based on dye-sensitized colloidal tio2 films. *nature*, 353(6346):737, 1991.

Stephen Pacala and Robert Socolow. Stabilization wedges: solving the climate problem for the next 50 years with current technologies. *science*, 305(5686):968–972, 2004.

Gianfranco Pacchioni. Numerical simulations of defective structures: The nature of oxygen vacancy in non-reducible (mgo, sio2, zro2) and reducible (tio2, nio, wo3) oxides. In *Defects at Oxide Surfaces*, pages 1–28. Springer, 2015.

Rajendra K Pachauri, Myles R Allen, Vicente R Barros, John Broome, Wolfgang Cramer, Renate Christ, John A Church, Leon Clarke, Qin Dahe, Purnamita Dasgupta, et al. *Climate change 2014: synthesis report. Contribution of Working Groups I, II and III to the fifth assessment report of the Intergovernmental Panel on Climate Change*. IPCC, 2014.

Adriana Paracchino, Vincent Laporte, Kevin Sivula, Michael Grätzel, and Elijah Thimsen. Highly active oxide photocathode for photoelectrochemical water reduction. *Nature materials*, 10(6):456, 2011.

Hyun Sung Park, Emmeline Kao, Xining Zang, and Liwei Lin. High aspect ratio-titanium dioxide-stabilized zinc oxide nanowires for photocatalytic hydrogen gas harvester. In *Micro Electro Mechanical Systems (MEMS), 2017 IEEE 30th International Conference on*, pages 667–670. IEEE, 2017.

T Riis, EF Hagen, G Sandrock, PJS Vie, and O Ulleberg. Hydrogen production and storage, international energy agency: Paris, 2006, 2006.

Andrew L Rohl and D Michael P Mingos. Size and shape of molecular ions and their relevance to the packing of the ?soft salts? *Inorganica chimica acta*, 212(1-2):5–13, 1993.

Jean Roncali. Conjugated poly (thiophenes): synthesis, functionalization, and applications. *Chemical Reviews*, 92(4):711–738, 1992.

Abdul K Rumaiz, JC Woicik, E Cockayne, HY Lin, G Hassnain Jaffari, and S Ismat Shah. Oxygen vacancies in n doped anatase tio 2: experiment and first-principles calculations. *Applied Physics Letters*, 95(26):262111, 2009.

Constanze Schliehe, Beatriz H Juarez, Marie Pelletier, Sebastian Jander, Denis Greshnykh, Mona Nagel, Andreas Meyer, Stephan Foerster, Andreas Kornowski, Christian Klinke, et al. Ultrathin pbs sheets by two-dimensional oriented attachment. *Science*, 329(5991): 550–553, 2010.

Dawei Shao, Lingcheng Zheng, Deqiang Feng, Jie He, Rui Zhang, Hui Liu, Xinghua Zhang, Zunming Lu, Weichao Wang, Weihua Wang, et al. Tio 2–p3ht: Pcbm photoelectrochemical tandem cells for solar-driven overall water splitting. *Journal of Materials Chemistry A*, 6 (9):4032–4039, 2018.

Ji-Yong Shin, Jong Hoon Joo, Dominik Samuelis, and Joachim Maier. Oxygen-deficient tio2- δ nanoparticles via hydrogen reduction for high rate capability lithium batteries. *Chemistry of Materials*, 24(3):543–551, 2012.

Supramaniam Srinivasan. Electrode/electrolyte interfaces: Structure and kinetics of charge transfer. In *Fuel Cells*, pages 27–92. Springer, 2006.

Otto Stern. Zur theorie der elektrolytischen doppelschicht. *Berichte der Bunsengesellschaft für physikalische Chemie*, 30(21-22):508–516, 1924.

Ziqi Sun, Ting Liao, Yuhai Dou, Soo Min Hwang, Min-Sik Park, Lei Jiang, Jung Ho Kim, and Shi Xue Dou. Generalized self-assembly of scalable two-dimensional transition metal oxide nanosheets. *Nature communications*, 5:3813, 2014.

Chaoliang Tan and Hua Zhang. Wet-chemical synthesis and applications of non-layer structured two-dimensional nanomaterials. *Nature communications*, 6:7873, 2015.

BV Tilak, C-P Chen, and SK Rangarajan. A model to characterize the impedance of electrochemical capacitors arising from reactions of the type oad+ ne-? rad. *Journal of Electroanalytical Chemistry*, 324(1-2):405–414, 1992.

Roel Van De Krol. Principles of photoelectrochemical cells. In *Photoelectrochemical hydrogen production*, pages 13–67. Springer, 2012.

Hui Wang, Jiajia Zhang, Xudong Hang, Xiaodong Zhang, Junfeng Xie, Bicai Pan, and Yi Xie. Half-metallicity in single-layered manganese dioxide nanosheets by defect engineering. *Angewandte Chemie*, 127(4):1211–1215, 2015.

Roseanne Warren, Firas Sammoura, Kwok Siong Teh, Alina Kozinda, Xining Zang, and Liwei Lin. Electrochemically synthesized and vertically aligned carbon nanotube–polypyrrole nanolayers for high energy storage devices. *Sensors and Actuators A: Physical*, 231:65–73, 2015a.

Roseanne Warren, Firas Sammoura, Fares Tounsi, Mohan Sanghadasa, and Liwei Lin. Highly active ruthenium oxide coating via ald and electrochemical activation in supercapacitor applications. *Journal of Materials Chemistry A*, 3(30):15568–15575, 2015b.

Michael F Weber and MJ Dignam. Splitting water with semiconducting photoelectrodes?efficiency considerations. *International Journal of Hydrogen Energy*, 11(4):225–232, 1986.

Martin Winter and Ralph J Brodd. What are batteries, fuel cells, and supercapacitors?, 2004.

Xu Xiao, Huaibing Song, Shizhe Lin, Ying Zhou, Xiaojun Zhan, Zhimi Hu, Qi Zhang, Jiyu Sun, Bo Yang, Tianqi Li, et al. Scalable salt-templated synthesis of two-dimensional transition metal oxides. *Nature communications*, 7:11296, 2016.

Pengtao Xu, Nicholas S McCool, and Thomas E Mallouk. Water splitting dye-sensitized solar cells. *Nano Today*, 14:42–58, 2017.

Min Yi and Zhigang Shen. A review on mechanical exfoliation for the scalable production of graphene. *Journal of Materials Chemistry A*, 3(22):11700–11715, 2015.

B Yildiz, MC Petri, G Conzelmann, and C Forsberg. Configuration and technology implications of potential nuclear hydrogen system applications. *US Department of Energy*, 2005.

Zhen Zhang and John T Yates Jr. Band bending in semiconductors: chemical and physical consequences at surfaces and interfaces. *Chemical reviews*, 112(10):5520–5551, 2012.

Y Zhao, NC Anderson, K Zhu, JA Aguiar, JA Seabold, J van de Lagemaat, HM Branz, NR Neale, and J Oh. Oxidatively stable nanoporous silicon photocathodes with enhanced onset voltage for photoelectrochemical proton reduction. *Nano letters*, 15(4):2517–2525, 2015.

Zhao Zhao, Huaqiao Tan, Haifeng Zhao, Yang Lv, Li-Jing Zhou, Yujiang Song, and Zaicheng Sun. Reduced tio 2 rutile nanorods with well-defined facets and their visible-light photocatalytic activity. *Chemical Communications*, 50(21):2755–2757, 2014.

Jian Zheng, Han Zhang, Shaohua Dong, Yanpeng Liu, Chang Tai Nai, Hyeon Suk Shin, Hu Young Jeong, Bo Liu, and Kian Ping Loh. High yield exfoliation of two-dimensional chalcogenides using sodium naphthalenide. *Nature communications*, 5:2995, 2014.

Yuzhi Zhou, Daisuke Kiriya, Eugene E Haller, Joel W Ager III, Ali Javey, and Daryl C Chrzan. Compliant substrate epitaxy: Au on mos 2. *Physical Review B*, 93(5):054106, 2016.

Zhigang Zou, Jinhua Ye, Kazuhiro Sayama, and Hironori Arakawa. Direct splitting of water under visible light irradiation with an oxide semiconductor photocatalyst. *nature*, 414 (6864):625, 2001.